# State readout of single Rubidium-87 atoms for a loophole-free test of Bell's inequality

**Norbert Ortegel**


München 2016

# State readout of single Rubidium-87 atoms for a loophole-free test of Bell's inequality

**Norbert Ortegel**

Dissertation
an der Fakultät für Physik
der Ludwig–Maximilians–Universität
München

vorgelegt von
Norbert Ortegel
aus Erlangen

München, den 24.08.2016

Erstgutachter: Prof. Dr. Harald Weinfurter
Zweitgutachter: Prof. Dr. Immanuel Bloch
Tag der mündlichen Prüfung: 18.10.2016

*für meine geistigen Väter, Mütter und Kinder*

# Zusammenfassung

Im Gegensatz zu klassischen Theorien hat die Quantenmechanik - die Theorie zur Beschreibung von Teilchen und Wellen in der mikroskopischen Welt - sehr eigenartige Eigenschaften: Die bekanntesten sind die Heisenbergsche Unschärferelation, die es unmöglich macht bestimmte Paare von Variablen eines Systems gleichzeitig zu bestimmen, sowie die Existenz verschränkter Zustände, die es erlauben zwischen beliebig voneinander entfernten Teilchen nichtlokale Korrelationen zu erzeugen. Dies führte zur Herleitung des Paradoxons von Einstein, Podolsky und Rosen, aus dem die Autoren schlossen, dass die Quantenmechanik keine vollständige Theorie sein kann. Die Möglichkeit der Existenz der daraufhin geforderten vollständigen lokalen versteckten Variablentheorien wurde mit Bells Ungleichung überprüfbar. Dieses Theorem beschränkt die Korrelationen zwischen Messergebnissen an Teilchen aus einem Paar von Zweiniveausystemen. Bis vor kurzem litten Experimente zur Bellschen Ungleichung an Schlupflöchern, die ein beweiskräftiges Ausschließen von lokalen versteckten Variablentheorien verhinderten. Diese sind das Lokalitätsschlupfloch, zur dessen Schließung eine raumartige Trennung der Messungen erforderlich ist, und das Detektionsschlupfloch, nach dem eine gewisse Mindestanzahl aller erzeugten Teilchenpaare ausgelesen werden muss.

Diese Arbeit trägt zu einem Bellexperiment mit einem Paar von einzelnen Rubidium 87 Atomen bei, die 400 Meter voneinander entfernt gefangen sind. Sie konzentriert sich auf die Implementierung einer Atomfalle, die eine schnelle, effiziente und präzise Atomzustandsauslese erlaubt, die es ermöglichen soll beide Schlupflöcher in einem einzigen Experiment zu schließen. Das atomare Zweiniveausystem besteht aus zwei Zeemanzuständen des Atoms im Grundzustand. Die Auslese basiert auf einer zeemanzustandsabhängigen Ionisation der Atome und der darauffolgenden schnellen Detektion der Ionisationsfragmente mit Teilchendetektoren.

Die Atome können in beliebigen Messbasen analysiert werden und der experimentell bestimmte Kontrast zur Unterscheidung zweier orthogonaler Zustände liegt im Bereich von 90%...93%. Dies reicht aus um eine Verletzung der Bellschen Ungleichung mit zwei verschränkten Atomen zu zeigen. Bei jedem Ausleseversuch erhält man eine Antwort über den Atomzustand, womit das Detektionsschlupfloch geschlossen wird. Darüber hinaus liegt die Gesamtdauer der Messung inklusive des Einstellens der Messbasis bei 820 Nanosekunden. Mit einem Abstand zwischen zwei Atomen von 400 Metern wird also auch ein Schließen des Lokalitätsschlupflochs in demselben Experiment möglich.

Rubidiumatome sind ein viel verwendeter Träger von Qubitzuständen im Bereich der Quanteninformation. Im Zusammenhang mit der Quantenkryptographie könnte das vorliegende Ausleseschema den Weg zur Realisierung von geräteunabhängiger Quantenschlüsselverteilung mit einzelnen Atomen eröffnen.

# Abstract

In contrast to classical physical theories, quantum mechanics - the theory describing particles and waves in the microscopic world - has very peculiar properties: The most prominent of them are the Heisenberg uncertainty principle, that makes it impossible to determine certain pairs of variables of a system simultaneously, as well as the existence of entangled states, which allow to establish non-local correlations between two particles at arbitrary distances. This lead to the derivation of the famous paradox of Einstein, Podolsky and Rosen, from which the authors concluded that quantum mechanics cannot be a complete theory. The possibility of the existence of the thereupon postulated complete local hidden variable theories (LHV) became testable with Bell's inequality. This theorem limits the correlations between measurements on particles from a pair of two-level systems. Until recently experiments on Bell's inequality suffered from loopholes that impeded a conclusive exclusion of LHVs. These are the locality loophole that requires spacelike separation of the measurements and the detection loophole that requires that a minimum number of all created particle pairs is read out.

This work contributes to a Bell-experiment with a pair of single Rubidium 87 atoms that are trapped at a distance of 400 meters. It focuses on the implementation of an atom trap setup that enables a fast, efficient and precise readout of the atomic state which shall allow to close both loopholes simultaneously in one experiment. The atomic two-level system consists of two Zeeman states of the ground state atoms. The readout is based on a Zeeman state selective ionization of the atoms and subsequent fast detection of the ionization fragments with charged particle detectors.

The atoms can be analyzed in arbitrary measurement bases and the experimentally determined contrast to distinct between two orthogonal Zeeman states is in the range of 90%...93%. This is sufficient for demonstrating a violation of Bell's inequality with two entangled atoms. For every readout attempt an answer about the atomic state is obtained which allows to close the detection loophole. Furthermore, including the setting of the measurement basis the overall duration of the readout is 820 nanoseconds. Given the inter-atomic distance of 400 meters, it hence becomes also possible to close the locality loophole in the same experiment.

Rubidium atoms are a commonly used carrier of qubit states in quantum information science. In the realm of quantum cryptography the presented readout scheme could for example open the path to realizing device-independent quantum key distribution with single atoms.

# Contents

# 1. Introduction

Despite of the overwhelming achievements of quantum mechanics in the beginning of the twentieth century in explaining by then puzzling phenomena like the blackbody radiation and the discrete emission spectra of atoms, great skepticism remained among physicists about this new theory. This was for example due to the impossibility to measure certain observables simultaneously - resulting in the well-known Heisenberg uncertainty relation. Quantum mechanics also does not make a definite statement about the actual state of a system until it is measured. It rather assumes that the system is fully described by a coherent superposition of different states until it instantaneously collapses to one of the eigenstates of the measured observable during the measurement process. This lead some physicists to believe that quantum mechanics did not deliver a complete description of nature.

Einstein, Podolsky and Rosen provided strong support of this conjecture with their derivation of the famous EPR-paradox in 1935 [1]. They considered measurements of non-commuting quantities on two particles sharing a common quantum state. Implicitly assuming the concept of *locality*, i.e. that for an appropriate separation of the particles the measurement on one particle cannot causally influence the other particle, and by postulating *realism*, i.e that each physical quantity must have a definite value already before it is measured, they derived that quantum mechanics cannot be considered complete if quantities of non-commuting observables cannot be determined simultaneously. As a solution they postulated theories with additional *hidden variables* that would resolve this problem and give a complete picture of nature. Bohm reformulated the paradox in terms of measurements on two spin-$\frac{1}{2}$ particles that are prepared in a non-separable entangled state [2, 3]. The spin orientations of those particles would show strict correlations even if the measurements on the single particles were causally independent from each other. Bohm reinterpreted the paradox by stating that these correlations would require some hidden - probably even *non-local* or instantaneous - interaction between the distant particles, thus being in contradiction with special relativity.

Finally, John Bell opened up a possibility to rule out at least such theories that assume local hidden variables (LHV) in an experiment of the kind that Bohm had proposed. He found an inequality limiting the outcomes of measurements on a bipartite two-level system, that would always hold for any description of the system with local hidden variable theories (Bell's theorem), but that could be violated according to the predictions of quantum mechanics [4]. Clauser, Horne, Shimony and Holt then generalized this inequality as to make it applicable to realizable experiments [5]. In the following decades several experiments demonstrated a violation of the CHSH inequality [6, 7, 8].

However, these experiments suffered from so-called loopholes that still allowed for an explanation of the results with local hidden variable theories. The two major loopholes are the *locality loophole* and the *detection loophole.* To close the locality loophole the measurement on one

particle - including the choice of the measured observable, i.e. the measurement basis - must be space-like separated from the measurement on the other particle and vice versa. This is in order to exclude any influence of the basis choice and measurement outcome at particle 1 on the outcome at particle 2 via an interaction at or below the speed of light. The second major loophole, the detection loophole, arises when only a small subset of all produced particle pairs is read out such that the results from the detected pairs cannot be assumed to be representative for the whole ensemble. Hence, in an ideal experiment all of the created particles should be observed.

The third loophole is the so-called *freedom-of-choice loophole*. It states that full independence of the two observers from each other as well as from possible local hidden variables is required. In other words it must be assured that the choice of the measurement bases can be considered as free or random. While the interactions considered in the locality and freedom-of-choice loophole already have to be intrinsically excluded for the derivation of Bell's theorem, the detection loophole was independently brought up by Pearle [9].

Since the first tests of Bell's inequality further experiments have been performed that closed the above mentioned loopholes. The locality loophole was first partially addressed [10] and finally strictly closed [11] in experiments with photons. Later the locality and freedom-of-will loophole were simultaneously closed within one experiment [12]. These demonstrations were possible due to the technical simplicity of separating photons over large distances thus guaranteeing the space-like separation of the readouts. The detection loophole was first closed in experiments with ions and solid state particles [13, 14] that allow for a higher detection efficiency. With the development of highly efficient superconducting transition edge single photon detectors [15] this eventually also became possible for experiments with photons [16]. However, only lately experiments with entangled nitrogen vacancy centers [17, 18] and yet again with photons [16, 19] were able to close the two major loopholes, the locality and the detection loophole, simultaneously.

It should be pointed out that a violation of Bell's inequality is not a definite proof of the validity of quantum mechanics. In fact other hidden variable theories such as Bohmian mechanics [20, 21] can predict the same experimental results as quantum mechanics. Bohmian mechanics is, however, of non-local nature and hence not subject of Bell's theorem. Also so-called superrealistic and deterministic LHVs (see e.g. [12] for a descriptive classification of LHVs) cannot be excluded by Bell's theorem as their basic assumptions do not allow to close the locality and freedom-of-will loophole.

Apart from this fundamental interest in Bell's inequality it has also found practical relevance in the context of quantum cryptography and quantum key distribution (QKD). In a first proposal of "Quantum Cryptography Based on Bell's Theorem" [22] it was shown that an entangled EPR pair can be used to perform QKD while Bell's theorem allows to detect potential eavesdroppers. Such a system has lately been shown to be secure even when the devices used by the key exchanging parties are untrusted [23]. The so-called "device-independent quantum key distribution", however, again relies on the readouts of the particles at the respective remote receivers to be space-like separated and the detection loophole being closed.

This work contributed to a successful realization of a loophole-free Bell experiment. The experiment is based on a pair of entangled Rubidium 87 atoms that are trapped at a distance of 400 meters in different laboratories and buildings of the university. Due to the impossibility

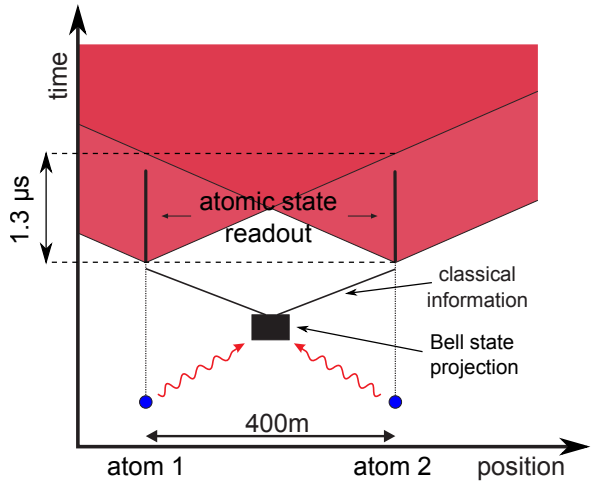


Figure 1.1.: Simplified space-time diagram of the Bell-experiment: Two single atoms trapped at a distance of 400 m are entangled via "entanglement swapping". After the creation of entanglement the atomic state readout is initialized. For space-like separation the full duration of the readout at one atom must be outside the light cone of the measurement on the other atom.

of creating the entanglement in a direct interaction of the two atoms we make use of the so-called entanglement swapping protocol [24] that allows to create entanglement between basically arbitrarily remote particles. Figure 1.1 shows a space-time diagram of the experiment. The spin of each of the atoms is first entangled with the polarization state of a single photon originating from a spontaneous emission process of the atom. These two photons are then brought together via an optical fiber link. Their common polarization state is now projected onto a maximally entangled Bell-state using Hong-Ou-Mandel interference of the photons at a beam splitter [25] and subsequent detection of the photons at the output ports. The detection heralds the successful projection of the photons' polarizations and swaps the entanglement onto the atoms' common spin state. The information about the creation of entanglement is then transmitted to the trap sites where the atomic state readout is performed.

The creation of atom-atom entanglement with this scheme as well as a violation of Bell's inequality had already been demonstrated in [26] for an inter-atomic distance of 20 m. The atomic readout efficiency of unity allowed to close the detection looophole. However, the locality loophole was not closed due to the long duration of the readout via fluorescence detection which had a duration of about 40 ms. Thanks to the ability to distribute atom-photon entanglement over long distances [27] the interatomic distance could now be increased to 400 m. This now leaves 1.3 µs for the atomic state readouts in order to be space-like separated.

### Aim of this thesis

This thesis focuses on the implementation of a sufficiently fast and efficient atomic state readout for the envisioned Bell experiment. In such an experiment each of the observers of the two atoms

must be able to measure the atom's spin orientation along two different directions (measurement bases). In our case the Hilbert space of this spin state is spanned by two Zeeman states of the atom's electronic ground state. The readout must hence be able to perform projection measurements onto these Zeeman states or quantum mechanical superpositions of them. Basically the readout consists of two steps: First, a state-selective laser-induced ionization of the atoms that ionizes atoms in a predefined superposition of the two Zeeman states while leaving atoms in the orthogonal state unaffected. And second, a subsequent detection of the potential ionization fragments with charged particle detectors. Those basic components having already been studied in previous works [28, 29], the objective of the present thesis was to integrate them into the trap setups and characterize the system with respect to its suitability for a loophole-free test of Bell's theorem.

In the beginning this work gives an introduction into the trapping of single Rubidium atoms and introduces the employed atom-photon entanglement scheme as well as the envisaged readout scheme. The following chapters present the experimental setup of the single atom trap. It had to be constructed from scratch in order to be able to integrate the new atomic state readout. A focus lies on all aspects that are associated with the fidelity and speed of the readout. The final chapter experimentally characterizes the performance of the readout scheme in terms of the contrast with which it can distinguish between two orthogonal Zeeman states as well as the overall duration of the atomic state readout.

# 2. Methods

This chapter first describes the basic physical properties of Rubidium 87 that are relevant for this experiment and continues with a short introduction to the techniques for trapping single neutral atoms with so-called optical dipole traps.

After this we explain the preparation of entanglement between the Zeeman-state of a single Rubidium 87 atom and the polarization state of a single photon emitted by the atom in a spontaneous decay process. This is the same process that is also utilized during the entanglement swapping for the loophole-free Bell experiment with two remotely trapped atoms. In the context of this thesis atom-photon entanglement will be employed as a means to prepare well-defined atomic spin states in order to be able to characterize the fidelity of the envisaged atomic state readout.

The chapter ends with the introduction of the Zeeman-state selective readout that is based on state-selective ionization of the atom and subsequent detection of the ionization fragments. We will briefly compare this method to other possible state readouts, emphasize its specific advantages and present results from a numerical simulation of the ionization process that provide information about the theoretically possible fidelity.

Throughout the chapter we will highlight specific sources of experimental errors - of both physical and technical nature - that can arise during the state preparation and readout.

## 2.1. Properties of Rubidium 87

Due to their well-studied and relatively simple hydrogen-like level structure with only one valence electron alkali atoms have become the workhorse of many quantum optics experiments with neutral atoms. Rubidium is an alkali atom with the atomic number 37 and the electronic ground state configuration $[Kr]5s^1$. The ionization energy of an atom in this ground state is 4.177127 eV [30].

In this experiment we use the isotope $^{87}$Rb which has a mass of $m_{Rb87} = 1.443 \cdot 10^{-25}\,\mathrm{kg}$ and a nuclear spin of $\frac{3}{2}$. In its ground state the valence electron resides in the $5^2S_{1/2}$ orbital (figure 2.1) which is split up into the hyperfine-levels $F = 1$ and $F = 2$ with a level-spacing of 6.83 GHz [30]. Excitation to the two higher lying finestructure levels $5^2P_{1/2}$ and $5^2P_{3/2}$ can be achieved via dipole transitions at the near infrared wavelengths of 794.98 nm and 780.24 nm, respectively. In order to ionize atoms in the state $5^2P_{1/2}$ during the envisaged ionization-based state readout, photons with a wavelength below 473.67 nm are required. The excited states split up into hyperfine levels $F = 1, 2$ and $F = 0, 1, 2, 3$ - this time with smaller spacings of 814.5 MHz and 72.2, 156.9, and 266.7 MHz, respectively. Each of the hyperfine states in turn consists of $2F + 1$

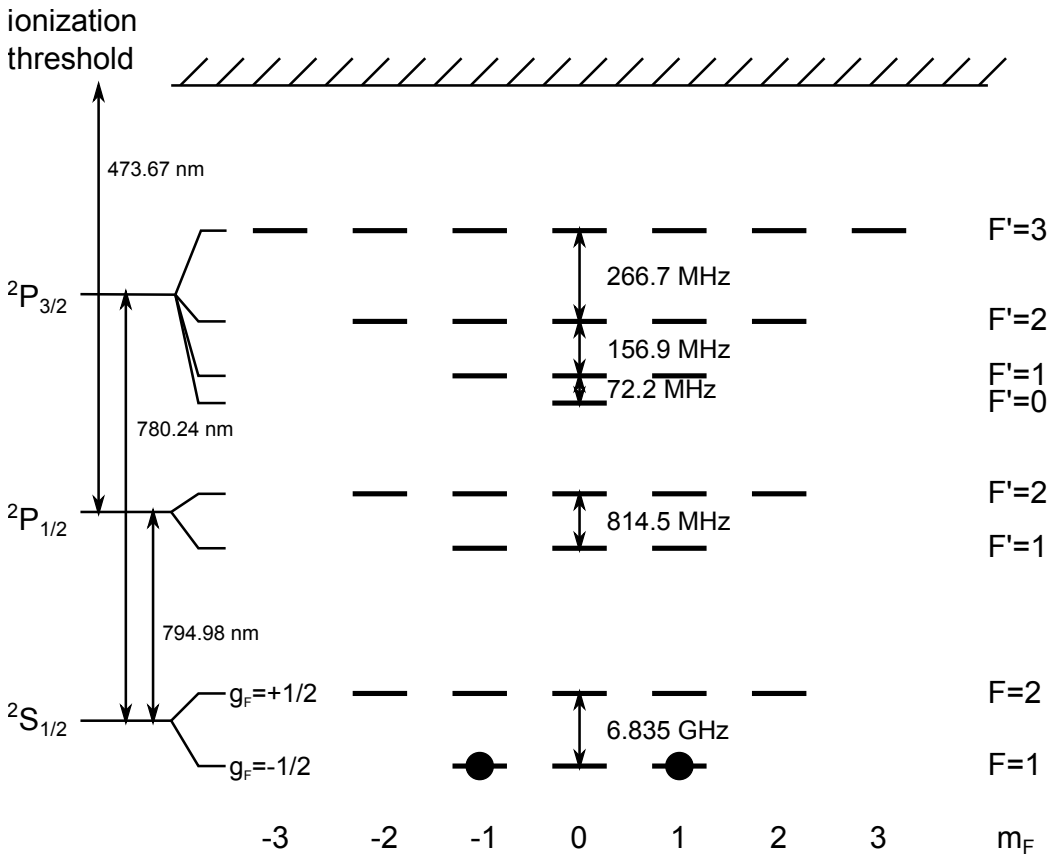


Figure 2.1.: Atomic level scheme of Rubidium 87 showing the ground state $5^2S_{1/2}$ and the first two excited states $5^2P_{1/2}$ and $5^2P_{3/2}$. The two states marked with black spheres are used to form the atomic qubit.

Zeeman sublevels $m_F$ that are degenerate in the absence of external magnetic and ellipitcally polarized optical fields.

In this experiment the atomic qubit will be represented by the Zeeman states $m_F = \pm 1$ of the $5^2S_{1/2}, F = 1$ hyperfine level. The sensitivity of the qubit states to magnetic fields is determined by the Landé factor $g_F$ of the hyperfine level $F = 1$. Its value is $-\frac{1}{2}$, leading to an energy shift of the $m_F = \pm 1$ states of $\mp 0.7$ MHz/Gauss[30].

From a technical point of view Rubidium has the advantage of being commercially available in the form of metallic vapor dispensers. Moreover, the light fields for driving transitions between the ground and first excited states can be produced with easy to handle diode lasers that are as well commercially available at low cost. A further advantage in the context of this experiment is that the wavelength of photons emitted via transitions from $5P$ to the ground state shows a relatively low absorption of $<$3.5 dB/km in single-mode optical fibers. For our fiber link with a length of 720 meters this means losses of less than 50% which allows to efficiently distribute atom-photon entanglement through the fiber link and thus establish atom-atom entanglement at decent event rates.

## 2.2. Trapping of single $^{87}$Rb-atoms

This experiment requires a mechanism that is able to trap a single neutral atom at a well defined position while allowing good optical access to the atom from all directions. A strong localization of the atom is neccessary in order to be able to efficiently collect its emitted fluorescence. Furthermore the trapping mechanism must not lift the degeneracy of Zeeman-sublevels within one hyperfine state in order to not disturb the atomic qubit. All of these requirements can be fulfilled with a strongly focused optical dipole trap (ODT) as it will be presented in this section.

In order to avoid collisions with atoms from the background gas such experiments must be performed in ultrahigh vacuum (UHV), i.e. at pressures of about $10^{-10}$mbar. The trap is loaded with Rubidium atoms that are evaporated from a metal vapor dispenser which is heated to 600 K. Due to the shallow trapping potential of ODTs, which is on the order of millikelvin, an intermediate cooling stage is indispensable. This is realized by Doppler cooling in a magneto-optical trap (MOT). It creates a cloud of cold atoms at a temperature close to or even below the Doppler limit which is at 146 µK for $^{87}$Rb [30]. The MOT is overlapped with the position of the ODT so that the latter can pick a single atom out of the precooled atomic cloud.

This section introduces the magneto-optical trap and the optical dipole trap. Their basic working principle is explained as well as the overall procedure to load the single atom trap. A detailed description of the experimental setup including the vacuum chamber and the confocal microscope for the optical dipole trap can be found in chapter 3.

### 2.2.1. Magneto-optical trap

The first step towards trapping single neutral Rubidium atoms is to prepare a cold cloud of atoms at temperatures that are well below the depth of the optical dipole trap. This is achieved by using

a magneto-optical trap (MOT) [31, 32], the working principle of which is based on the effect of Doppler cooling [33].

A MOT consists of three pairs of counterpropagating laser beams along the three spatial axes that intersect at a common crossing point. The frequency of the laser light is red-detuned to the transition $5^2S_{1/2}, F = 2 \rightarrow 5^2P_{3/2}, F' = 3$ which leads to the desired Doppler-cooling once an atom moves opposite to the propagation direction of any of the laser beams. Thus the lasers form a molasse-like dissipative force field that cools the atoms coming from the dispenser in all spatial degrees of freedom. To make the radiation pressure from the cooling beams position-dependent and thus form a trap for the atoms a magnetic quadropole field is applied using a pair of magnetic field coils in anti-Helmholtz configuration. The center of the quadrupole field is overlapped with the crossing section of the laser beams. This shifts the energies of the Zeeman-sublevels in such a way that - together with appropriate circular polarization of the cooling beams - atoms moving away from the trap center experience stronger radiation pressure from that beam that drives them back to the center. In this configuration with counterpropagating circularly polarized laser beams additional polarization gradient cooling occurs [34] that even allows for cooling well below the Doppler limit.

The used cooling transition is closed in the sense that after excitation to $5P_{3/2}, F' = 3$ the only decay channel to the ground state via a dipole transition leads back to $5^2S_{1/2}, F = 2$. Atoms that leave this cooling cycle via additional decay channels - possibly also after off-resonant excitation to neighboring hyperfine-levels - are recycled by excitation with a repump laser resonant to $5^2S_{1/2}, F = 1 \rightarrow 5^2P_{3/2}, F' = 2$.

### 2.2.2. Optical dipole trap

The trapping potential of an optical dipole trap is produced by a strongly focused laser beam with a wavelength that is far detuned from the dipole transition between the ground state and the first excited state. The interaction with the detuned beam induces an ac-Stark shift of the eigenenergies of the ground state hyperfine-levels which is proportional to the beam intensity. In the case of alkali atoms a red detuning (i.e. the laser's wavelength is larger than that of the atomic transitions) leads to a lowering of these energies. It is thus energetically beneficial for a ground state atom to seek the spot with highest laser intensity. For a gaussian beam this will be the center of the beam focus (see figure 2.2).

The resulting potential energy $U(r, z)$ for an atom in hyperfine state $F$ and a beam of intensity $I(r, z)$ is given by [35]:

$$U(r,z) = \frac{\pi c^2 \Gamma}{2\omega_0^3} \left( \frac{2 + g_F m_F P}{\Delta_{2,F}} + \frac{1 - g_F m_F P}{\Delta_{1,F}} \right) \cdot I(r,z) \tag{2.1}$$

Here $\Gamma$ and $\omega_0$ are the decay rate and the central transition frequency of the D-line. $g_F$ is the Landé factor of the considered hyperfine state and $\Delta_{1,F}$, $\Delta_{2,F}$ are the detunings of the light field with respect to the central transition frequencies between the hyperfine ground state $F$ and $^2P_{1/2}$, $^2P_{3/2}$, respectively (red detuning: $\Delta < 0$, blue detuning: $\Delta > 0$). $m_F$ is the magnetic quantum number of the atomic Zeeman state in a reference system with the quantization axis along the

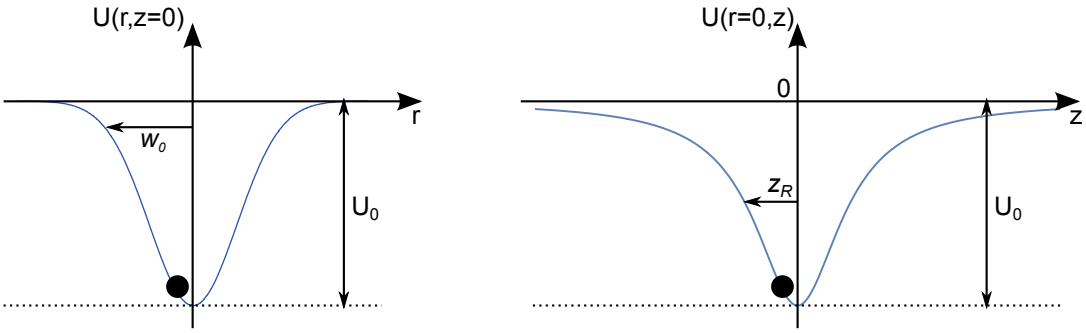


Figure 2.2.: Light shift $U(r, z)$ of the atomic ground state energy in an optical dipole trap with Gaussian beam shape. Left: Cut through the focal plane ($z = 0$). Right: On the beam axis ($r = 0$). The trapping potential has its minimum $U_0$ at the spot of highest laser intensity.

beam axis of the trap laser. Finally, $P$ denotes the polarization of the light field. It is related to the ellipticity $\epsilon$ via $P = \sqrt{1-\epsilon^2}$, with the normalized polarization vector (Jones vector) of the laser beams being $\hat{\varepsilon} = 1/\sqrt{2}(\sqrt{1+\epsilon}\,\hat{x} + i\sqrt{1-\epsilon}\,\hat{y})$ [36].

One can easily see that for linearly polarized light ($\epsilon = 1$, $P = 0$) the dependence on the magnetic quantum number $m_F$ vanishes, i.e. the Zeeman-sublevels remain degenerate and the atomic qubit is thus not disturbed by the trap. However, with circular polarization components ($\epsilon < 1$ and hence $P \neq 0$) the degeneracy is lifted. The light field then induces an undesired temporal evolution of the atomic Zeeman states in the same manner as it would occur for a magnetic field applied along the beam axis[1]. Thus a high purity of linear polarization for the trap laser is necessary. Unwanted scattering of photons from the trapping laser which would as well disturb the atomic state is strongly suppressed due to the large detuning.

It has been demonstrated that for properly chosen trap depth and size loading of more than one atom into the trap is inhibited via light-induced collisions that happen due to continuous illumination with the cooling light from the MOT [37, 38].

Note that this trapping mechanism relies on shifting the energy levels of the bound valence electron. An atom that is ionized during the atomic state readout is hence no more trapped and its ionization fragments can be detected with the charged particle detectors as desired.

### Trap parameters and localization of the atom

Our trap laser is linearly polarized, has a wavelength of 852 nm and its beam has a gaussian profile. Using a microscope objective (see section 3.1.2) the laser is focused to a waist of $w_0$=1.92 µm resulting in a Rayleigh range of $z_R$=13.6µm. For a laser power of 15.0 mW at the position of the trap we obtain a peak intensity in the focal spot of $I_0(0,0) = 2.59 \cdot 10^9$ W/cm². With values for $\Gamma, \omega_0$ and $\Delta_{i,F}$ from [30] we can use equation 2.1 to calculate the maximum trap depth. We obtain:

[1]Note that $P$ is only positive for this special case of $\hat{\epsilon}$ (right circular polarization components). For $\hat{\varepsilon} = 1/\sqrt{2}(\sqrt{1+\epsilon}\,\hat{x} - i\sqrt{1-\epsilon}\,\hat{y})$ (left circular polarization components) $P$ is negative: $P = -\sqrt{1-\epsilon^2}$

$$U_0 = k_B \cdot 1.13\,\mathrm{mK} \tag{2.2}$$

This can be compared with the temperature of the trapped atoms in order to estimate how strongly the atoms are localized in the ODT. Measurements of the temperature have been performed [39] that yield a value of $T$ =57 µK which is more than a factor of 20 below the maximum trap depth. It can thus be expected that the atom is bounded to distances from the trap center that are well below $w_0$ and $z_R$. At these low energies the trapping potential can also be approximated as that of a three-dimensional harmonic oscillator. In this case the probability distribution of the spatial position of the atom is of gaussian shape with the following standard deviations in radial and longitudinal direction [40]:

$$\sigma_r = \sqrt{\frac{k_B T}{2U_0}} w_0 = 305\,\mathrm{nm} \tag{2.3}$$

$$\sigma_z = \sqrt{\frac{k_B T}{2U_0}} z_R = 2.16\,\mu\mathrm{m} \tag{2.4}$$

The ionization fragments that are going to be produced during the atomic state readout envisaged in this thesis hence originate from an almost pointlike source. Due to the low temperature of the atoms their typical starting velocity directly after the ionization will be on the order of only

$$\hat{v} = \sqrt{\frac{2 \cdot k_B T}{m_{\mathrm{Rb87}}}} = 10.4\,\frac{\mathrm{cm}}{\mathrm{s}}, \tag{2.5}$$

with $\hat{v}$ being the maximum of the Maxwell-Boltzmann velocity distribution with temperature $T$.

### 2.2.3. Trap operation

Once a pre-cooled atom from the MOT enters the conservative potential of the ODT, it dissipates the gained potential energy by continuing to scatter photons from the cooling beams and can hence no more leave the trapping potential. In order to monitor the presence of an atom in the optical dipole trap, we collect fluorescence induced by the cooling beams within the ODT's volume by using the same microscope objective that is used to focus the dipole trap laser (confocal arrangement). Trapping and loss of an atom are then clearly visible from a rise and fall of the countrate of fluorescence photons (see figure 2.3). Immediately after an atom has been trapped, the magnetic field of the MOT is switched off and the surrounding cloud of cold atoms expands quickly, thus not disturbing the further experiment.

The loading rate of the magneto-optical trap depends directly on the density of Rubidium atoms in the vacuum chamber. To increase this density temporarily during the loading period we make use of light-induced atom desorption [41] of atoms on the inner walls of the vacuum chamber by illuminating them with a UV-LED. This allows to reduce the required evaporation from the dispensers and thus increase their lifetime.

Including the time for loading the magneto-optical trap it takes about 0.5 seconds to load a single atom into the ODT. The $1/e$-lifetime of the atoms in the trap is on the order of several

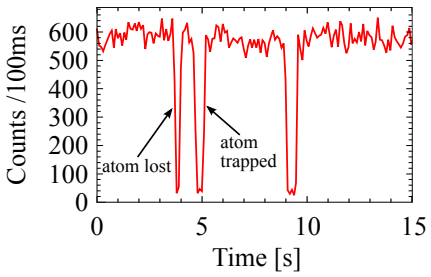


Figure 2.3.: Fluorescence from the optical dipole trap collected with the confocal microscope over a period of 15 seconds. Loading and loss of a single atom lead to a sudden rise and fall of the fluorescence.

seconds. However, both the loading rate as well as the lifetime of the trapped atoms strongly depend on the optical allignment of the MOT's cooling beams and can hence show strong temporal drifts over the course of several days to weeks.

## 2.3. Atomic state preparation via atom-photon entanglement

In order to be able to test the envisioned atomic state readout a reliable and precise method to prepare a well-defined state of the atom is required. In detail one has to be able to prepare different superpositions of the $m_F = \pm 1$-Zeeman states in the $F = 1$ ground state.

This work follows the idea to first entangle the Zeeman state of the atom with the polarization state of a single photon. This shall happen via the emission of this photon during a spontaneous decay of the previously excited atom. A projection measurement on the photon in an arbitrary basis then projects the atom onto one of the eigenstates of the corresponding atomic measurement basis. Due to the simplicity of setting the measurement basis in a polarization readout of photons it is thus easy to prepare various superposition states on the atom with a high fidelity.

This section describes the three main steps of the atomic state preparation:

1. Optical pumping into the initial ground state $F = 1, m_F = 0$ .

2. Optical excitation to $F' = 0, m_F = 0$ in $5^2P_{3/2}$. The subsequent decay generates a single photon whose polarization state is entangled with the resulting spin state of the atom.

3. Collection of the emitted photon and projection measurement on its polarization degree of freedom.

In the end we will discuss possible sources of error during this process that reduce the fidelity of the state preparation.

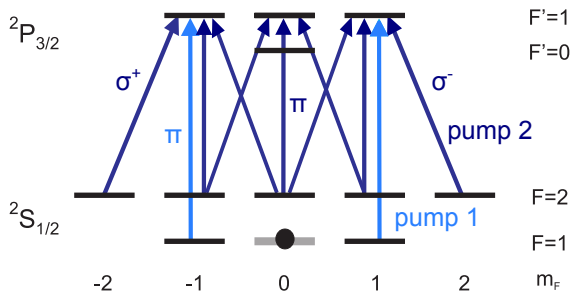


Figure 2.4.: Level scheme explaining the optical pumping to prepare the initial ground state $F = 1, m_F = 0$. Alternated $\pi$- and $\sigma$-polarized pulses from laser "pump 2" transfer population from $F = 2$ to $F = 1$. Here a second laser ("pump 1") transfers the population from the Zeeman-states $m_F = \pm 1$ to $m_F = 0$.

### 2.3.1. Initial state preparation by optical pumping

The preparation of the initial state $F = 1, m_F = 0$ is achieved by means of optical pumping and is depicted in figure 2.4.

The laser "pump 2" which is resonant to the transition $S_{1/2}, F = 2 \rightarrow P_{3/2}, F' = 1$ empties the hyperfine level $F = 2$. It alternately irradiates the atom along different beam axes in order to achieve an effective switching of the polarization between $\pi$- and $\sigma$. This is necessary in order to exclude the existence of any coherent dark state in $F = 2$ since population in this dark state would not be transferred to $F = 1$. Simultaneously the $\pi$-polarized laser "pump 1" resonant to $S_{1/2}, F = 1 \rightarrow P_{3/2}, F' = 1$ is applied in order to empty the outer Zeeman-states $m_F = \pm 1$ in $F = 1$. The atom continuously scatters light from the two lasers until it decays into $F = 1, m_F = 0$. This state is dark with respect to "pump 1" since the transition $F = 1, m_F = 0 \rightarrow F' = 1, m_F = 0$ is dipole-forbidden.

These pump lasers are applied before each excitation attempt for a duration of 2 µs.

### 2.3.2. Generation of atom-photon entanglement

After preparation of the initial ground state the atom is excited to $5^2P_{3/2}, F' = 0, m_F = 0$ with a $\pi$-polarized laser pulse (figure 2.5 *left*). From here the atom decays back into the $F = 1$ hyperfine ground state via three possible decay channels (figure 2.5 *right*). Due to conservation of angular momentum the spin of the emitted photon is directly related to the resulting spin-state of the atom. When emitting a $\sigma^{\pm}$-polarized photon (spin parallel/anti-parallel to the quantization axis) the atom decays into Zeeman states $|1, \mp 1\rangle$ (spin anti-parallel/parallel to the quantization axis), whereas the emission of a $\pi$-polarized photon (spin orthogonal to quantization axis) leads to the atomic state $|1, 0\rangle$. Since the decay channels have equal probability and are indistinguishable in all other degrees of freedom, the following entangled atom-photon state is obtained:

$$|\Psi\rangle = \frac{1}{\sqrt{3}} \left( |\sigma^+\rangle|1, -1\rangle + |\pi\rangle|1, 0\rangle + |\sigma^-\rangle|1, +1\rangle \right) \tag{2.6}$$

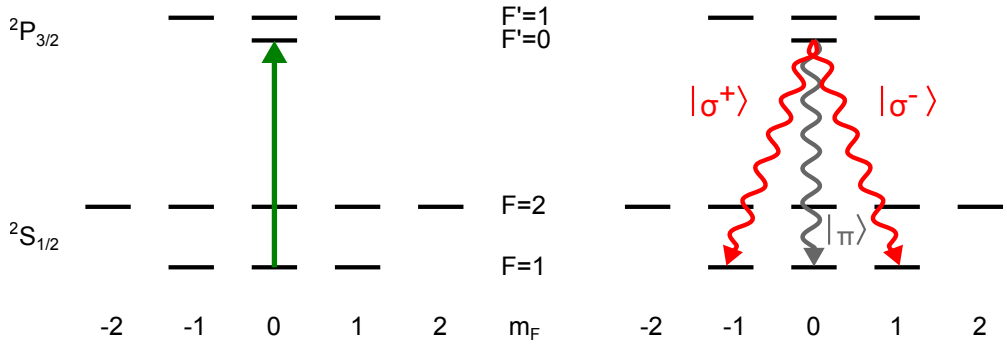


Figure 2.5.: Generation of atom-photon entanglement. *Left*: Optical excitation *Right*: Spontaneous decay producing the entangled atom-photon pair.

However, with our collection optics we only detect photons that are emitted into a mode that is symmetric around the quantization axis. These are only the $\sigma^{\pm}$-polarized photons. The decay which produces $\pi$-polarized photons does not yield any detectable atom-photon entanglement events [42]. Hence the effective Hilbert space of all observable atom-photon pairs is reduced and is spanned by the pairs of basis states $|\sigma^{\pm}\rangle$ and $|1, \mp 1\rangle$, respectively. The actual entangled state then is:

$$|\Psi\rangle_{AP} = \frac{1}{\sqrt{2}} \left( |\sigma^{+}\rangle |1,-1\rangle + |\sigma^{-}\rangle |1,+1\rangle \right) \tag{2.7}$$

This is one of the four maximally entangled Bell-states. By rewriting it in the complementary basis pairs of linear polarization $H/V$ and $\pm 45°$ one obtains:

$$|\Psi\rangle_{AP} = \frac{1}{\sqrt{2}} \left( |H\rangle \frac{1}{\sqrt{2}} \left( |1,+1\rangle + |1,-1\rangle \right) + i|V\rangle \frac{1}{\sqrt{2}} \left( |1,+1\rangle - |1,-1\rangle \right) \right) \tag{2.8}$$

and

$$|\Psi\rangle_{AP} = \frac{1}{\sqrt{2}} e^{-i\frac{\pi}{4}} \left( |+45°\rangle \frac{i}{\sqrt{2}} \left( |1,+1\rangle - i|1,-1\rangle \right) - |-45°\rangle \frac{1}{\sqrt{2}} \left( |1,+1\rangle + i|1,-1\rangle \right) \right) \tag{2.9}$$

These representations reflect the typical property of entangled states to be non-separable in any basis.

### 2.3.3. State projection of the photon

The photon that is emitted during the atom-photon entanglement is collected with a microscope objective and coupled into a single mode fiber. Both, the optical axis of the objective as well as the central axis of the single guided mode of the fiber conicide with the quantization axis. In

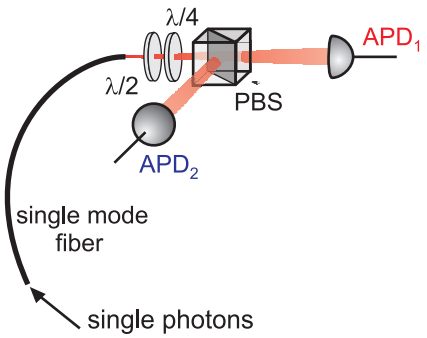


Figure 2.6.: Setup for the polarization analysis of the single photon.

this way we implement the mode filter that guarantees that only such photons are collected that originate from the $\sigma^{\pm}$- decay channels in figure 2.5.

The fiber guides the photons to a setup for the analysis of their polarization state (figure 2.6). It consists of a polarizing beam splitter (PBS) and an avalanche photo-diode in each output port of the PBS. This implements a projection measurement of the polarization state in the $H/V$-basis. Additional $\lambda/2$- and $\lambda/4$-plates in front of the polarizing beam splitter allow for projection in any linear, elliptical or circular basis.

### 2.3.4. Success probability and repetition rate of the state preparation

In the experiment the procedure for producing the atom photon entanglement is continuously repeated until the resulting photon is successfully detected. The overall success probability is determined by the following factors:

- the efficiency of the optical pumping into $F = 1, m_F = 0$ (>90%)
- the efficiency to generate a single photon during the excitation (~ 97%)
- the probability of 2/3 that the photon is emitted into one of the detectable $\sigma$-decay channels
- the probability to collect the single photon with the microscope objective and couple it into the single mode fiber
- photon losses due to absorption in or reflection from optical components (total transmission: ~75%)
- the detection efficiency of the single photon detectors ( 60-65% at 780 nm, according to specifications).

All in all this success probability is about 2‰. It is mainly limited by the effective aperture and quality of the collection optics for the single photons (see section 3.1.2) that allow to collect only a small fraction of all produced photons.

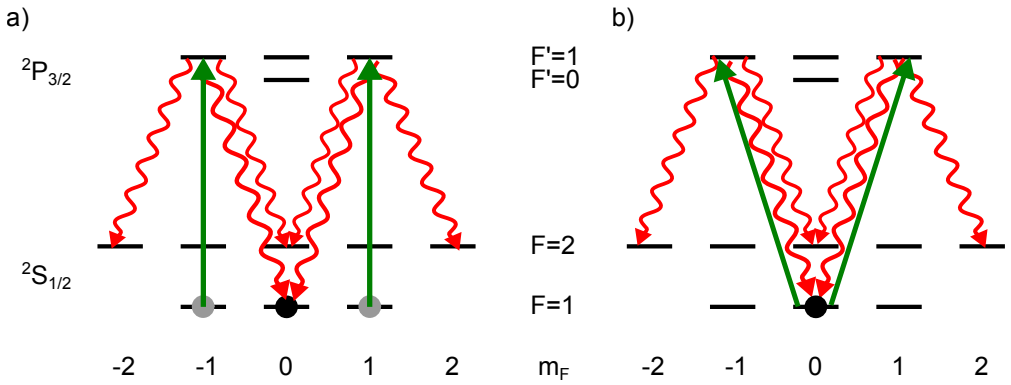


Figure 2.7.: Errors during the preparation of atom-photon entanglement: a) off-resonant excitation of residual population in $m_F = \pm 1$ after imperfect optical pumping. b) off-resonant excitation of population in $m_F = 0$ via $\sigma$-transitions due to a polarization error of the excitation laser. In both cases a detectable $\sigma$-polarized photon can be created via several decay channels.

The optical pumping and excitation of the atom must hence be repeated many times before a single photon is detected. In order to counteract the resulting heating of the atom that is induced by the continuous scattering of photons, this repeated pumping and excitation cycle is interrupted after 40 tries by a 200 µs long cooling period. As a result the effective repetition rate of the atom-photon entanglement procedure (including optical pumping and cooling) is about 50 kHz.

For the given success probability of 2‰ one could thus obtain about one hundred entangled atom-photon pairs per second. However, in experiments that shall characterize the entangled state with the help of the atomic state readout (or characterize the readout itself) the destructive nature of the atomic state readout and hence the necessity to permanently reload the single atom trap limit the event rate to about a hundred events per minute.

## 2.3.5. Sources of error

The effects that limit the fidelity of the presented atomic state preparation can be grouped into two classes: Those which influence the quality of the prepared entangled atom-photon state and those which affect the projection measurement of the polarization state of the photon.

### Errors during the preparation of atom-photon entanglement

In this experiment effects of the first kind occur when the detected single photon does not originate from the intended $\sigma$-decay channels presented in section 2.3.2. On the one hand additional detectable $\sigma$-decay channels will arise if the atom is not excited to the desired state $5^2P_{3/2}, F' = 0, m_F = 0$ but to one of the Zeeman levels of the neighboring $F' = 1$ hyperfine state. Two main sources of error have been identified that allow for such an off-resonant excitation:

- imperfect optical pumping that leaves a residual population in the $m_F = \pm 1$ ground states which allows for off-resonant excitation via $\pi$-transitions to $F' = 1, m_{F'} = \pm 1$ (figure 2.7 a))

- polarization error of the excitation light field such that is has non-vanishing field components perpendicular to the quantization axis. This allows to drive the off-resonant $\sigma$-transitions $F = 1, m_F = 0 \rightarrow F' = 1, m_{F'} = \pm 1$ (figure 2.7 b))

On the other hand the quality of the entangled atom-photon state will also be disturbed if the optical axis of the collection optics does not fully coincide with the quantization axis. In that case one will also collect photons from the $\pi$-decay back to $m_F = 0$.

Except for the contribution from imperfect optical pumping the quality of the entangled atom-photon state thus strongly depends on the precision and stability of the geometrical alignment with respect to the quantization axis. Anyway, in both cases the resulting atomic state lies outside the qubit space and the desired atom-photon entanglement is not obtained.

Several other ways to produce detectable photons via two-fold excitation of the atom within one excitation pulse have been discussed in detail in [43] and are not further listed here.

### Errors during the photonic state projection

The projection measurement on the polarization state of the photon is disturbed by any unwanted rotation of the photon's polarization along the way to the polarization measurement setup. These rotations are induced in the single mode fiber and at any optical component that transmits or reflects the single photon such as the glass walls of the vacuum chamber, the microscope objective, dichroic mirrors etc.

As a countermeasure the birefringence of the fiber is aligned with the help of manual paddle-based fiber polarization controllers such that the net polarization rotation through all components is zero for two complementary input polarizations, e.g. $H$ and $+45°$. This then guarantees that the photon's polarization is preserved for any input polarization.

A prediction of the respective probabilities of all these errors is rather complex. However, a detailed analysis of the experimental results from the atomic state readout in section 5.2.4 will give an upper bound for the summed probability of these errors.

## 2.4. Readout of the atomic state

This thesis focuses on the implementation of an atomic state readout that shall allow to perform a loophole-free Bell experiment. As such, the readout has to fulfill two conditions: It must be fast (<1.3 µs for the given interatomic distance of 400 m) and efficient (i.e. preferably always deliver an answer about the atomic state in every readout attempt).

In the beginning of this section we first discuss the standard option of fluorescence based readouts of matter qubits in order to compare it with the ionization based scheme that is presented in this work - particularly with regard to their suitability for a loophole-free Bell experiment.

### Fluorescence-based state readouts

Previous experiments on atom-photon entanglement and atom-atom entanglement in our group used an atomic state readout that was based on a laser induced Zeeman state selective removal of the atoms from the trap and subsequent determination of the presence of the atom in the trap by the detection of laser induced fluorescence [44]. The result of the fluorescence detection revealed whether the atom had been in a dark state of the previous state selective removal. In that case the atom remained in the trap and could be detected due its fluorescence. Atoms in any orthogonal state of the $F = 1$ ground state were removed and produced no fluorescence. This scheme allowed to close the detection loophole in a Bell experiment with two single atoms [26] since the fluorescence readout always gives one of the two possible answers - either "atom in trap" or "no atom in trap". However, with the given optics for collecting the fluorescence, the photon count rate had to be integrated for at least a few tens of milliseconds [45, 46] to be able to make a definite distinction between "atom in" or "atom out". This makes it impossible to close the locality loophole with a reasonable distance between the two atoms.

The integration time in such a fluorescence detection can be reduced by increasing the photon collection efficiency in several ways. For example, in the loophole-free violation of Bell's inequality demonstrated in [17] the readout of the spin of two entangled nitrogen-vacancy centers in diamond was realized by fluorescence detection. Here the combination of micro-fabricated integrated solid immersion lenses above the diamond defect centers and a microscope objective with a NA of 0.9 allowed for a total photon collection efficiency of 2-3% and hence a duration of the fluorescence readout of 3.7 µs. Thus a distance of 1.3 km was required between the NV-centers which, however, severly limited the event rate to about one event per hour due to transmission losses of the single photons during the entanglement swapping process. In experimental setups with single neutral atoms or ions high numerical apertures and collection efficiencies are generally difficult to achieve. This is mainly due to restrictions imposed by the surrounding vacuum and trap setup. Still, in experiments with single trapped ions and using an intra-vacuum objective (NA=0.4) a photon collection efficiency of 4% has been reported [47]. Later another group even increased the collection efficiency to close to 10% with an out-of-vacuum objective (NA=0.6) [48, 49]. Other experimentally demonstrated alternatives to achieving high collection efficiencies are given by placing the atom or ion in optical cavities [50, 51, 52] and thus benefiting from the resulting preferred photon emission into the eigenmode of the cavity or by enhancing the solid angle of the collection optics with a parabolic mirror around the emitting particle [53]. However, the implementation of all of the mentioned possibilities is technically highly complex. It thus seems worthwhile to explore approaches that do not rely on the efficient collection of fluorescence from the carriers of the quantum state.

### Novel ionization based state readout

The atomic state readout that is presented in this thesis pursues a different approach. It consists of two main steps:

1. The original state-selective removal of the atom from the trap is replaced by a **laser induced Zeeman state-selective ionization** of the atom.

2. The fluorescence detection is replaced by the **detection of the potential ionization fragments** with charged particle detectors.

If no particle is registered at the charged particle detectors after the ionization process, this will be interpreted as a projection of the atom on the dark state of the laser ionization. In contrast the detection of at least one of the ionization fragments will be interpreted as a projection onto the state orthogonal to the dark state which is called the bright state.

With this method - like in the fluorescence based scheme - the detection loophole is intrinsically closed since one always obtains one of the two possible signals “fragment detected” or “no fragment detected”. Of course, all particle detectors will have a limited quantum efficiency. Yet his does not open up a detection loophole, but rather only leads to a fraction of invalid results of the kind “no fragment detected” and hence affects the fidelity of the readout. The key advantage of this scheme is that its duration is mainly limited by the time of flight of the ionization fragments to the detectors which can easily be reduced to a few hundreds of nanoseconds. Hence closing the locality loophole becomes comparably simple.

In the following we present the basic functionality of the two steps of this ionization based readout, discuss possible sources of error and point out the technical requirements for its experimental realization. The setups themselves are going to be described in detail in chapters 3 and 4. We also perform a numerical simulation of the laser induced ionization in order to obtain knowledge about the maximum achievable quality.

### 2.4.1. Zeeman state selective ionization

The ionization process has to distinguish superpositions of the Zeeman-states $m_F = \pm 1$ of the $S_{1/2}, F = 1$ ground state. Figure 2.8 gives a complete overview over the involved atomic states and the necessary laser transitions to perform this process. Shown are all hyperfine and Zeeman states of the $S_{1/2}$ ground state and the $P_{1/2}$ excited state as well as the $F' = 3$ hyperfine level of the $P_{3/2}$ excited state.

The primary goal is to achieve a direct ionization of the atom via a two-photon transition: The atom is first state-selectively excited via $\sigma$-transitions to the intermediate state $P_{1/2}, F' = 1, m_F = 0$ with the so-called readout laser at 795 nm. Simultaneously a second laser pulse at 473 nm is applied that excites the valence electron from the intermediate state above the ionization threshold[2].

The Zeeman state selectivity of this process is realized by choosing the appropriate polarization of the readout laser. For example a $\sigma^+$- polarized readout laser will excite the state $|1, -1\rangle$ (*bright* state), but leave $|1, +1\rangle$ (*dark* state) unaffected since the necessary target state $|P_{1/2}, F' = 1, m_F = +2\rangle$ does not exist. Also off-resonant excitation to $m_F = 2$ in the neighboring $F' = 2$ manifold is at least strongly suppressed due to the large hyperfine splitting of 814.5 MHz.

[2]There is also a laser with a wavelength of 450 nm in use, which, however, makes no substantial difference in this application.

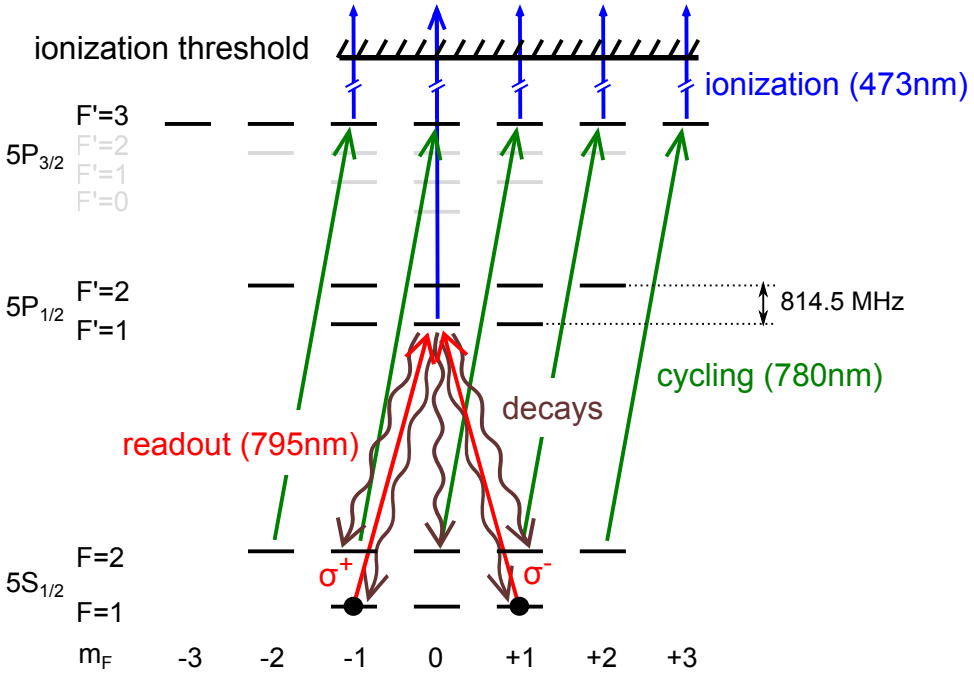


Figure 2.8.: Level scheme illustrating the Zeeman state selective ionization. Depending on the polarization of the readout laser one of the states $|1,-1\rangle$ and $|1,+1\rangle$ - or a corresponding superposition of them - is first excited to $P_{1/2}$ and then ionized. In a small fraction of events the atom decays back into the ground state before being ionized. Atoms that decay back into the bright state can get re-excited by the readout laser. An additional laser (cycling) re-excites atoms, that end up in the $F = 2$ hyperfine state, to $P_{3/2}, F' = 3$ from where they are ionized as well.

| readout polarization | atomic dark state |
|---|---|
| $H$ | $\frac{1}{\sqrt{2}}\left(\|1,+1\rangle + \|1,-1\rangle\right)$ |
| $V$ | $\frac{i}{\sqrt{2}}\left(\|1,+1\rangle - \|1,-1\rangle\right)$ |
| $+45°$ | $\frac{1}{\sqrt{2}}e^{i\frac{\pi}{4}}\left(\|1,+1\rangle - i\|1,-1\rangle\right)$ |
| $-45°$ | $-\frac{1}{\sqrt{2}}e^{-i\frac{\pi}{4}}\left(\|1,+1\rangle + i\|1,-1\rangle\right)$ |
| $\sigma^+$ | $\|1,+1\rangle$ |
| $\sigma^-$ | $\|1,-1\rangle$ |

Table 2.1.: Correspondence between the polarization of the readout laser and the resulting coherent dark state of the atom.

To perform projection measurements onto any superposition of $|1,-1\rangle$ and $|1,+1\rangle$ it is sufficient to choose the corresponding superposition of $\sigma^+$- and $\sigma^-$-polarizations. Table 2.1 lists the resulting coherent dark states [54] of the atom for readout polarizations $H/V$, $\pm 45°$, and $\sigma^\pm$.

By considering the entangled atom-photon states in equations 2.8 and 2.9 one can see that by a projection of the single emitted photon onto the polarization states $H/V$ or $\pm 45°$, the atom gets prepared in the dark state of an $H/V$ or $\pm 45°$-polarized readout laser.

It is instructive to note here that any other state in the $S_{1/2}$ ground state except from the above defined dark state gets ionized by the described laser fields (e.g. also $F = 1, m_F = 0$). Strictly speaking one should hence state that only the detection of no ionization fragments can be interpreted as a projection onto a definite state (the dark state), while the detection of fragments in general only indicates the projection onto any other state. The reliability of the state projection announced by the measurement outcome "fragment detected" thus strongly depends on the ability to restrict the previous preparation of the atomic state to the two-level system spanned by the *dark* and *bright* state.

### Limitations to the readout fidelity

One fundamental limitation for the fidelity of this state readout comes from the fact that the ionization does not happen instantaneously due to the limited intensity of the ionizing laser. As a consequence, with a small probability the atom can decay back into the ground state. This happens with the decay rate $\Gamma_1$ of the $D_1$-transition. Its value is 36.129 MHz corresponding to a lifetime of the excited state of $\tau_1 = 1/\Gamma_1 = 27.68\,\mathrm{ns}$. In the case of a decay back into the bright state the atom gets re-excited by the readout laser and there is a second chance to ionize it. Also atoms that decay into the $F = 2$ hyperfine ground state can be re-excited by the additional cycling laser (780 nm) that drives the closed transition to $P_{3/2}, F' = 3$, from where the atom will be ionized as well. However, atoms that decay into the dark state of the readout laser can no more be excited. Such events reduce the fidelity of the state readout.

To avoid this problem, at first glance it seems advantageous to choose the intensity of the ionization laser as high as possible in order to ionize the atom in a time that is much shorter than $\tau_1$. However, numerical simulations of the entire ionization process (see 2.4.2) predict, that an increasing power of the ionization laser leads to stronger off-resonant coupling of the readout

transition to the neighboring $P_{1/2}, F' = 2$ hyperfine level so that also the original dark state of the readout laser can get excited. The laser power therefore has to be chosen such that the readout yields the maximum contrast in the distinction between dark and bright state.

Other possible sources of error are predominantly of technical nature. One of them are errors of the polarization of the readout laser that can be induced by birefringent components in the beam path. Moreover, the method relies on the fact that only $\sigma$-transitions are addressed. To ensure this, the readout beam has to be fully parallel to the quantization axis. Any angle between the optical axis of the beam and the quantization axis leads to field components parallel to the quantization axis. In that case also $\pi$-transitions are driven and the dark state is partially ionized as well, thus reducing the fidelity of the readout.

### 2.4.2. Numerical simulations of the laser ionization

In order to obtain a prediction about the maximally achievable quality of the state-selective ionization, numerical simulations of this process were performed. A detailed explanation of the entire simulation can be found in [55]. Here we only give a qualitative description and focus on the discussion of the results.

As explained in the previous section there is on the one hand a residual probability that the bright state of the ionization process is not ionized, while on the other hand there is also a non-vanishing probability that the dark state accidentally gets ionized as well. The aim of the simulation is now to determine the dependence of the ionization probability of the bright and dark state of the readout laser on the experimental parameters such as pulse duration and pulse intensity of the involved lasers.

The simulation yields the temporal evolution of the occupation of all concerned atomic states over the duration of the ionization process (see figure 2.8). Starting with an atom prepared in a predefined superposition of the ground states $F = 1, m_F = \pm 1$, the coupling of this atom to the laser fields readout, cycling and ionization is calculated. We consider all resonant dipole transitions addressed by the lasers as well as the off-resonant transition driven by the readout laser that couples the dark state to the $F' = 2$ manifold of the $P_{1/2}$ excited state. The latter is responsible for the unwanted ionization of the dark state. The simulation also includes all possible intermediate spontaneous decays of the excited atom to other ground states and subsequent re-excitation and ionization of the atom.

The action of the ionization laser is modeled as an artificially introduced spontaneous decay channel from the excited states $P_{1/2}$, $P_{3/2}$ into an additional virtual state ("ionization state") that couples to none of the lasers. In this model the intensity of the ionization laser is represented by the decay rate $\Gamma_{ion}$ into this ionization state. It is assumed to be the same for all excited states and is in the following always given in multiples of the decay rate from $P_{1/2}$ to the ground state $S_{1/2}$. This is motivated by the idea that an atom, that has been excited by the readout laser, is desired to predominantly decay into the ionization state rather than back to the ground state, where it might end up in the dark state of the readout laser. One thus expects that $\Gamma_{ion}$ must be larger than $\Gamma_1$ in order to achieve a good quality of the readout.

Throughout the simulations the optical intensity of the cycling laser is kept fix at a value that leads to a Rabi frequency $\Omega_{cycl} = 2\pi \cdot 92\,\mathrm{MHz}$ for the oscillation of the amplitudes be-

tween the ground and excited state (see appendix C). Assuming only coherent dynamics of the populations, this would allow to fully transfer the atomic state to the excited state within $\frac{1}{2}\frac{1}{92\,\mathrm{MHz}} = 5.4$ nanoseconds [3]. In a two-level system with only the decay back to the ground state this power would correspond to $458 \cdot I_{sat}^{cycl}$, with $I_{sat}^{cycl}$ being the standard saturation intensity of the pure cycling transition[4].

The power of the readout laser will be varied. As a reference value we note that - with the given focusing ($w_0 = 10$µm) and without the ionization laser - saturation of the readout transition would be achieved at $P_{sat}^{readout}$=28.2 nW and that for $I = 10 \cdot I_{sat}^{readout}$ half a Rabi oscillation takes 39 ns.

The evolution of the populations is obtained by solving the master equation of the full system. The key results of the simulation are the final occupations of the virtual ionization state in the cases of the bright and dark state as input states.

### Dependence on the intensity and duration of the readout laser

Figure 2.9 shows the final occupation of the ionization state ("ionization probability") as a function of the duration of the readout laser pulse for the two input states "bright state" (a) and "dark state" (b). In this simulation the decay rate into the ionization state was set to $\Gamma_{ion} = 3 \cdot \Gamma_1$.

In the case of the bright state one can see that an increasing power of the readout laser leads to shorter durations of the ionization process. For a power of 0.33 µW the occupation of the ionization state saturates at a value of 97.8% within 105 ns. Even with longer pulse durations this ionization probability cannot be further increased as - according to the simulation - the entire remaining population of 2.2% is trapped in the dark state.

If the atom has been prepared in the dark state, one observes a linear increase of the ionization probability with the duration of the readout pulse. For a power of 0.33 µW 0.80% of the dark state population has been ionized after 105 ns. The calculations show that this linear increase continues also for longer pulse durations.

The key figure of merit of the laser induced Zeeman state selective ionization is the contrast with which the dark and bright state can be distinguished. It is given by the difference of the probabilities to ionize the bright state $p_{bright}$ and the dark state $p_{dark}$.

$$contrast = p_{bright} - p_{dark} \tag{2.10}$$

From the figures it becomes clear that this contrast reaches its maximum at the readout duration, where the ionization probability of the bright state saturates, and will decrease again for longer durations due to the further increasing ionization of the dark state. The resulting contrast of 97.0% for $P_{readout} = 0.33\,\mu\mathrm{W}$ and a pulse length of 105 ns is the maximum value that could be achieved in the simulations among various combinations of readout powers and durations.

[3] With the incoherent decay channels the amplitude of the oscillations is of course damped, but the calculation still gives a good order of magnitude for the necessary laser powers.

[4] In the given situation with the additional decay channel into the ionization state this saturation intensity is, however, no more a meanigful measure for the intensity of the light field as the well known 50/50 distribution between ground and excited state populations for $I \gg I_{sat}$ can never set in.

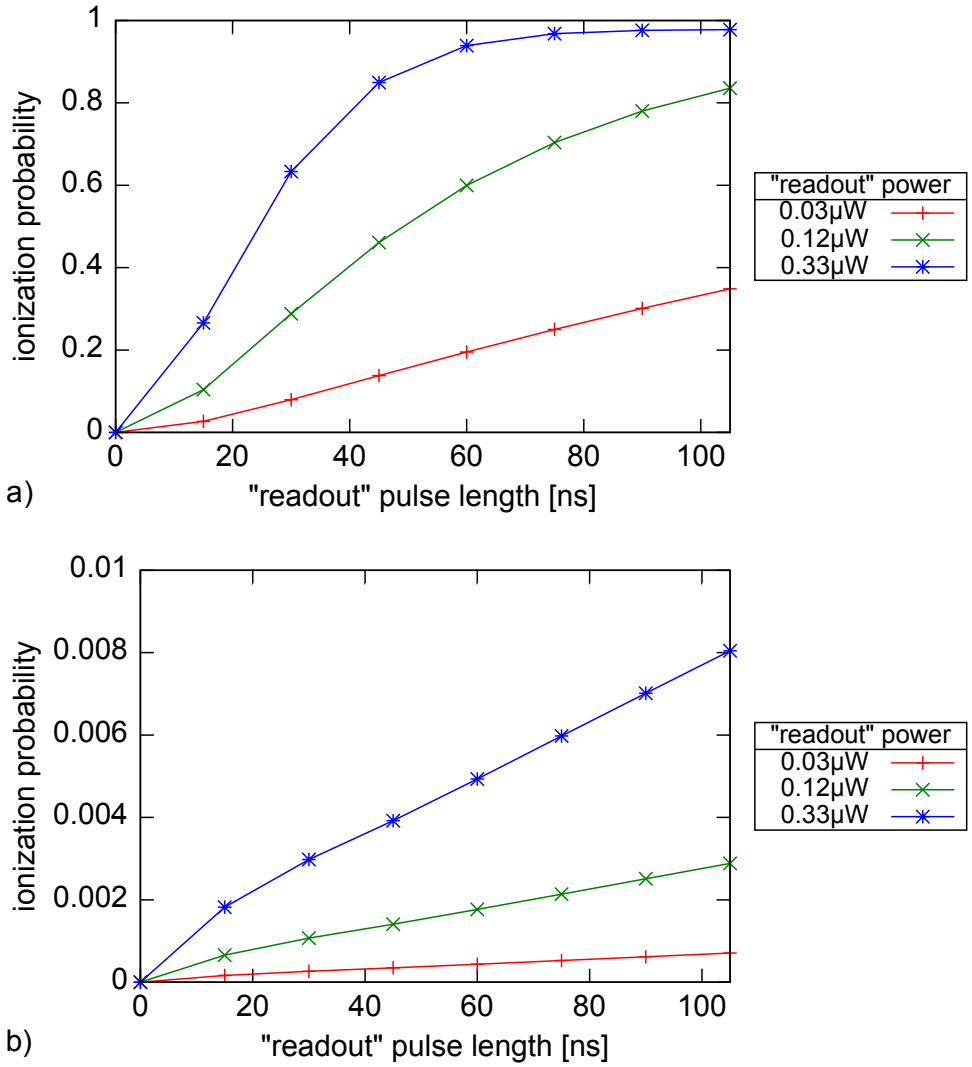


Figure 2.9.: Numerical simulation of the dependency of the ionization probability of the bright state (a) and dark state (b) on the power and duration of the "readout" laser. At sufficiently high powers the ionization probability of the bright state saturates after 100 ns while the undesired ionization of the dark state continues to linearly increase. The overall contrast to distinguish both states thus has its maximum around 100 ns.

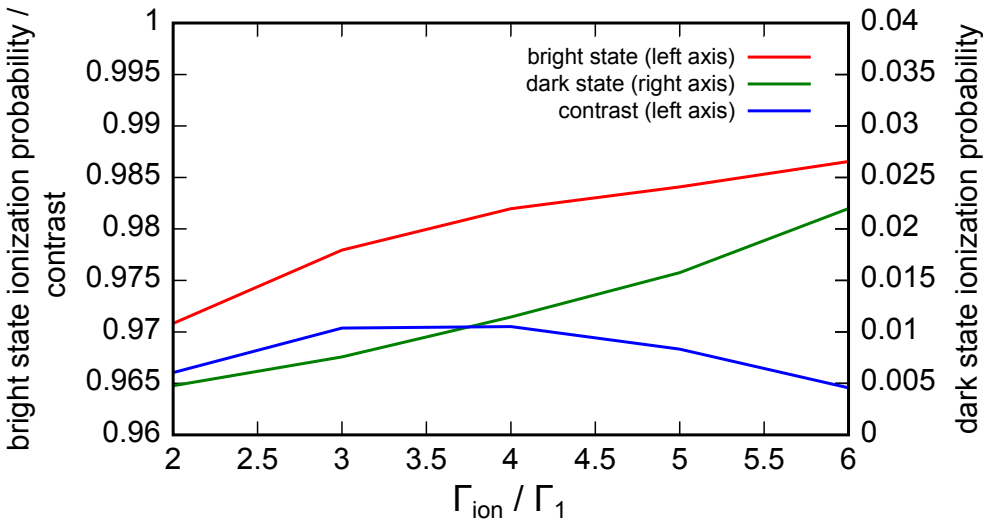


Figure 2.10.: Dependency of the bright and dark state ionization probability and the resulting contrast on the laser power of the ionization laser. The laser power is modeled via the induced decay rate $\Gamma_{ion}$ from the intermediate excited states into the ionized state. The contrast has a maximum for $\Gamma_{ion} = 3...4 \cdot \Gamma_1$.

### Dependency on the intensity of the ionization laser

In the following it is examined whether a further increase of the power of the ionization laser can improve the contrast of the Zeeman state selective readout. For this the simulation is performed for different laser powers. For each value the duration and power of the readout laser were separately optimized in order to achieve the maximum possible contrast.

The result is illustrated in figure 2.10 that shows the bright and dark state ionization probabilities and the resulting contrast for decay rates $\Gamma_{ion}$ ranging from $2 \cdot \Gamma_1$ to $6 \cdot \Gamma_1$. Contrary to the expectations the contrast does not steadily increase with the ionization power. It rather has a clear maximum for $\Gamma_{ion} = 3...4 \cdot \Gamma_1$. At these laser powers the optimum readout pulse duration was 120 ns and 90 ns, respectively. For higher laser powers the increasing ionization probability of the bright state is outweighed by an even stronger increase in the ionization probability of the dark state. By increasing $\Gamma_{ion}$ from $3 \cdot \Gamma_1$ to $6 \cdot \Gamma_1$, $p_{bright}$ increases by only 0.85% while $p_{dark}$ increases by 1.44%. The increase of $p_{dark}$ can be explained by two factors:

- First, for higher ionization powers the optimum contrast is achieved for shorter durations but also higher intensities of the readout laser. If $\Gamma_{ion}$ is changed from $3 \cdot \Gamma_1$ to $6 \cdot \Gamma_1$, the readout pulse has to become two times shorter but also three times more intensive. All in all this favors further off-resonant excitation of the dark state. This effect adds 0.4% to $p_{dark}$.

- Second, a higher ionization power corresponds to a higher decay rate of the excited states into the ionization state. This effectively leads to a line broadening of all transitions into the excited states, again favoring off-resonant excitation of the dark state to $P_{1/2}, F' = 2$.

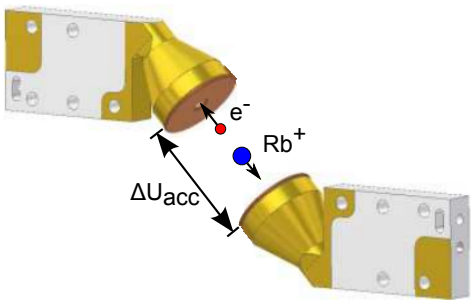


Figure 2.11.: Sketch of the detection of the ionization fragments. The fragments are separated by an electric field and get accelerated into their respective detectors.

As a consequence, in the experiment the ionization laser power is set between $3 \cdot \Gamma_1$ and $4 \cdot \Gamma_1$ where the contrast is expected to be slightly above 97%.

### 2.4.3. Detection of the ionization fragments

The state readout is completed by the detection of the potential ionization fragments. Thus two opposing charged particle detectors are installed around the center of the atom trap (figure 2.11). An electric field that is applied between the entrances of the detectors separates the electron from the Rubidium ion and accelerates each of them into the respective detector. A full description and characterization of this setup will be given in section 4.1 and 4.3.

#### Sources of error

Apart from dark counts of the detectors, the main source of error in this process arises from the non-perfect detection efficiencies of the particle detectors. However, it is sufficient to detect only one of the fragments. This strongly reduces the requirements on the efficiency of the detectors. For example, for a combined probability of 99% to detect at least one of the fragments, a single particle detection efficiency of 90% is already sufficient. As will be seen in chapter 4 this is feasible.

#### Fluorescence detection as a comparative measurement

As an alternative method to determine the outcome of an ionization attempt of a single trapped atom one can continue to use the above described fluorescence detection of the presence of the atom in the trap. The necessary setup for this method is the same that is required for the loading of the trap and the collection of the single photons from the atom-photon entanglement. The fluorescence detection can hence easily be performed in parallel to the detection of the ionization fragments. The method is described in more detail in appendix B.

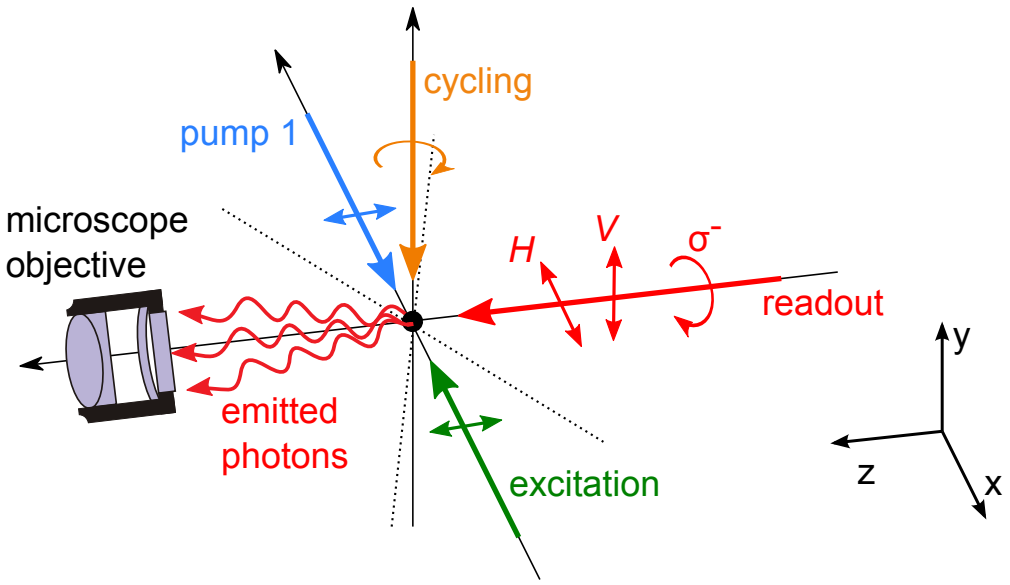


Figure 2.12.: Schematic view of the laser beams around the position of the atom. The microscope objective for the collection of the emitted photons is aligned along the quantization axis $z$. Also the polarization vectors of lasers "excitation" and "pump 1" are parallel to $z$. The polarization of the readout laser, incident along $z$, can be arbitrarily chosen. The cycling laser has circular polarization. Lasers "cooling", "repump" and "pump 2" are not shown here. Their six pairwise counter-propagating beams are incident along the $y$-axis and along two axes in the $x$-$z$-plane with an angle of $\pm 35°$ to the $x$-axis (dotted lines).

## 2.5. Definition of the reference frame

Figure 2.12 gives an overview over the geometric alignment of the laser beams that are directed towards the atom. The $z$-axis of the coordinate system denotes the quantization axis. The polarizations $H$ and $V$ of the single emitted photons from the entanglement procedure are parallel to the $x$- and $y$-axis respectively. The same accounts for the polarizations of the readout laser. Circular polarizations $\sigma^+$ and $\sigma^-$ mean that the photon's spin is parallel and anti-parallel to the quantization axis.

## 2.6. Summary

This chapter gave an overview over the methods needed to create an entangled atom-photon pair and to perform the readout of the atomic state. The atomic qubit is encoded in the $m_F = \pm 1$ Zeeman sublevels of the $S_{1/2}, F = 1$ hyperfine ground state of a single $^{87}$Rb-atom. The single atom is trapped in an optical dipole trap and is laser cooled to below 100 µK. The position of the atom is then fixed to a precision on the order of 1 µm.

After the excitation of the atom with a laser pulse a single photon is emitted from the atom in a

spontaneous decay process. The polarization of the emitted photon is entangled with the Zeeman state of the atom after the emission. This entangled pair is suitable to form the fundamental building block of the envisaged Bell experiment on two entangled atoms at remote locations, as the photonic part of the entangled pair can be transmitted over long distances - thus allowing to perform the entanglement swapping protocol.

The chapter ends with describing the new readout scheme of the atomic state. It consists of two main steps: A laser-induced Zeeman-state selective ionization of the atom and the subsequent detection of the potential ionization fragments with charged particle detectors. It enables projection measurements of the atomic state onto arbitrary superpositions of the two Zeeman states by choosing the appropriate polarization of the readout laser. The atomic state that gets ionized by the laser is denoted the *bright* state, while the state that is not ionized is called the *dark* state. Numerical simulations of the laser ionization process predict that under perfect experimental conditions the maximum contrast, with which two orthogonal atomic states can be distinguished, reaches 97%. Higher contrasts are inhibited by off-resonant transitions, that lead to a partial ionization of the dark state and that are inherently enabled by the configuration of the atomic energy levels.

# 3. Optical setup and vacuum chamber

This chapter presents details on the experimental setup of the single atom trap. A main focus lies on the components that concern the atomic state readout. These are the optics for the readout laser, the fast switching of the laser's polarization and the vacuum chamber together with the modifications that were necessary in order to integrate the charged particle detectors.

During the setup of the new trap special care was taken to avoid sources of error for the state preparation of the atom-photon entanglement as well as the atomic state readout that had appeared in previous trap setups. In more detail this concerns the precision of the alignment with respect to the quantization axis and the issue of birefringence of critical optical components that disturbs the polarization properties of the single photons entangled with the atom, the dipole trap laser beam and the readout laser. To reduce the problems with birefringence a new design of the vacuum glass cell was implemented that allows for a lower birefringence of the cell's walls. Moreover, a temperature stabilization of the entire trap setup was developed in order to reduce temperature induced temporal drifts of the residual birefringence of all optical components.

## 3.1. Optical setup

The entire arrangement of the vacuum and the optical components for the atom trap is situated in a housing with outer dimensions of $2\times1\times1$ meters (figure 3.1). A confocal microscope for trapping and observing the single atom as well as the optical setup for the atomic state readout are installed on the quantization axis $z$ on opposite sides of a vacuum glass cell where the single atom is situated. For more clarity see again figure 2.12 for a schematic overview over the position and directions of the applied laser beams.

During experiments the housing remains closed. The air temperature within the setup is then precisely stabilized in order to avoid temporal drifts of critical components (see section 3.3). All laser sources are installed on a separate optical table and are connected to the trap setup via optical fibers.

### 3.1.1. Laser system

Several laser systems are required for the envisaged experiment. Figure 3.2 gives a schematic overview of the addressed transitions between the involved atomic states.

First of all one needs to be able to drive dipole transitions of the near-infrared $D_1$- and $D_2$-line of $^{87}$Rb to perform the cooling, state preparation and state readout of the atoms. Here it is necessary to resolve the distinct hyperfine levels of the involved states $5^2S_{1/2}$, $5^2P_{1/2}$ and $5^2P_{3/2}$

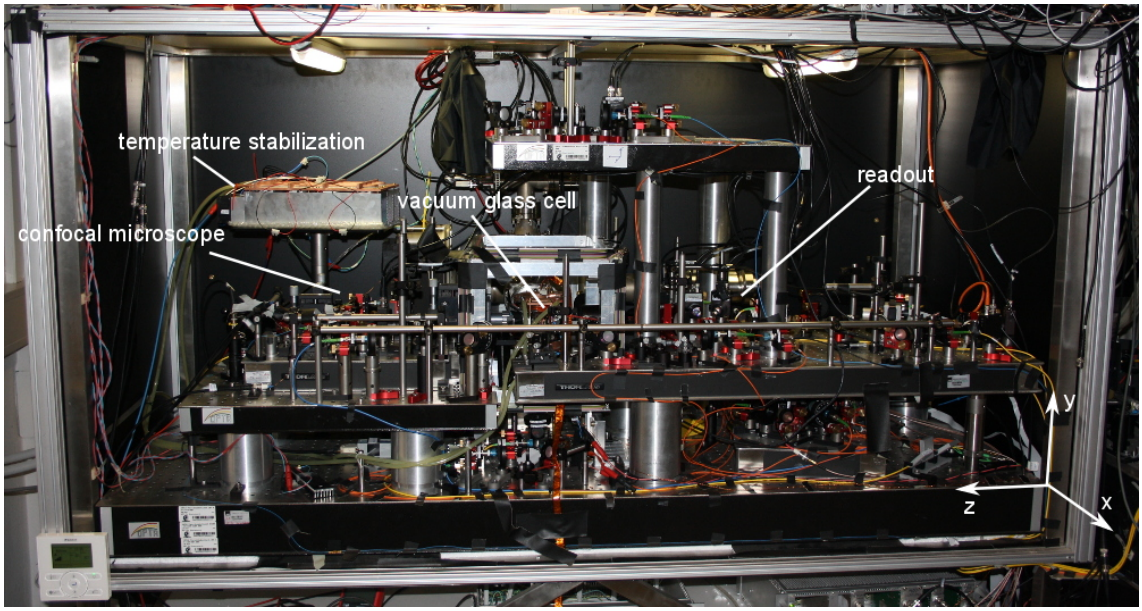


Figure 3.1.: Photograph of the trap setup of "trap 1". The dimensions of the housing are $2\times1\times1$ meters.

with level spacings down to the order of 100 MHz. To achieve this we use tunable grating-stabilized external cavity diode lasers in Littrow configuration [56]. Such lasers show linewidths well below 1 MHz. Their central frequency can be locked to a desired transition using the signal from a Doppler-free saturation spectroscopy of Rubidium atoms in a reference gas cell. Three frequency stabilized diode lasers are used to drive transitions from the $F = 1$ and $F = 2$ ground state to the excited states $5^2P_{3/2}$ (lasers "COOLING", "REPUMP") and $5^2P_{1/2}$ (laser "READOUT"), respectively. After splitting the laser beams into several arms different hyperfine levels in the excited states can be addressed by additionally shifting the laser frequency with accousto-optical modulators (AOM) in each arm. These are also used to switch the beams on and off with rise and fall times of ~20 ns and extinction ratios well above 60dB.

The laser for the optical dipole trap does not require an active stabilization of its frequency. Here a free-running but still longitudinally single-mode laser diode with a wavelength of 852 nm is used.

For the ionization laser two different laser diodes at 450 and 473 nanometers are in use[1]. They are as well not frequency stabilized and show a strongly multi-mode spectrum with a typical total width of about 2 nanometers. As the ionization laser does not address distinct levels but rather

[1]Nichia, NDB 4116 and NDA 4116, optical output power for continuous operation: 100 mW. In order to achieve the necessary intensities during the maximally 500 ns long pulses, the laser diodes are driven with up to four times the specified maximum currents. This is achieved using the pulsed current sources LDP-V 03-100 UF3 from PicoLAS. Between the ionization events the diodes are entirely switched off. The maximum duty cycle that is applied during the alignment of the beam line is of several tens of pulses per second. During the experiment the duty cycle is of about 1 per second. No degradation of the laser power has been observed after an estimated total number of pulses of $10^6$-$10^7$.

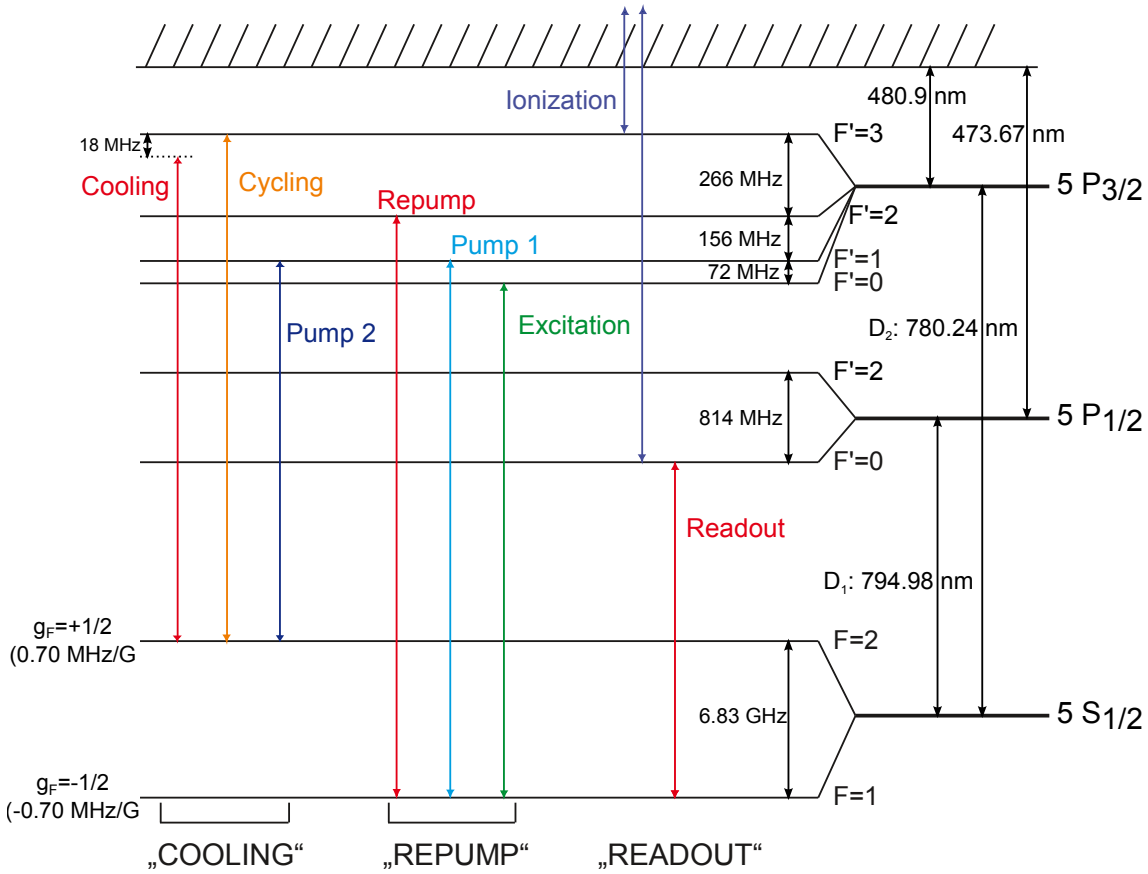


Figure 3.2.: Overview over all dipole transitions driven by the diode lasers. Beams derived from the diode laser "COOLING" drive the transitions on the $D_2$-line starting from the $F = 2$ ground state, laser "REPUMP" those starting from the $F = 1$ ground state. The beam from "READOUT" is resonant to the $D_1$-transition starting from $F = 1$. Also shown is the unstabilized ionization laser.

couples to the continuum, this does not pose a problem to the fidelity of the state readout. The lasers are used to ionize atoms that have been excited to $5^2P_{1/2}$ or $5^2P_{3/2}$ by the readout laser. The optical power after the fiber and at the entrance of the focusing objective in the confocal microscope is 251 mW, considering the transmission of the objective (85%) and the glass cell (95%) one obtains ~200 mW at the position of the atom. For the experiments in section 4.3 that require a continuous laser beam a diode pumped solid-state laser (DPSS) with a wavelength of 473 nm was used.

All laser beams are transversally single mode and can hence be efficiently coupled into single mode optical fibers that guide them to the trap setup.

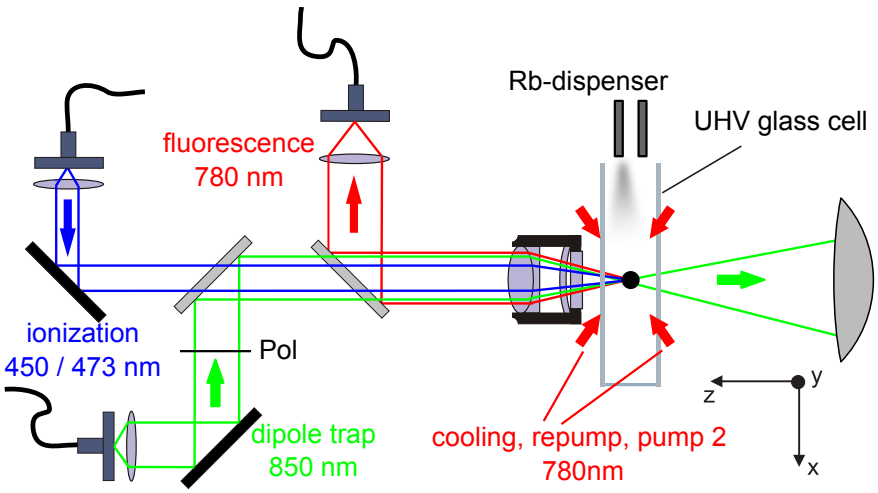


Figure 3.3.: Optical setup of the confocal microscope for the single atom dipole trap. Dichroic mirrors overlap the beam paths of the dipole trap laser, the collection optics for the fluorescence photons from the single atom and the ionization laser for the atomic state readout. Their common focal spot lies in the center of a vacuum glass cell. The optical axis of the objective defines the quantization axis $z$.

### 3.1.2. Confocal microscope for the atom trap and fluorescence detection

Figure 3.3 shows a drawing of the confocal microscope for the single atom trap. A microscope objective[2] focuses the laser beam of the dipole trap to the center of an ultra-high vacuum glass chamber. The optical axis of the objective is aligned along the $z$-axis (i.e. the quantization axis of the experiment). Two pairs of counter-propagating cooling and repump beams that irradiate the trap center lie in the horizontal $x$-$z$-plane. Another pair of counter-propagating cooling beams is applied along the vertical $y$-axis.

Photons emitted from the single atom by scattering of cooling light or after the excitation during the atom-photon entanglement are collected by the same objective. They are then separated from the dipole trap laser's beam path with a dichroic mirror and coupled into the single-mode optical fiber that guides them to the single-photon detectors. Also in confocal configuration with the dipole laser is the ionization laser that is used during the ionization based readout of the atomic state.

The dimensioning of the imaging parameters is governed by the aim to obtain the maximum collection efficiency for the photons emitted by the atom. The objective is specified to provide diffraction limited imaging up to a numerical aperture of 0.5, however, only in the visible spectrum. Thus the full performance cannot be reached with the near-infrared wavelengths of the trap laser and the fluorescence collection, leading to a lower effective NA. The system is set up in the following order:

[2]Mitutoyo, G Plan Apo 50, NA=0.5, corrected for a glass plate with a thickness of 3.5 mm between the objective and the focal spot.

| | waist | angle of divergence | used NA | $M^2$ |
|---|---|---|---|---|
| fluorescence collection | 1.00 µm | 15.5° | 0.267 | 1.1 |
| trap laser | 1.92 µm | 8.1° | 0.14 | 1.0 |
| ionization laser | 1.07 µm | 7.4° | 0.13 | 1.0 |

Table 3.1.: Imaging parameters of the three Gaussian beams in the confocal microscope. The trap laser is focused to about twice the diameter of the focus of the fluorescence collection. The ionization laser has about the same diameter as the fluorescence collection.

1. First one determines the minimum possible diameter of the focal spot for the fluorescence collection, i.e. the maximum usable aperture of the objective, so that the maximum amount of fluorescence is efficiently coupled into the Gaussian mode of the optical fiber. For this we send laser light at 780 nm backwards through the optical fiber for the fluorescence collection and chose the focal length and longitudinal position of the collimation lens at the fiber's output coupler such that the Gaussian waist in the focus of the objective is minimal but still diffraction limited. The diffraction limited imaging of the fiber mode is verified in a $M^2$ measurement of the beam profile with the knife edge method [57, 46].

2. After this the focal waist of the trap laser is chosen. It must be small enough to guarantee the blockade effect necessary for trapping of single atoms and to allow for a spatial confinement of the atom well below the waist of the fluorescence collection optics (see equations 2.3 and 2.4). However, a too strong focusing of the beam leads to increasing longitudinal polarization components [40] resulting in undesired elliptic polarization.

3. Finally the focal waist of the ionization laser is focused as strongly as possible to maximize the laser intensity at the position of the atom.

Table 3.1 lists the beam parameters of the confocal microscope setup. From the angle of divergence $\theta$ of the beams obtained from the $M^2$ measurement we calculate the actual numerical aperture for each beam via $NA = \sin\theta$. The maximum usable numerical aperture for the fluorescence collection was found to be 0.267.

### 3.1.3. Zeeman state selective readout

Since ideally the readout laser must drive $\sigma$-transitions only, it is applied along the quantization axis. The optics for focusing the beam is hence placed on the side opposite to the position of the confocal microscope (figure 3.4). During experiments that examine the atom-photon entanglement and the atomic state readout we employ retarder plates ($\lambda/2$ and $\lambda/4$) to set the laser's polarization to $\sigma^+/\sigma^-$ or any of their superpostions. For the loophole-free Bell experiment that requires a fast switching of the measurement basis we use two laser beams with appropriate predefined polarizations (set by polarizers 1 and 2) and overlap them at a beam splitter. The measurement basis is then set by quickly switching on the power in the laser beam with the desired polarization (see section 3.1.4).

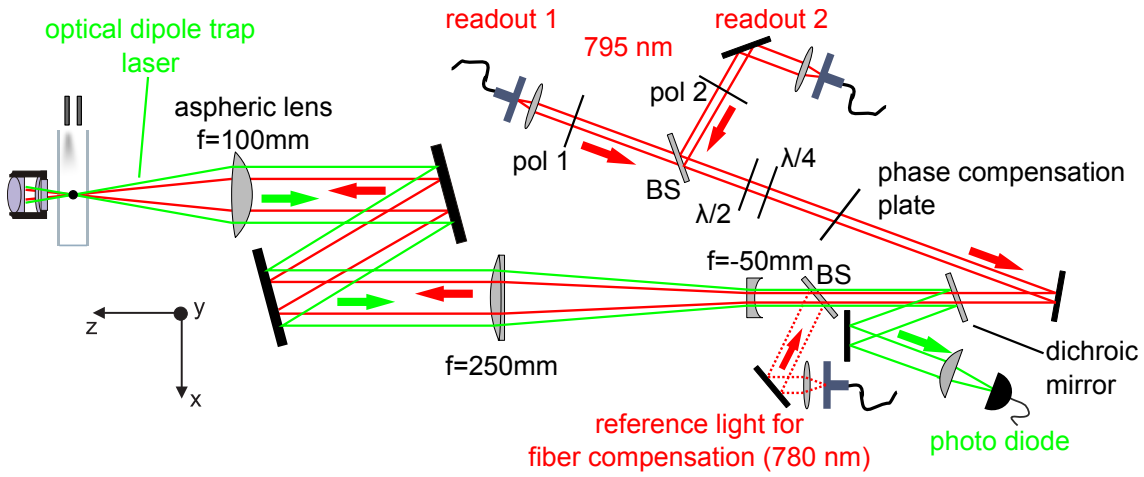


Figure 3.4.: Optical setup for setting the polarization of the readout laser and focusing it onto the single trapped atom.

Originating from a single mode optical fiber with a beam diameter of $2w = 1\,\mathrm{mm}$ after the output coupler of the fiber, the beam is first expanded in a 5:1 telescope and then focused onto the atom with an aspheric lens[3] with a focal length of f=100 mm. The calculated beam diameter at the position of the atom is then $2w_0 \approx 20\,\mu\mathrm{m}$. In order to ensure a good overlap of the beam with the trap position and the quantization axis, two mirrors in front of the aspheric lens are used to couple the readout beam into the fiber for fluorescence collection of the confocal microscope (see section 3.1.2).

The focusing lens also collimates the beam of the optical dipole trap originating from the opposite side of the vacuum cell. The trapping laser is decoupled from the readout laser's beam path with a dichroic mirror and sent to a photo diode for measurement and stabilization of its power. Additionally, a 50:50 beam splitter is used to insert a laser beam at 780 nm that is coupled into the opposing fiber for the fluorescence collection. This reference light is used to adjust the birefringence of this fiber.

### Polarization errors of the readout laser

Phase shifts between the orthogonal polarization components of the readout laser that are induced by birefringent components along the beam path are compensated with an additional phase plate[4] that is tilted around the vertical axis. Moreover, the mirrors and beam splitters generally show different reflectivities for s- and p-polarizations (i.e. $H$ and $V$). This, however, cannot be corrected for with unitary transformations as e.g from phase plates. In order to minimize both effects - phase shifts and differences in reflectivities - from the beginning, we choose silver coated mirrors instead of dielectric mirrors and use them under small angles of incidence. Also the angles

[3] Asphericon, A50-100LPX-S-B

[4] We use a zero order $\lambda/2$-waveplate for 795 nm. Its ordinary and extraordinary axes are aligned parallel to $H$ and $V$.

of incidence of the beam splitters and the dichroic mirror were chosen such that the reflectivities for s- and p-polarization are equal.

In order to quantify the residual polarization errors in the setup we first measure its transmission for $H$- and $V$-polarized light from the fiber couplers to the output of the microscope objective. We find the relative difference between the two transmissions to be 3.8%. This difference alone causes a rotation of an initially $\pm 45°$-polarized laser field in the linear plane by 0.55° which would lead to an extinction ratio of 1/9200 at a $\mp 45°$ polarizer. To determine the overall disturbance of a linearly polarized laser beam including the ellipticity resulting from birefringence we measured its extinction at a crossed polarizer. After proper alignment of the phase compensation plate we find it to be 1/4500 for input state $V$ and 1/15000 for input state $+45°$. From this we derive a maximum polarization error of 0.85° and ~0.47°, respectively.

## 3.1.4. Fast switching of the atomic measurement basis

To close the locality loophole in a Bell-experiment one requires a fast method to switch the measurement basis of the state readout at each particle between two preselected values. For each system there is a set of two basis pairs - one for each observer - that leads to a maximum violation of the CHSH inequality. In our case the measurement basis is defined by the polarization of the readout laser and a maximum violation can for example be achieved for the two pairs of linear polarizations $\{0°, +45°\}$ and $\{-22.5°, +22.5°\}$ [26].

In this experiment we reserve a maximum time window of 300 ns to set the correct polarization once one of the two measurement bases has been selected by a random number generator. Concerning the quality of the readout laser's polarization we estimate that the extinction of the laser at a polarizer that is rotated by 90° with respect to the desired basis should not exceed 1/3000, corresponding to a polarization error of 1°. In preparation of the Bell-experiment two methods for the fast setting of the measurement basis have been tested. In the following we first briefly discuss the dismissed option of switching the polarization with the help of electro-optical modulators and then present the implemented method of using acousto-optic modulators.

### Switching with electro-optic modulators

Electro-optic modulators (EOMs) are the most common solution for applications where a fast switching of polarizations is required. EOMs are based on the Pockels effect in a birefringent crystal where the indices of refraction of the ordinary and extraordinary axis can be modulated by applying a high voltage to the crystal [58]. The EOM then acts like a waveplate with an adjustable retardance that is determined by the amplitude of the applied high voltage. Its bandwidth is practically only limited by the employed high voltage source and the latter's capability to drive the input capacitive load of the EOM at the given input impedance.

As the pulsed high voltage source we used a PVM 4210 from Directed Energy Inc. with a maximum output voltage of 950 V and a 10%-90% rise and fall time below 15 ns. It has a throughput delay from the leading edge of the gate pulse to the leading edge of the output pulse of 93 ns - thus leaving slightly more than 200 ns to settle to the desired output voltage within the envisaged total time window of 300 ns. Other important parameters in this context are the pulse

over- and undershoot (<5%) and the pulse droop (<1%) that both determine the stability of the output voltage after the switching[5].

In total three different EOMs have been tested with this high voltage source. However, with none of them we were able to obtain the necessary stability of the output polarization within a few hundred nanoseconds after the switching of the high voltage. The main reason for this is a piezoelectric ringing of the birefringent crystal induced by the fast switching of the applied high voltage. This leads to a periodic oscillation of the crystal's indices of refraction and hence of the output polarization. In a first attempt with an EOM made from a Lithium Niobate ($LiNbO_3$) crystal[6] an oscillation of the extinction of the output polarization around values worse than 1/1000 for a duration of more than 100 µs was observed [59]. The oscillations had a period of 500 ns - in good agreement with calculations of the expected acoustic resonances of the crystal. To avoid the piezoelectric effect two other EOMs were tested: An EOM made from Rubidium-Titanyle-Phosphate[7], a material that is considered to show low acoustic ringing, and one made from Potassium Dideuterium Phosphate of which the crystal geometry has been optimized for strong damping of the acoustic ringing[8]. Yet also these EOMs showed a comparable behaviour and did not deliver the required quality and stability of the polarization within the desired time window.

### Switching with acousto-optic modulators

As a consequence of the insufficient performance of the electro-optical modulators we chose a different option: We prepare two laser beams with the polarization in each of the beams being fixed to one of the desired measurement bases by a polarizer and overlap their beam paths at a non-polarizing beam splitter (see figure 3.4). For a high purity of the polarization one then requires a means to switch the beam with the required polarization on while keeping the other beam off with a high on/off optical power ratio.

This can be easily achieved by using acousto-optic modulators (AOMs). These are based on the acousto-optic effect that allows to induce a periodic modulation of the index of refraction in an appropriate transparent glass or crystal by applying radio-frequency sound waves to this material with the help of a piezoelectric transducer [58]. The modulated index of refraction then acts as a Bragg grating that splits the laser beam into several diffraction orders with the laser frequency in the $\pm$n-th order being shifted by $\pm$n times the radio-frequency. Typically up to 90% of the incoming light can be diffracted into the $\pm 1^{st}$ diffraction order (depending on the orientation of the grating with respect to the beam axis). Hereby the on/off ratio of the optical power in the diffracted arms is only limited by the electric on/off power ratio of the radio-frequency source.

However, the response time of the AOMs, i.e. the time delay between the electric pulse arriving at the piezoelectric transducer and the rise of the optical power in the diffracted arms to its

[5] All specified values are given for a connected load capacitance of 100 pF
[6] Thorlabs, EO-PM-NR-C1, input capacitance load of 14 pF
[7] Leysop, RTP-4-20-AR650-1000
[8] Conoptics, 350-50 with option BK for minimized piezo-electric resonances

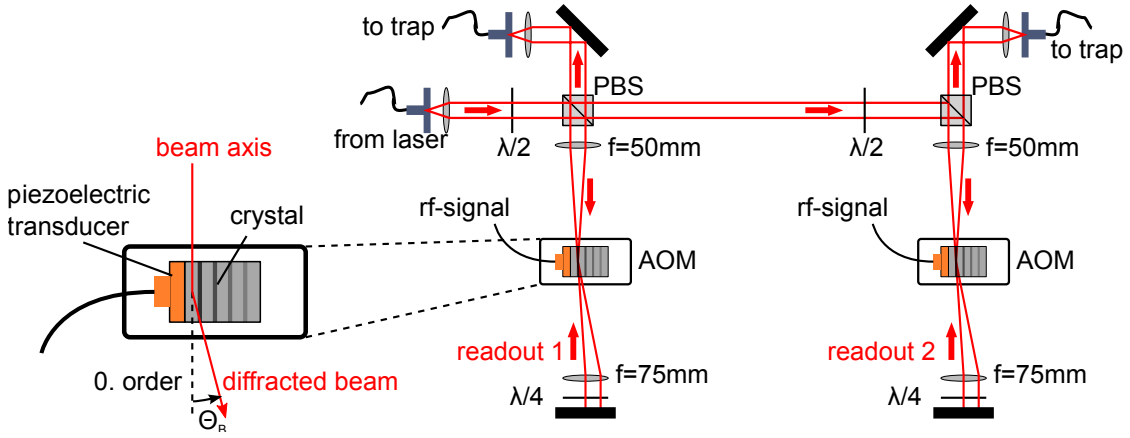


Figure 3.5.: Acousto-optic modulator setup for fast switching of the lasers readout 1 and readout 2. The readout laser is split into two arms at a polarizing beam splitter and is then sent to two separate AOMs in double pass configuration. The AOMs' alignment has been optimized for a fast response time by the appropiate focusing of the laser beams and by passing the beams close to the piezoelectric transducer of the AOM.

maximum value, is limited by the speed of sound $v$ of the acoustic wave within the crystal. Two measures have to be taken to minimize this response time:

- In order to reduce the delay between the electric and the optical pulse the laser beam within the AOM has to be aligned as close as possible to the piezoelectric transducer.

- In order to reduce the rise time of the laser pulse intensity it is advantageous to focus the beam at the position of the AOM to a small diameter.

Figure 3.5 shows the setup of the acousto optical modulators. The laser beams pass the AOMs two times in order to increase the on/off ratio to well below 60 dB and are then coupled into single mode fibers that guide them to the trap. After each pass residual power in the $0^{\text{th}}$ diffraction order is blocked at apertures on both sides of the AOM. To allow for a high-bandwidth power modulation of our lasers we select AOMs with a high carrier drive frequency of 350 MHz [9]. The actual driving frequency in our setup is set to $f = 408$ MHz such that the resulting laser frequency is resonant to the desired atomic transition. The crystal in the AOMs is made of TeO2 in which the speed of sound is $v = 4200$ m/s, i.e. the acoustic wave takes 24 nanoseconds per 100 µm. To reach short rise times of the optical pulse we chose the focusing lens in front of the AOM such that we obtain a diameter of the focal spot of $2w_0 \approx 25$ µm. The corresponding laser beam divergence of $\theta = 1.2°$ is then already on the order of the AOM's Bragg angle $\theta_B = \frac{\lambda f}{v} = 1.1°$. This results in a strong but still tolerable reduction of the diffraction efficiency to ~30-40% for a single pass through the AOM.

[9] AOMs in this setup: AA Optoelectronic MT350-A0.12-800 and Gooch&Housego 3350-199

| | time [ns] |
|---|---|
| electric drivers and cables | 15 ns |
| delay within AOM | 140 ns |
| rise time of AOM (0-90%) | 5 ns |
| optical path to trap | 25 ns |
| | **$\Sigma$ =185 ns** |

Table 3.2.: Time budget for switching on the readout lasers. The overall delay between the electric input pulse at the AOM's driving electronics and the arrival of the optical pulse at the atom is 185 ns.

We measured the overall minimum delay between the electric pulse at the input of the AOM's driving electronics and the arrival of the optical pulse at a photodiode at the trap setup. It was found to be 185 ns. From the knowledge of the delays in the electronics, in cables and optical paths we derive that the delay due to the propagation of the acoustic wave in the AOM is of about 140 ns. This means that the laser beam should be at a distance of about v·140 ns = 600 µm from the piezoelectric transducer. Table 3.2 summarizes the contributions to the switching time of the readout laser beams.

## 3.1.5. Alignment with respect to the quantization axis

As stated in 3.1.2, the quantization axis of the experiment is defined by the optical axis of the microscope. There are three optical beams that have to be well aligned with respect to the quantization axis - the polarization of the excitation laser that is applied during the preparation of atom-photon entanglement, the optical mode of the fluorescence collecting fiber and the readout laser. In the following we give estimates about the precision of these alignments.

### Polarization of the excitation laser

In order to achieve a high quality of the atom-photon entanglement, the excitation laser must drive a $\pi$-transition, its electric field vector must hence be parallel to the quantization axis. For this the angle between the beam axis and the quantization axis must be 90° and its polarization must be $H$. We determined the error of the beam direction with respect to the housing of the microscope to be below 0.3° and the deviation of the polarization from $H$ to be below 0.5° - limited by the precision of the alignment of the used polarizers with respect to the horizontal plane.

### Collection of entangled photons

In order to only collect photons from decays via $\sigma$-transitions during the atom-photon entanglement (see section 2.3.2) it is crucial that the spatial mode originating from the fluorescence collecting fiber is parallel to the objective's optical axis at the position of the atom trap. To verify this we determine the transverse position of the mode center with respect to the quantization axis

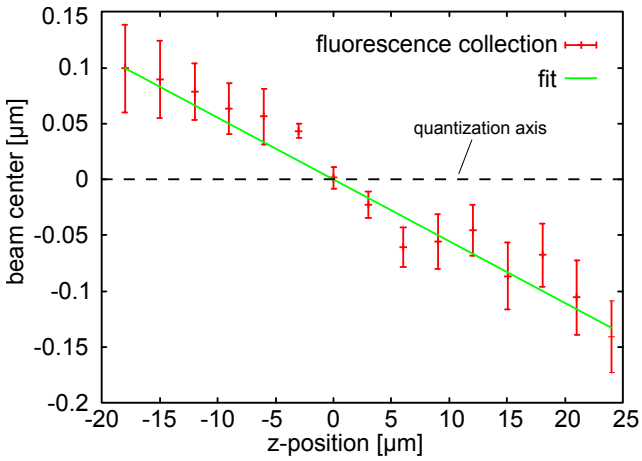


Figure 3.6.: Transverse deviation of the mode of the fluorescence collecting fiber with respect to the optical axis of the microscope objective (quantization axis $z$) at the position of the objective's focus. The angle between the fitted straight line and the quantization axis is 0.32°.

(as obtained during the $M^2$-measurements in 3.1.2) as a function of the $z$-position. Figure 3.6 shows the resulting plot. A linear fit of the data yields a residual angle of 0.32° between the fiber's mode and the quantization axis. Repeated measurements of these data over the course of two days revealed drifts of this angle below 0.2°.

### Readout laser

The readout laser is overlapped with the quantization axis by coupling it into the opposing fiber for fluorescence collection in the confocal microscope. However, since the diameter of the readout laser is not matched to the mode of the fluorescence collection, the fiber coupling efficiency is low and does not provide a sharp criterion for the geometric overlap of the two modes. The resulting inaccuracy of the readout laser's angle with respect to the quantization axis is estimated to be on the order of 1°.

## 3.2. Vacuum setup and glass cell

To operate a magneto-optical trap as well as a single atom dipole trap an ultrahigh vacuum (UHV) environment is required in order to minimize collisions with atoms and molecules from the background gas. The vacuum setup must also house the charged particle detectors for the atomic state readout which are placed close to the atom trap and can as well only operate under high vacuum conditions. Since all operations for the trapping of the atom as well as the state preparation and readout are performed with lasers, a good optical access to the trapping region from all sides is necessary. The atom trap along with the detectors are thus situated in a glass cell that is attached to the UHV system.

In this work the charged particle detectors have to be combined with a single atom trap. This makes several modifications of the vacuum setup necessary. In particular it would be advantageous to be able to shift the volume of optimal detection efficiency in order to optimize its overlap with the position of the single atom trap without having to move the whole detector setup. Since this volume is defined by electric fields accelerating the charged particles onto specific spots of the detectors, additional electrodes which will be discussed in the following are needed to finetune the electric field configuration of the detectors. Tuning perpendicular to the quantization axis is possible with simple electrodes made of copper plates. To maintain the optical access along the quantization axis, electrodes along this direction are implemented with an optically transparent and electrically conductive indium tin oxide (ITO) coating on the inner walls of the glass cell.

This section starts with a brief overview of the vacuum setup. It continues with the main design considerations for the construction of the glass cell with the conductive coating. We then explain the assembly of the cell and how to electrically contact the coating with expoxy glues. In the end we describe the method to attach the glass cell to the vacuum system and characterize its birefringence.

### 3.2.1. Overview of the vacuum setup

Figure 3.7 gives an overview of the vacuum setup: The glass cell where the experiment takes place is attached to an ultrahigh vacuum system of standard CF-components made of non-magnetic stainless steel (type 316L and 316LN). A tee piece attached to the glass cell houses the Rubidium dispensers. The latter is connected to a 5-way cross. Here an UHV valve allows to attach a turbopump with which the setup is first evacuated and that pumps away gases that are emitted during the bakeout of the vacuum system. Once the bakeout is finished the valve is closed and an ion-getter pump (Varian, UHV-24p) is used to further decrease and maintain the pressure. With this pump a pressure of $2...5 \cdot 10^{-10}$ mbar is achieved.

The vacuum setup also incorporates electrical feedthroughs for the high-voltage power supply of the charged particle detectors and their output signals as well as additional voltages for the electrodes that are used for finetuning of the transverse electric field configuration.

A glass window in the rear side of the cross provides additional optical access to the trapping region from behind which is used during the optical pumping.

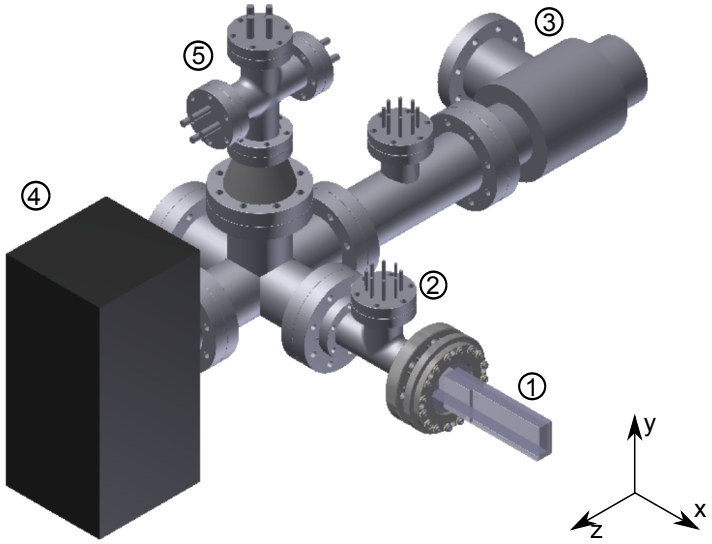


Figure 3.7.: Vacuum setup: The experiment takes place in a glass cell (1) that is attached to an ultahigh vacuum system incorporating Rubidium dispensers (2), a vacuum valve (3), an ion getter pump (4) and high-voltage feedthroughs (5).

## 3.2.2. Design considerations for the glass cell

Apart from geometrical considerations two major requirements influenced the design of the glass cell of this experiment:

### Minimization of birefringence

The cell must exhibit a birefringence as low aspossible. This is on the one hand important for preserving the polarization of the photons from the entangled atom-photon pair leaving the cell. On the other hand it is important for the readout laser since its polarization defines the measurement basis of the atomic state readout. Moreover, the laser of the optical dipole trap must be perfectly linearly polarized, otherwise the degeneracy of the qubit states of the trapped atoms is lifted (see section 2.2.2). Birefringence of the glass wall might render its polarization elliptical.

Problems with birefringent glass cells appeared in previous designs of both trap setups of this experiment and e.g. their impact on the polarization of the optical dipole trap and coherence properties of the qubits has been examined [60]. In both setups a vacuum sealing was achieved by pressing the open rear side of the cell against a steel flange at the vacuum system with the help of a stamp on the cell's front face (for a detailed description of this setup see appendix D.1 or [28]). This induced strong mechanical stress and hence birefringence along the whole glass cell. A calculation of the expected birefringence with this system can be found in appendix D.1 and is in good agreement with measured rotations of the polarization. In general it is possible to compensate birefringence of optical components with additional birefringent phase plates in

the beam path. However, the stress that induces birefringence is usually temperature dependent which makes its compensation over long periods of time difficult. It is thus desirable to reduce the absolute birefringence to a minimum in order to also minimize the magnitude of its drift.

To circumvent this problem the open rear side of the glass cell is now bonded to a glass flange which in turn is used to attach the cell to the vacuum chamber. In this way the walls of the cell itself remain free of mechanical stress which leads to low birefringence as shown in section 3.2.8.

### Well-defined electric environment

The dielectric surfaces of the glass cell can pose a problem for the collection of the ionization fragments during the atomic state readout. Patch charges that might accumulate on the walls and that will not be neutralized under vacuum conditions can lead to a time variant distortion of the electric field used to collect the ionization fragments. This would lead to unstable collection efficiencies and thus deteriorate the fidelity of the state readout. Similar problems with patch charges on dielectric surfaces in vacuum are well known for example in ion trap setups and have been systematically studied meanwhile (see e.g. [61]).

To avoid this problem the walls of our glass cell are coated with an electrically conductive indium tin oxide (ITO). The coating is contacted with cables that allow not only to prevent accumulation of charges on the surfaces but also to apply defined voltages and thus use them to tune the field configuration between the charged particle detectors in a controlled way.

### Resulting design

Figure 3.8 shows a technical drawing of the cell with the glass flange. The entire glass cell was manufactured by Hellma Analytics out of high quality fused silica (Suprasil® by Heraeus). The walls of the cell are 3.5 millimeters thick[10] and its inner dimensions are of 15x35x136.5 mm. Since the temperatures necessary for the bonding process would greatly exceed the temperature resistivity of the coating (max. 200°C), the latter has to be applied after manufacturing of the cell. For this reason the cell is left open on one side in order to have access to its inner walls. A separate glass window of the appropriate size is then glued onto the open side after the coating (see following sections).

All accessible surfaces of the cell have been ITO-coated. Only the small inner walls were not accessible, but were also left uncoated deliberately in order to inhibit a short circuit between the two opposing large walls that are to be used as electrodes. Special care was also taken to leave those surfaces uncoated where the window is going to be glued onto the cell. These are the rims of the side walls of the cell as well as a margin of 4 mm around the window. In addition edges of the window on the vacuum side are not beveled as this increases the risk of a leak (see the red marked spot in figure 3.8).

[10] The used objective of the confocal microscope is corrected for a glass plate of this thickness between the objective and its focal spot.

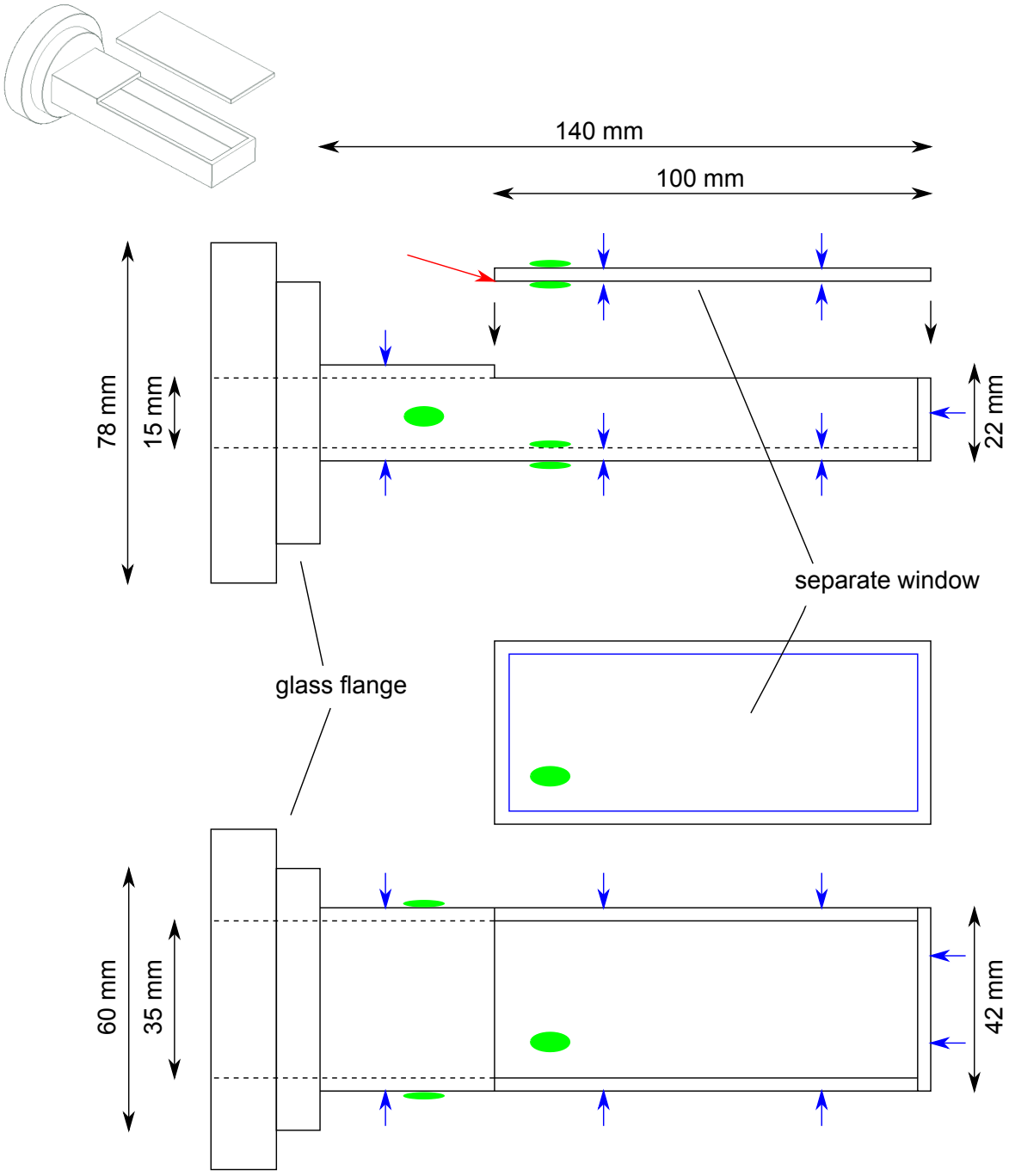


Figure 3.8.: Drawing of the ultrahigh vacuum glass cell. The open side of the cell is closed with a separate window. The thickness of all walls is 3.5 mm. A stepped glass flange is directly bonded to the cell for connection to the vacuum system. Blue arrows mark the surfaces with the electrically conductive indium tin oxide coating. The green spots indicate the positions where the coating is electrically contacted. The edge indicated by the red arrow is not beveled.

### 3.2.3. Indium tin oxide (ITO) coating

The electrically conductive coating is realized with an indium tin oxide (ITO) layer that was applied on the glass cell by physical vapor deposition. ITO is a semiconductor with a band gap of $\approx 4\,\mathrm{eV}$ [62] which makes it transparent over the whole visible and near infrared spectrum. This beneficial optical characteristic explains its widely spread use as screen electrode on touch displays or in liquid crystal displays. Our coating (Iralin™ 185L by Optics Balzers) has a sheet resistance of ≈1 kOhm/sq [11]. Since we intend to apply only static voltages to the electrodes a lower resistance is not necessary and also not desired as it comes at the price of reduced transparency due to the increased concentration of charge carriers.

Another important property in our context is the work function i.e. the energy that is needed to remove an electron from the ITO layer as it might happen in our experiment via the photoeffect due to illumination with the 450 nm ionization laser. The resulting stray electrons could lead to dark counts on the electron detectors during the atomic state readout. The provider of the coating was not able to specify this quantity. However, the work function of thin ITO layers has been intensively studied due to its importance in e.g. organic solar cells and OLEDs. Values in the respective literature ([62, 63, 64, 65, 66, 67]) range from 3.9 to 4.7 eV depending on previous treatments and cleaning of the layers. This is well above the photon energy of the ionization laser of 2.755 eV. Photoemission from the ITO coating should hence not occur in the experiment.

Furthermore, the ITO coating also serves as a broadband anti-reflective coating of the glass cell with a specified reflectivity of $R \leq 0.5\%$ over the whole relevant range from 450 nm to 850 nm. This increases the transmission of the cell for the single photons at 780 nm and reduces reflections of the ionization laser that might trigger dark counts in the charged particle detectors.

### 3.2.4. Epoxy glues for ultrahigh vacuum

Two different glues will be required for the assembly of the vacuum glass cell. First, an electrically conductive glue is needed to contact the ITO layer with cables. Second, a non-conductive glue is needed to attach the glass window to the open side of the glass cell [12].

Glues for ultrahigh vacuum applications have to fulfill two main requirements: They have to show low outgassing in order to allow for low pressures in the chamber and they have to be heat resistant in order to withstand the bakeout of the vacuum system (in our case the respective parts will be heated to about 130°C). Both requirements can be fulfilled by suitable epoxy adhesives. We chose the silver filled EPO-TEK® H20E from Epoxy Technology for the electrical contacts and EPO-TEK® 353ND for gluing the windows. Both are two-component adhesives that have to be cured at at least 80°C. After mixing of the components both adhesives must first be degassed

[11] In a rectangularly shaped layer the electric resistance for a current flowing between two opposing faces is proportional to the lenght of the rectangle but inversely proportional to its width. The resistance is therefore the same for any square (sq), independent of its side length. Hence the unit [kOhm/sq].

[12] Gluing of an ultrahigh vacuum glass cell and UHV-suitable electrical contacting of components has been done by Pascal Böhi in the group of Philipp Treutlein at LMU Munich in the context of an experiment with a Bose-Einstein condensate on an atom chip [68]. We gratefully acknowledge advice from the group on the selection and handling of the glues.

| | H20E | 353ND |
|---|---|---|
| electrical volume resistivity | $\leq 0.0004\ \Omega\,\mathrm{cm}$ | $\infty$ |
| pot lifetime | $\leq$ 2.5 days | $\leq$ 3 hours |
| curing temperature | 2 hours at 100°C | 10 minutes at 100°C |
| max. continuous operating temperature | 200°C | 250°C |
| glass transition temperature: $T_G$ | $\geq$ 80°C | $\geq$ 90°C |
| coeff. of thermal expansion:<br>below $T_G$<br>above $T_G$ | <br>$31 \cdot 10^{-6} \frac{1}{°C}$<br>$158 \cdot 10^{-6} \frac{1}{°C}$ | <br>$54 \cdot 10^{-6} \frac{1}{°C}$<br>$206 \cdot 10^{-6} \frac{1}{°C}$ |

Table 3.3.: Key characteristics of the epoxy glues used for the glass cell. H20E is used for electrical contacting the ITO-layers. 353ND is used for gluing the glass window onto the cell.

in a vacuum chamber at $\leq 10^{-2}$ mbar for several minutes to allow for low outgassing in the future vacuum setup. Table 3.3 gives an overview over the relevant characteristics of the glues.

After curing the adhesives are heat resistant to up to 200°C. However, the coefficients of thermal expansion are about two orders of magnitude above that of the cell material ($5.1 \cdot 10^{-7} \frac{1}{°C}$ for Heraeus Suprasil) - below as well as above the glass transition temperature $T_G$. This poses the risk of mechanical stress along the glue joint. The ramping of the temperature during the bakeout should therefore happen slowly in order to make use of the glass transition point as an opportunity to balance out the differing thermal expansions of glass and adhesive (figure 3.9).

### 3.2.5. Contacting of the coating

Before closing the cell with the separate glass window each of the coated surfaces is first electrically contacted with a cable. Apart from the two inner walls that are to be employed as electrodes also the outer surfaces are contacted. These are then connected to ground with the aim of reducing the accumulation of charged dust particles that could otherwise be attracted by a net bias of the electric potential in the detector setup (see section 4.1.4).

For the inner walls we use coaxial cables with the inner conductor and shielding made of silver strand and the insulation out of ultrahigh vacuum suitable polyamid[13]. At their ends the shielding is stripped off. The inner conductor is then cramped into silver coated cable shoes of copper together with parts of the inner insulator as a pull relief.

To provide an electrically conductive bond between the cable shoe and the ITO coating we use the silver filled epoxy glue EPO-TEK® H20E. Pilot tests were performed in order to study the electrical resistance between the cable and the layer in such a glued contact as well as its mechanical resistivity. Before gluing, the glass substrate as well as the cables where first cleaned in an ultrasonic bath with first ethanol and then acetone. The resistance from single contacts into the layer was determined by placing an additional contact at a very close distance so that the resistance within the coating was negligible. Simple dropping of the glue onto the layer

[13] Allectra, 311-KAPM-060-COAX

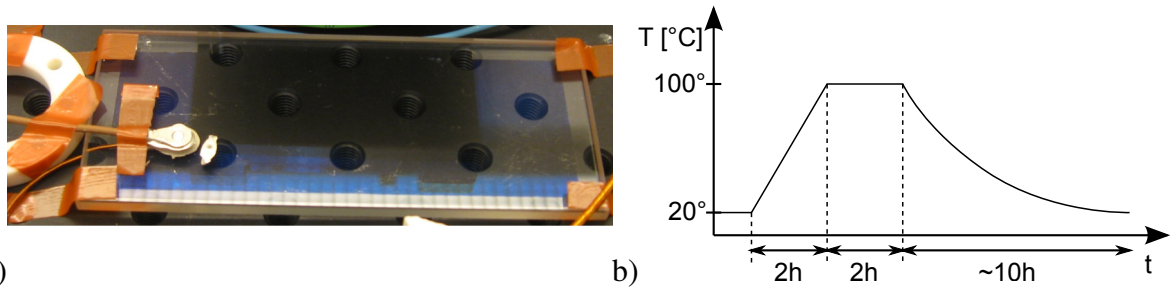


a) b)

Figure 3.9.: a) Electrical contacting of the ITO-layer on the glass window with the silver filled epoxy glue. An adjacent auxilliary contact is used to check the resistance from the glue into the layer. b) For the bakeout the temperature was linearly ramped to 100°C within two hours. After two hours at the maximum temperature the oven was switched off and slowly cooled down over a period of ~10 hours.

resulted in resistances in the range of 5-20 $\mathrm{M}\Omega$ or even above the measurement range of the used multimeter. However, it was found that rubbing the glue into the ITO layer with a metal tip and thereby cautiously scratching the layer yields much lower electrical resistances below 1 $\mathrm{k}\Omega$.

Concerning the mechanical stability it was observed that it is possible to rip the glued spot off the coated glass substrate with moderate effort. The coating is thereby partially removed from the glass substrate. Increasing the size of the bond evidently helps but still great care should be taken when handling the glued parts.

Figure 3.9a) exemplarily shows a photograph of the glued contacts on the ITO-coated glass window. One can easily distinguish the coated region from the uncoated margin along the edges by its blue color. The cable shoes were held in place during the bakeout by strips of heat resistive tape. A small spot of glue next to the contact is used after the bakeout to check the resistance from the contact into the layer. The bakeout of the glass window and the cell was performed in an oven with a preprogrammed temperature profile (figure 3.9b)). The temperature was ramped up and down slowly in order to minimize mechanical stress within the glass cell.

### 3.2.6. Gluing of the window

After contacting the coating, the open side of the glass cell has to be closed with the separate window. The bond is realized with the non-conductive EPO-TEK® 353ND.

For the assembly of the cell and the window a custom made holder keeps the glass cell in a horizontal position with the open side showing upwards. The glue is then applied on the rims of the cell's glass walls and the window is attached from the top. For the bakeout the same temperature curve as for the silver filled glue was used.

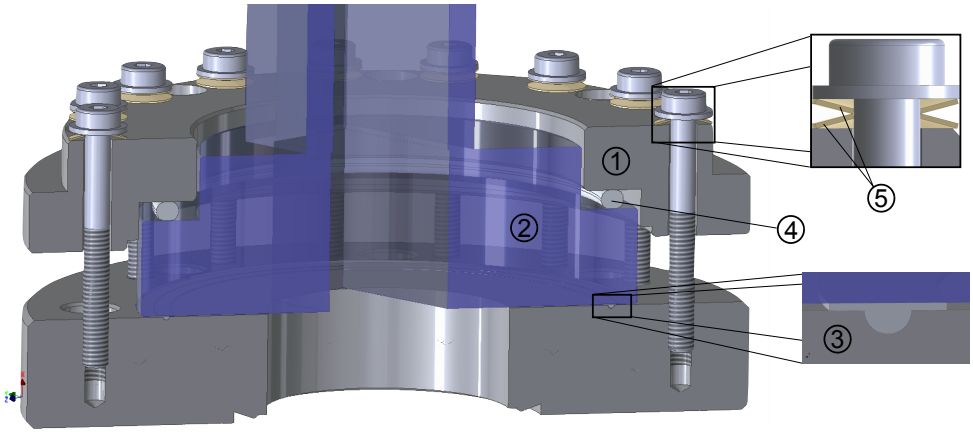


Figure 3.10.: Connection of the glass cell to the vacuum chamber: A collar flange (1) presses the glass flange (2) onto an indium wire (3) that is placed in a groove in the vacuum adapter flange. A compressible Helicoflex® seal ring (4) compensates unevenesses of the surfaces. Two disk springs (5) under the screw heads indicate the tightening force at each screw.

### 3.2.7. Connection to the vaccum chamber

The attachment of the glass cell to the vacuum system requires an ultrahigh vacuum suitable seal between the glass flange and a steel adapter flange on the vacuum setup. This seal is realized with an indium wire. Figure 3.10 shows a drawing of the metal-to-glass transition. A collar flange is used to press the glass flange onto the gasket. The indium wire (thickness 1 mm) is placed in a circular groove (diameter 70 mm) on the adapter flange's surface. The groove itself has a semicircular profile with a width equal to the wire's thickness and a depth of half its thickness [69]. An elastic Helicoflex® seal ring between the glass flange and the collar flange levels out potential unevenesses of their surfaces.

For closing the seal the adapter flange is connected to the vacuum pump of a helium leak detector. Initially 16 screws (M4) arranged around the circular groove are used to slightly compress the indium wire until a vacuum can be built up. Further compression of the wire then happens by atmospheric pressure alone (17.5 Newton per centimeter of wire). In the end approximately the same compressing force is added with the screws. By measuring the compression of disk springs[14] placed between the screw heads and the collar flange it is possible to monitor the applied force at each screw separately and thus to achieve a balanced fastening of the seal. The obtained helium leak rate is below the minimum detectable leak rate of $10^{-10}$ mbar·l/s. The compressing force necessary for obtaining a tight seal is of the same order of magnitude as reported in the literature (see e.g. [70] where 8.6 kg/cm are reported for a 1.6 mm thick wire on a polished ceramic flange).

The indium seal might undergo further compression during the bakeout of the vacuum setup where temperatures approach the melting point of indium (156.6 °C). During this period the disk

[14] Schnorr 027100, 8×4.2×0.3 mm, 34 Newton at 25% compression, 61 Newton at 50% compression

springs help to better maintain the load on the seal as compared to a setup with screws alone.

### 3.2.8. Measurement of birefringence

Before the assembly of the glass cell the birefringence of the large sidewalls was analyzed by measuring the extinction ratio of a $H$- and $+45^{\circ}$-polarized laser beam (wavelength 780 nm) at a $V$- and $-45^{\circ}$-oriented polarizer after transmission through the respective substrate[15]. In both cases the extinction was on the order of the sensitivity of the used pair of polarizers ($< 1/10000$). After the assembly the glass cell was attached to the vacuum system and we measured the extinction ratio of the evacuated glass cell - now after transmission of the light through both walls. For both, $H/V$- as well as $+45^{\circ}/-45^{\circ}$, it was around $\approx 1/5000$. In principle the birefringence can also be measured individually for each of the walls by placing one polarizer inside of the cell. This possibility was, however, abandoned due to the fragility of the gluing spots for the contacting of the coating. But in a setup with a comparable glass cell no difference in the extinction ratio for an evacuated and an unevacuated cell has been observed (see appendix D.2). Hence it is supposed that the measured birefringence originates only from stress induced due to the gluing of the components.

The obtained value indicates a much lower birefringence as compared to the previously used cells where the extinction ratio for $+45^{\circ}/-45^{\circ}$ polarization after transmission through both walls was about $1/50$.

In the meantime a more sophisticated design for an ultra-low birefringence vacuum glass cell of dodecagonal shape has been presented [71] that allows extinction ratios below $10^{-6}$. Measurements in this setup confirm our observations that the birefringence is not considerably affected by the evacuation of the cell. The publication also recommends the use of an epoxy glue containing filling particles (Epotek® H77) that leads to less stress induced birefringence after the bakeout of the glue. This could also contribute to a lower birefringence in the system presented in this thesis. Moreover, the same group also demonstrated a highly precise method to characterize the birefringence of each cell wall separately after evacuation by measuring the differential vector light shift of an atomic hyperfine transition of atoms trapped within the cell [72].

[15] $H$- and $V$- polarization denote the polarization along the x- and y-axis.

## 3.3. Temperature stabilization of the trap setup

### 3.3.1. Effects of temperature instabilities

With the repetition rate of the current setup a test of Bell's inequality and other experiments characterizing the entangled atom-atom state require long measurement times over periods of up to a week or more. In order to guarantee constant conditions during these experiments an active and precise stabilization of the temperature within the trap setups has turned out to be indispensable. This arises mainly from the observation that the coherence properties of the atomic qubit state, i.e. the superposition of the $F = 1, m_F = \pm 1$ ground states, are strongly affected by temperature drifts of technical components in the setup. The coherence of the atomic state is generally characterized by observing the evolution that the atomic state performs in the presence of perturbations that can vary over many realizations of the same experiment. In the case of atomic qubits encoded in Zeeman states such time-varying perturbations arise from drifting external magnetic fields or - when using optical dipole traps - from the Zeeman state dependence of the trapping potential due to a partially circular polarization of the trapping laser (see 2.2.2). The impact of the trap on the atomic state is then equivalent to that of a magnetic field along the $z$-axis. This latter effect can for example vary due to drifting birefringent components in the trapping laser's beam path. In both cases the result is a Larmor precession of the atomic state and a variation of this behaviour between different runs of the experiment.

Details on how measurements of the Larmor precession are performed in our specific experiment can be found in [40]. In order to determine the influence of temperature drifts on the long-term coherence of the atomic state we performed continuous measurements of the period of the Larmor precession over the course of two days and compared it to the evolution of the temperature in the laboratory. Figure 3.11 shows the result of this measurement. The temperature (green curve) performed a oscillation with a peak-to-peak amplitude of about 0.7 °C between day and night. As one can see, the Larmor period (red curve) is strongly correlated with the temperature.

Further analysis revealed that the main origin of the drifting atomic coherence times is a temporal drift of the residual circular polarization component of the dipole trap laser. The a-priori linearly polarized trap laser is transmitted through several optical components such as dichroic mirrors, the microscope objective and the vacuum glass cell (see figure 3.3) that can show stress induced - and hence temperature dependent - birefringence and render its polarization elliptic. Figure 3.12 exemplarily shows the temperature dependent polarization drift caused by transmission through the dichroic mirror in the setup of "atom 2". It has been obtained from a measurement of the extinction ratio of the originally $H$-polarized trap laser at a $V$-polarized polarizer behind the mirror. The birefringence of the other components was generally found to be smaller but also here temporal drifts of the induced circular field components of the trap laser could be observed.

In the worst case scenario the drift of the extinction ratio is entirely a result of an acquisition of circular polarization components. In the following we calculate the resulting energy shift $\Delta E$ of the Zeeman states $S_{1/2}, F = 1, m_F = \pm 1$ in the center of the trap ($r = 0, z = 0$) where the intensity is the highest. According to equation 2.1 the relative energy shift with respect to the

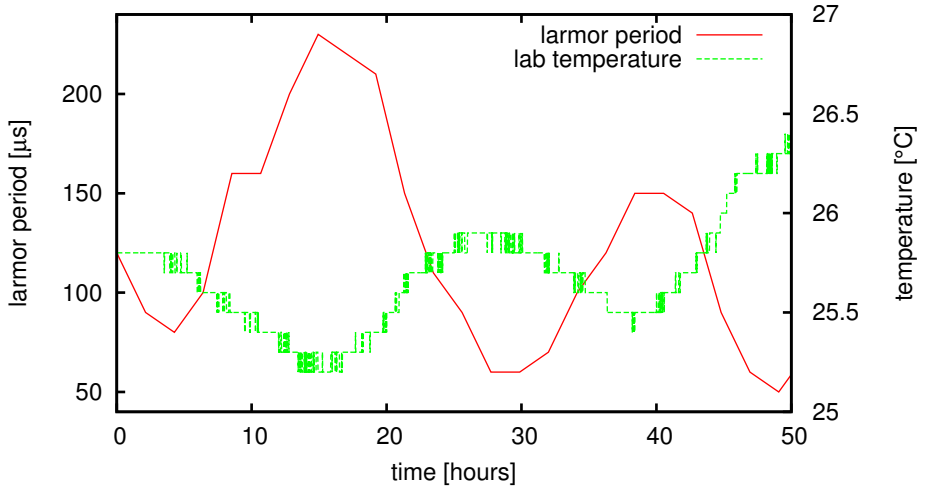


Figure 3.11.: Correlation between the temporal evolution of the temperature in the laboratory (*green curve*) and the coherence of the atomic state as measured by the duration of its Larmor precession (*red curve*). The Larmor period is correlated with the daily variations of the lab temperature.

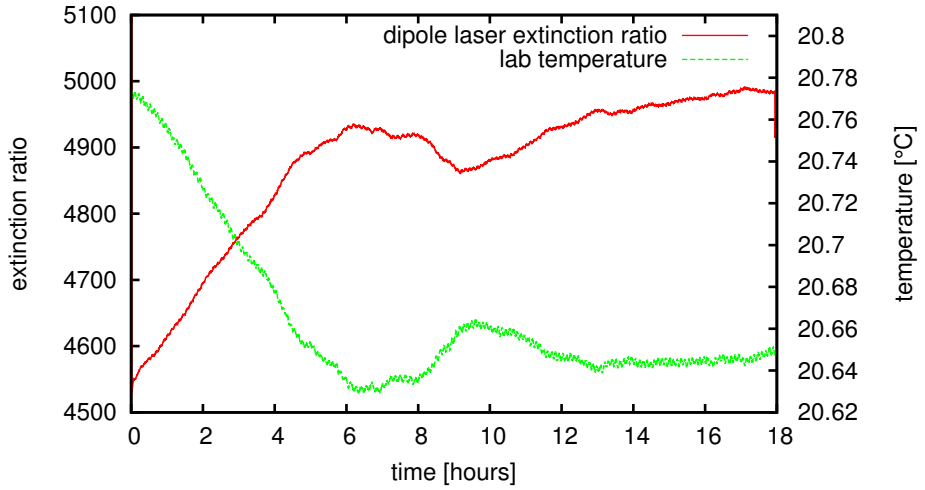


Figure 3.12.: Temperature-dependent drift of the circular polarization component of the dipole trap laser after transmission through the dichroic mirror in the confocal microscope. *Green curve*: temperature measured at the ion getter pump. *Red curve*: extinction ratio of the trap laser at a polarizer behind the mirror.

$m_F = 0$ Zeeman level is:

$$\Delta E = \frac{\pi c^2 \Gamma}{2\omega_0^3} \left( \frac{g_F m_F \sqrt{1-\epsilon^2}}{\Delta_{2,F}} - \frac{g_F m_F \sqrt{1-\epsilon^2}}{\Delta_{1,F}} \right) \cdot I(0,0) \tag{3.1}$$

The ellipticity is generally determined by rotating a polarizer in the laser beam and recording the maximum and minimum transmitted power. It is then calculated from $\epsilon = \frac{P_{max}-P_{min}}{P_{max}+P_{min}}$ [36]. On the other hand the ellipticity can also be expressed in terms of the extinction ratio $ER = \frac{P_{min}}{P_{max}+P_{min}}$ via $\epsilon = 1 - 2 \cdot ER$. For the minimum and maximum extinction ratios of $\frac{1}{4600}$ and $\frac{1}{5000}$ from figure 3.12 the energy shifts are

$$\begin{aligned} \Delta E \left( \frac{1}{4550} \right) &= h \cdot 30.0\,\mathrm{kHz} \\ \Delta E \left( \frac{1}{5000} \right) &= h \cdot 28.6\,\mathrm{kHz}. \end{aligned}$$

These energy shifts correspond to effective magnetic fields $B_{eff} = \Delta E/(\mu_B\, g_F\, m_F)$ of

$$\begin{aligned} B_{eff} \left( \frac{1}{4550} \right) &= 42.8\,\mathrm{mG} \\ B_{eff} \left( \frac{1}{5000} \right) &= 40.9\,\mathrm{mG}. \end{aligned}$$

In general a constant effective field along $z$ can be canceled by applying a real $\vec{B}$-field in the opposite direction. However, already the drift of this effective field by ~2 mG is about four times larger than what is tolerable in a Bell-experiment[16]. A stabilization of the setup's temperature hence is indispensable. Moreover, also the readout laser's polarization or magnetic fields from nearby sources like the ion-getter pump might be temperature dependent. In addition stable temperatures also reduce geometric drifts of all laser beams thus reducing the required maintenance of the entire trap setup.

### 3.3.2. General strategy

The multitude of possible sources of error gives motivation to develop a temperature stabilization of the whole trap setup and not just for specific components. Based on the above results it is estimated that the peak-to-peak amplitude of the residual temperature drifts of critical components should be below 0.04 °C. This stability should be maintained in presence of the usual time-varying thermal load within the laboratory. As a starting point a high-performance air conditioning unit was installed in the laboratories. Moreover, the windows where isolated with

[16] Due to the large inter-atomic distance in a Bell-experiment the waiting time between the creation of atom-photon entanglement and the atomic state readout is ~13 µs. For a field along $z$ superpositions like $|\Psi\rangle = \frac{1}{\sqrt{2}}(|1,+1\rangle + |1,-1\rangle)$ for example show temporal evolutions of the kind $|\langle\Psi(t=0)|\Psi(t)\rangle|^2 = \cos^2 \omega_L t$ with $\omega_L = \mu_B g_F B_{eff}/\hbar$. In order to keep the overlap of these states with their initial configuration above 99.9%, a magnetic field stability better than $\cos^{-1}\left(\sqrt{0.999}\right) / (13\,\mu\mathrm{s} \cdot 0.7\,\mathrm{MHz/G}) \approx 0.5\,\mathrm{mG}$ is required.

styrofoam to reduce influences from outside temperature variations and solar irradiation. By these means the temperature stability in the lab could be improved to below $\pm 0.2\,°\mathrm{C}$. The strategy is now to implement a secondary temperature control stage that further stabilizes only the trap setup within the housing of the trap's optical table. More precisely, the idea is to stabilize the air temperature within the housing in a closed control loop using a heatsink and air fans that provide a constant heat exchange between the sink and the entire setup.

### 3.3.3. Dimensioning of the temperature stabilization system

To keep the necessary power and size of the stabilization system small, the interior of the trap's housing should be thermally isolated from the outside laboratory. To this end air exchange between inside and outside as well as heat transmission through the housing's walls should be minimized. We therefore close all openings and feedthroughs of the housing up to a few cm² and add a layer of 1 cm thick styrofoam to the housing's side walls and 4 cm thick styrofoam to the bottom plate. The thermal transmittance $U_{th}$ of the housing averaged over its entire surface of 10 m² then is estimated to be:

$$U_{th} = 1.4\,\frac{\mathrm{W}}{\mathrm{m}^2 \cdot \mathrm{K}}$$

If the temperature of the outside laboratory drifts by 1°K around its mean value and the set temperature of the temperature stabilization is set close to that mean value, then the maximum transmitted heat across the housing's walls becomes:

$$P_{th} = U \cdot 10\,\mathrm{m}^2 \cdot 1\,°\mathrm{K} = 14\,\mathrm{W}$$

Although the actual temperature stability in the lab is much better, we take this to be the minimum cooling and heating power that the stabilization should be able to deliver. Additional considerable sources of heat within the trap setup are the magnetic field coils of the MOT that dissipate about 6 ... 7 Watts (however only during the short loading periods of the trap) as well as the electric components of the temperature stabilization itself.

Apart from the pure heat power of the temperature stabilization one also requires a sufficiently strong air circulation between its heatsink and the walls of the housing as well as the setup's components. This is necessary in order to be able to react quickly on variations of the thermal load and reduce temperature gradients within the setup. Thus the airflow rate of the employed fans should allow to circulate the air volume in the housing (about 2 m³) at least two to three times per minute which results in average flow velocities across the cross section of the setup (1 m²) of 6.6 ... 10 cm/s.

### 3.3.4. Technical implementation

The envisioned temperature stability shall be realized using an analog closed feedback control loop in which the heating or cooling power of the heatsink is continuously adjusted such that the air temperature at an experimentally sensitive spot is kept at a predefined set value.

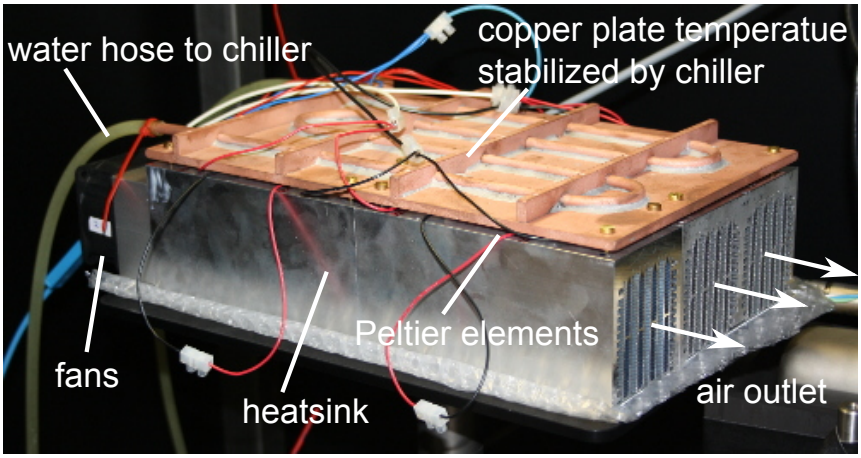


Figure 3.13.: Photograph of the temperature stabilization for the trap setup. Fans let the air within the trap setup circulate through a heatsink of which the temperature - and thus the heating or cooling power - is controlled by Peltier elements. These pump heat from the sink into a copper plate of which the temperature is stabilized by a water circuit.

The photograph in figure 3.13 shows the aluminum heatsink with the attached air fans. The sink incorporates three fans each attached to one of three air channels in the sink[17]. The entire sink has a length of 300 mm and a cross section of 187 mm×74 mm. With the given flow rate of each fan[18] of 54 m³/s the specified heating/cooling power of the entire sink is about 30 W per Kelvin temperature difference between the sink and the air. The total electric power of the fans that is dissipated into the trap setup is $3 \times 2.9\,\mathrm{W} = 8.7\,\mathrm{W}$.

The temperature of this heatsink (and hence its power) is controlled by ten Peltier elements[19] that are evenly distributed over the heatsink. They pump heat from the sink into a copper plate or vice versa. The copper plate in turn dissipates the heat into a water circuit which is connected to a chiller[20] that is placed outside of the trap setup and which stabilizes the water temperature to a precision of $\pm 0.16\,°\mathrm{C}$. The electric current through the Peltiers is adjusted by a commercial temperature controller with a PID regulator[21]. With this system a total heat transfer capacity of about 65 Watts can be achieved from the heatsink into the copper plate. The input signal for the regulator is provided by a temperature sensor[22] that measures the air temperature at a chosen position. This control loop allows for a continuously variable (and in principle infinitely precise control) of the temperature.

The position of the temperature stabilization within the trap setup can be seen in figure 3.1. In both trap setups it is placed at half height of the housing and oriented such that the air flow traverses the entire setup lengthwise. The thermoelectric element for the control-loop should be

[17] Two of the channels including the fans: fischerelektronik LA V 7 300 12. Third channel: LA V 6 300 12.
[18] ebmpapst 612 NHH-118
[19] TES1-127025 - 30X30, P&N Technology
[20] Melcor / Laird Technologies MRC150DH2-HT-DV, cooling capacity: 150 W, heating capacity: 125W
[21] Thorlabs TED350, maximum output ratings: 5 A, 40 W
[22] NTC 10 kOhm

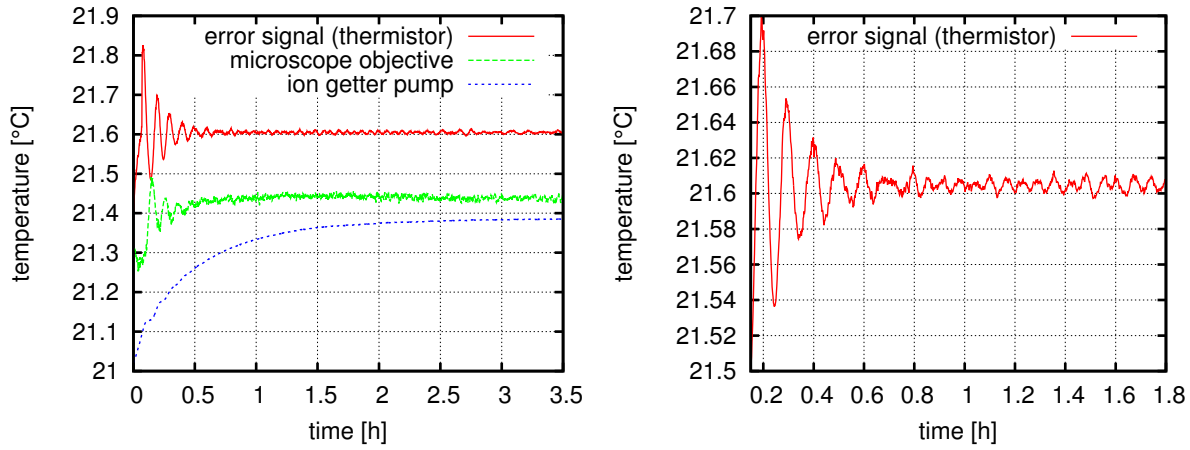


Figure 3.14.: Typical settling behavior of the temperature of the trap setup after an initial deflection from thermal equilibrium (here: "atom 2"). The air temperature at the thermistor (error signal) settles to a final residual peak-to-peak oscillation of 0.01 K after about 40 minutes. Other more massive components reach their equilibrium temperature after three hours. The right figure shows a zoom into the error signal from the left.

placed close to the optical component that requires the highest temperature stability. In case of "atom 2" this is for example the dichroic mirror in the confocal microscope.

### 3.3.5. Operation and characterization

Figure 3.14 shows the typical settling behavior of the system as is occurs when the stabilization is switched on or when the setup returns to its thermal equilibrium state after the housing of the experiment has been open for a longer time (at least 10 minutes). We monitor the temperature evolution at three spots within the trap setup of "atom 2": The air temperature at the thermistor close to the dichroic mirror via the error signal of the PID controller, the surface temperature of the microscope objective and that of the ion getter pump. In the beginning the air temperature oscillates with a period of about 6 minutes with a peak-to-peak amplitude of 0.4 K. Within fourty minutes this amplitude exponentially decreases to a residual inaccuracy of 0.01 K peak-to-peak. The temperature of the nearby microscope objective (measured with a sensor that is glued onto the surface of the objective) follows these oscillations due to its low thermal mass and approaches a stable value after one hour. In contrast the ion getter pump shows a more inert behaviour due to its large mass and reaches a stable temperature only after three hours. The initial oscillations with the period of 6 minutes appear for a rather wide range of P-, I- and D-values and seem to be more a result of the slow response of the temperature at the thermistor to variations of the Peltier current.

Once the temperature in the setup has reached a stable configuration the Peltiers typically draw an electric power that corresponds to a heat pump power of about 20 W that is transfered into the

copper plate. Including the heat dissipation of the Peltiers themselves (~7 Watts), this is in good agreement with the above listing of sources of heat.

In the following we characterize the long-term stability of the system and its residual susceptibility to drifts of the external lab temperature. As an example we analyze the temperature evolution in the two trap setups that was recorded during an eighty hours long Bell-experiment with a time resolution of 5 minutes (see figure 3.15). It can be seen that the error signal from the thermistor of the control loop remains fully unaffected by drifts of the lab temperature[23]. Critical components close to the sensor are hence well stabilized. Other components such as the microscope objective and the ion getter pump still experience drifts that follow the outside temperature. However, the amplitude of these drifts is attenuated by a factor of 5 ... 20 depending on the position of the respective element and the specific geometry of the differing trap setups.

Further improvement of the stability of components beyond the vicinity of the thermistor could easily be achieved by optimizing the isolation of the housing or by increasing the air flow. The latter would also help to accelerate the settling of the temperature of massive components after a longer opening of the housing due to a higher heat exchange rate between the air and the setup.

## 3.4. Summary

The single atom trap basically consists of a confocal microscope, that focuses the laser beam of the optical dipole trap and allows to monitor the presence of the atom via collection the emitted fluorescence photons. The Gaussian waist $w_0$ of the trap laser is 1.92 µm. The numerical aperture for collecting the fluorescence is 0.267. The readout laser has been set up on the opposite side of the atom trap. For both, the collection optics as well as the readout laser, angle errors in the alignment of the beam axes with respect to the quantization axis are below 1°. Also polarization errors of the readout laser are at this level. This is important for the quality of the prepared atom-photon state and the atomic state readout. To perform fast and precise switching of the measurement bases in a loophole-free Bell experiment the power of the readout laser can be switched between two arms with the appropriate polarization within 185 ns.

This chapter also introduced the design and assembly of a new ultrahigh-vacuum glass cell. It is optimized for low stress-induced birefringence. For light that is transmitted through the cell the extinction ratio at crossed polarizers was 1/5000 in two complementary bases. Moreover, it is equipped with an electrically conductive optical coating of indium tin oxide that allows for tuning of the electric field configuration of the charged particle detector setup.

In order to avoid drifts of the birefringence of optical components that induce partial circular polarization of the trapping laser, a precise long-term stabilization of the temperature of the trap setups was found to be mandatory. These drifts degrade the coherence properties of the atomic state as they shift the eigenenergies of the Zeeman states in the same manner as an effective magnetic field along the $z$-direction would do. To this end a system that stabilizes the

[23] The lab temperature was measured on the optical table of the laser system that is not shielded by a housing. Short term drifts of the air temperature due to switching cycles of the air conditioning are strongly damped due to the high thermal load of the table. We consider the larger residual fluctuations of the lab temperature in trap 1 to be responsible for the lower stability inside the trap setup.

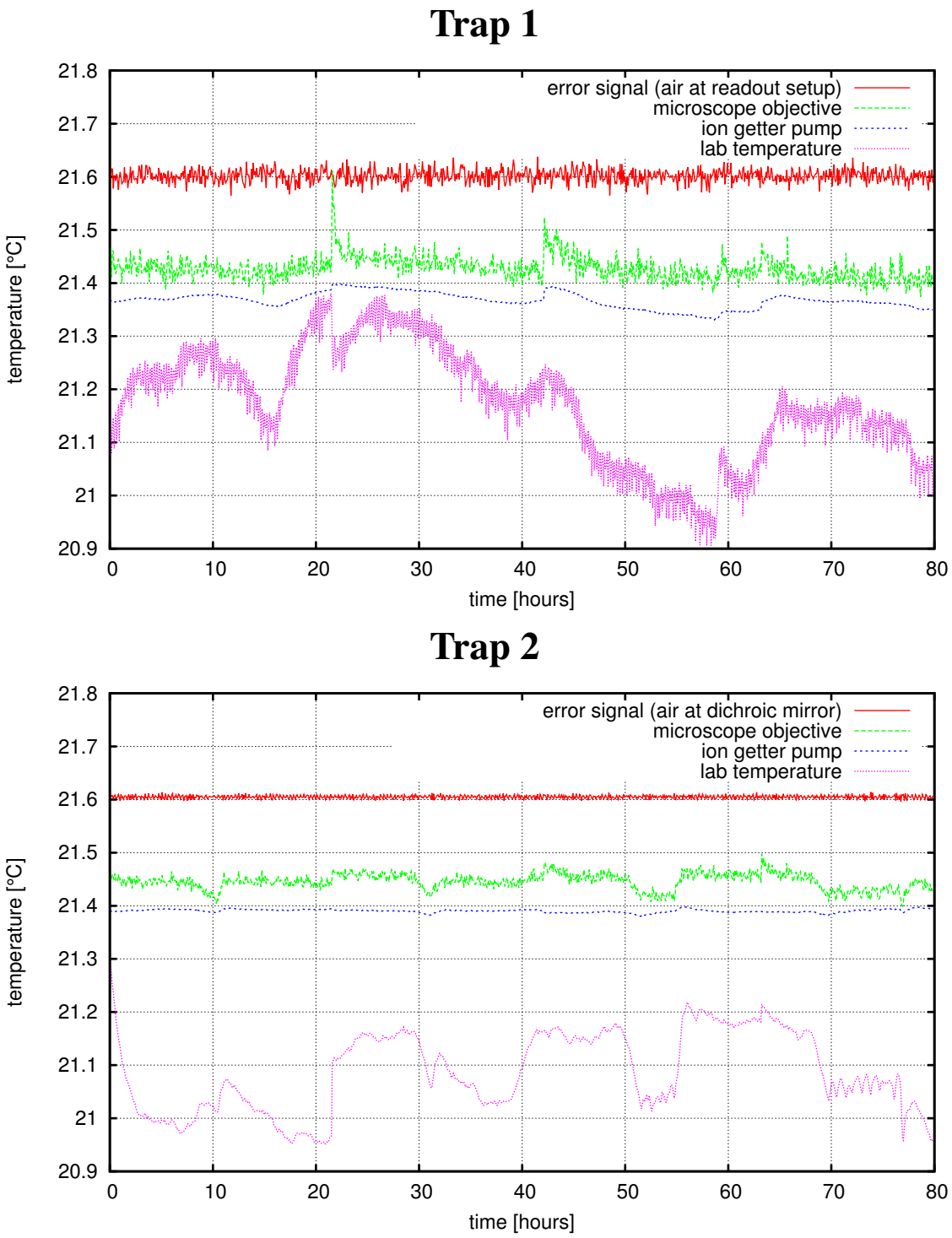


Figure 3.15.: Temperature stability of the two trap setups during an 80 hours long Bell experiment. The air temperature at the position of the control loop's thermistor (error signal) is not affected by drifts of the lab temperature. More remote components show a residual dependency on the outside temperature. The pronounced peaks visible in the green curve for trap 1 arose during maintenance breaks where the housing was opened.

air temperature within the setup has been implemented. It guarantees that peak-to-peak drifts of the temperature at the spot of the temperature sensor remain below 0.01 K while also the drift at more remote components is kept well below 0.1 K. This stability allows to reduce the drifts of the effective magnetic field to better than 0.5 mG and was verified over the duration of an 80 hours long Bell-experiment.

# 4. Detection of the ionization fragments

For the envisaged application of the atomic state readout in a loophole-free Bell experiment the employed detectors for the ionization fragments need to be fast (this mainly requires short times of flight of the particles to the detectors) and need to have high detection efficiencies. The presented work is based on a detector setup developed by Florian Henkel [28, 73]. In brief the setup consists of two opposing channel electron multipliers (CEMs) that are installed within the ultrahigh vacuum setup close to the position of the single atom trap. An applied electric field between the detectors separates the ionization fragments i.e. the ion and the electron and accelerates each of the particles to one of the detectors where the impact creates an electron avalanche that produces a measurable electric pulse at the output of the detectors.

This chapter describes the basic functionality and characteristics of the channel electron multiplier setup. The key figure of merit are the efficiencies with which the ionization fragments can be detected. These efficiencies strongly depend on the position between the detectors where the ionization fragments are created. Here a method is presented that allows to modifiy the configuration of the accelerating electric field such that the detection efficiencies can be optimized for the fragments originating from the single atom trap.

## 4.1. Setup and characteristics of the charged particle detectors

### 4.1.1. Channel-electron multipliers (CEM)

In the presented setup we use channel electron multipliers (CEMs) as detectors for the ionization fragments. These types of CEMs are suitable for the detection of electrons as well as any other charged particles. The employed CEMs (type KBL 10RS/45 by Dr. Sjuts Optotechnik GmbH) have a multiplier channel of lead glass in the form of a sinuous line within a ceramic body. The channel has a conical entrance with a diameter of 12 mm. Upon impact of a primary particle on the channel's entrance secondary electrons are emitted. The latter are further accelerated into the channel by a gain voltage $U_{gain}$ applied between the front entrance and the exit of the channel and thus create additional electrons upon impact on the channel's surface. At the exit of the channel the resulting electron avalanche consists of about $10^8$ particles - strongly depending on the applied gain voltage. It is collected by an anode made of stainless steel. The channel is electrically contacted with gold or silver contacts to which cables can be connected with screws

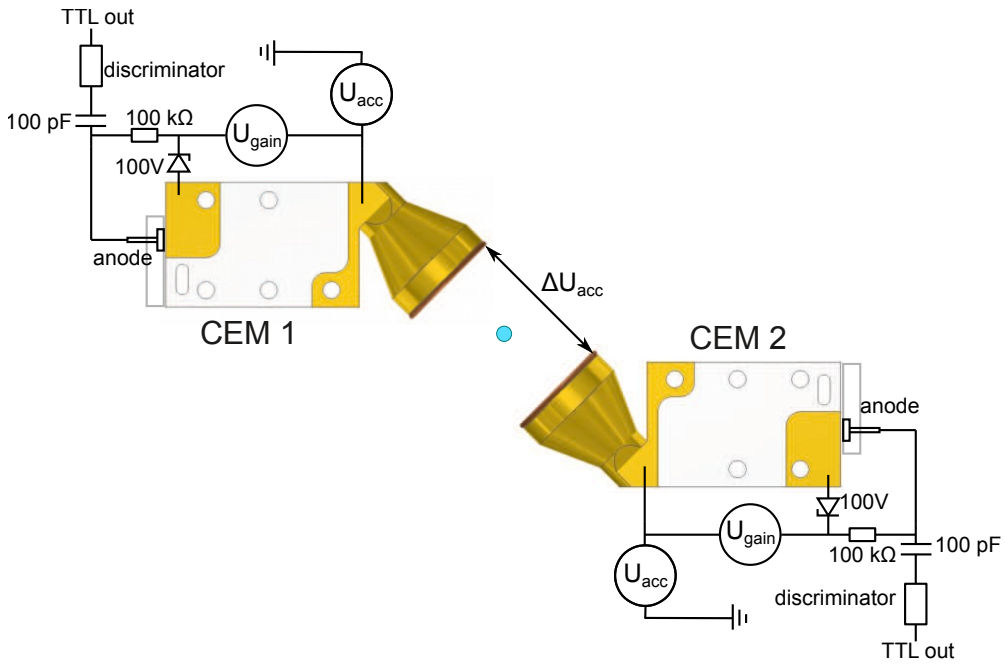


Figure 4.1.: Circuitry of the channel electron multiplier setup: The potential difference $\Delta U_{acc}$ separates the ionization fragments and accelerates them towards the detectors. Here a gain voltage $U_{gain}$ amplifies the produced secondary electrons to form an avalanche. The pulse from the electron avalanche is collected at an anode at the output of the CEM's channel. It is first decoupled from the DC high voltage and then registered by a discriminator.

through the ceramic body. All materials are ultra-high vacuum suitable and the detectors are specified to be bakeable up to 250 °C under vacuum conditions.

### Circuitry and output signals

Figure 4.1 shows a sketch of the circuitry of the CEM setup. A difference $\Delta U_{acc}$ in the electric potentials $U_{acc}$ at the front entrances of the CEMs separates the ion and the electron and accelerates the particles towards their respective detectors. The voltages $U_{acc}$ are set with respect to ground by two DC high voltage power supplies[1]. Typically $\Delta U_{acc}$ is in the rage of ~4 kV. The gain voltages at each CEM of 2-3 kV are produced by floating voltage supplies[2] whose negative poles are connected to the acceleration potentials $U_{acc}$ at the detectors' front sides. Zener diodes generate a potential difference of 100 V between the exits of the multiplier channels and their anodes so that the electron cloud is efficiently transferred to the anode.

In order to decouple the electric pulse generated at the anode from the DC high voltage, the anode is connected to a high voltage suitable capacitor with a capacity of $C = 100$ pF. Together

[1] FuG, HCP 14-12500, with overcurrent protection
[2] FuG, HCP 5-5000-MOD, with overcurrent protection

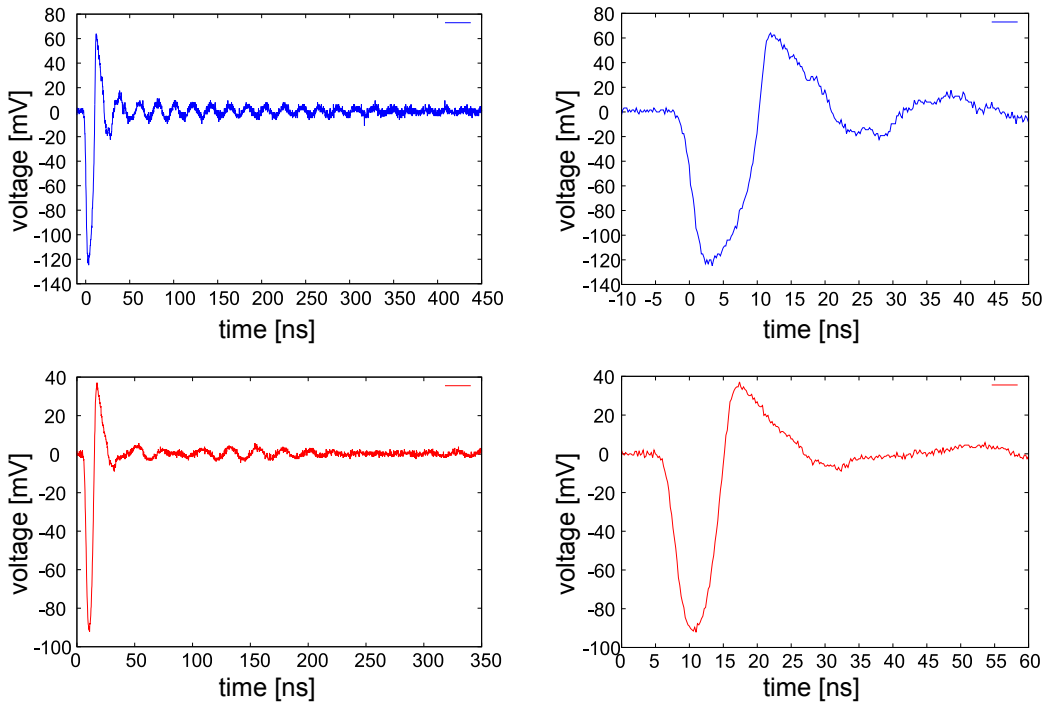


Figure 4.2.: Typical output signals of the channel electron multipliers upon detection of an electron (blue) and ion (red) measured at a 50 Ohm terminating resistance [74].

with the 50 Ω input resistance of the following discriminator[3] it serves as a high pass filter with a cut-off frequency of 32 MHz. Measured at the input of the discriminator the resulting negative pulse has a height of about -100 mV and a duration of about 10 ns (see figure 4.2). We set the threshold of the discriminator to -12 mV. At its output the discriminator delivers a TTL-pulse for further digital signal processing and registration of the detection events. The dead time of the discriminators is 80 ns.

The entire circuitry is placed outside of the vacuum setup. It is fully symmetric which means that both of the CEMs can be used to detect either the electron or the ion. Their role is solely defined by the sign of the relative voltage difference $\Delta U_{acc}$ between the two acceleration voltages.

The intrinsic dark count rate of the channel electron multipliers is specified to be below 0.02 $\frac{\#}{s}$, limited by events triggered by cosmic background radiation. However, in this specific setup and experiment the actual dark count rate is much higher. Section 4.1.3 gives a summary of the different sources of dark counts and possible countermeasures.

### Aging of the detectors

The actual gain voltage that is necessary for sufficient detection efficiencies strongly depends on the wear level of the detectors that is given by the overall accumulated counts. The detectors are specified for a constant count rate of 200000 $\frac{\#}{s}$ for a duration of the order of several years. In

[3] PAD-01A by WMT-Elektronik GmbH

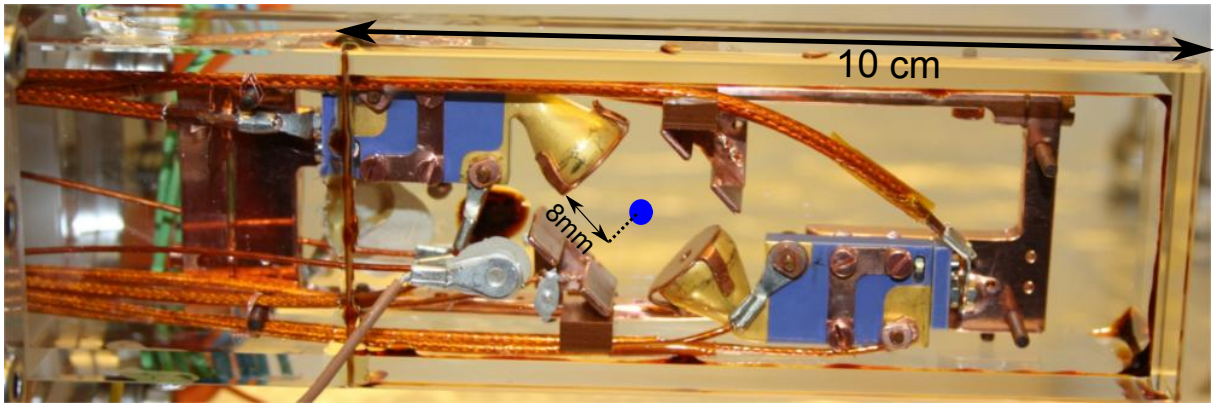


Figure 4.3.: The CEM setup inside the ultrahigh vacuum glass cell. The CEMs are mounted on a copper frame that is carefully centered within the cell by Kapton screws and are contacted with Kapton-insulated high voltage cables. The entrance of the CEMs is covered with a copper aperture with a 2 mm hole in the center. Copper electrodes and the ITO coated side walls of the cell allow tuning of the accelerating electric potential in transverse direction. A high optical access to the trapping region in the center is provided from all directions.

this experiment the count rate will not exceed 1000 $\frac{\#}{s}$ during the characterization of the detectors (chapter 4.3) and be on the order of 1 $\frac{\#}{s}$ or less during experiments on the readout of single trapped atoms. A priori no aging of the detectors should therefore be observed. However, due to the compactness of the present setup, high voltage differences between closely lying components can produce sporadic flashovers. These lead to massive emission of charged particles and excessive count rates at the detectors. In such cases the overcurrent protection of the high voltage power supplies switches off the detectors. Still, such events may deteriorate the active surface of the multiplier channel, reduce its gain and thus the detection efficiency of the detector. To a certain extent this effect can be compensated by higher gain voltages.

### 4.1.2. Setup in vacuum chamber

Figure 4.3 shows the entire detector setup installed in the vacuum glass cell. The two opposing channel electron multipliers are placed symmetrically around the position of the single atom trap at a distance of 8 mm from the trap. This is the minimum distance required for preserving the optical access to the trap from all directions. For this distance an acceleration voltage between the two CEMs on the order of 4 kV will be needed to keep the flight time of the heavier Rubidium ion below the envisaged 400 ns and also to achieve sufficient emission of secondary electrons upon particle impact (for a detailed calculation of the times of flight and the dependence of the detection efficiencies on $U_{acc}$ see [28] and [73]).

Apertures of copper with a centered hole of 2 mm on the front entrance of the detectors guarantee an almost homogeneous field configuration between the CEMs and provide additional shielding from stray particles and light, thus reducing dark counts. The diameter of these apertures

limits the volume out of which particles can be collected to a cylinder around the axis between the CEMs with at most the same diameter. This will be seen in the measurements in section 4.3.

The detectors are mounted on a frame fabricated of copper and are contacted with silver protected copper cable shoes and ultrahigh-vacuum compatible coaxial high voltage cables[4]. Especially in the vicinity of the CEM contacts the copper frame has been carefully polished in order to reduce the probability of flashovers between components at different electrical potential (see photos in appendix E).

### Tuning of the transverse field configuration

The frame also holds two opposing electrically contacted copper plates mounted on an axis orthogonal to the axis connecting the CEMs. The plates were originally designed to provide electric shielding of the potential in the central region from stray charges that accumulate on the top and bottom walls of the glass cell. Here the plates will also be used to control the potential between the CEMs in a transverse direction by applying voltage differences to those plates. Slits in the plates allow for optical access to the trapping region for laser beams that shall be scanned within the central plane between the CEMs' entrances (see section 4.3). In the same manner the electrically conductive coating on the two opposing large side walls of the glass cell can be used to induce a transverse shift of the potential along the optical axis of the confocal microscope. The voltages applied to the copper plates and the glass walls are in the range of at most a few hundred volts.

### Positioning within the vacuum cell

To avoid electrical contact of the copper frame and thereon installed components with the glass cell's side walls the position of the frame in the cell is centered with screws made of electrically insulating Kapton®. The minimum distance between the glass walls and the outermost points of the entrance cones of the CEMs is 1.5 mm resulting in potential gradients on the order of several kilovolt per millimeter. Smaller distances (and higher gradients) should be avoided to prevent flashovers.

### Short circuits due to coating with Rubidium

During the experiments the entire detector setup is exposed to the Rubidium vapor originating from the dispensers that are situated in the flange that connects the glass cell to the vacuum chamber. It is hence possible that a thin metallic and thus electrically conductive film of Rubdium is accumulated on the exposed surfaces of the setup. This occurred in one of the setups and caused short circuits between different high voltage contacts across the ceramic surface of the CEMs and also along the Kapton insulation of the high voltage cables.

Atoms originating from the dispensers get quickly adsorbed within a few collisions with surfaces. The Rubidium vapor inside the glass cell can hence be predominantly considered as a

[4] Allectra, 311-KAPM-060-COAX for high-voltage supply cables and the 50 Ohm version 311-KAP50 for CEM output signals

directed beam of atoms originating from the dispensers. Therefore an effective and simple measure against the described short circuits is to install shields between sensitive spots on the sides facing towards the dispensers. In the present setup this was accomplished by sheets of copper or Kapton foil.

### 4.1.3. Sources of dark counts and countermeasures

The intrinsic dark count rate of the CEMs is negligibly low and will not pose a limitation to the fidelity of the atomic state readout. However, several other sources of dark counts exist in the present application that can lead to significant dark count rates at the detectors. In the following we discuss all known sources and present countermeasures that allow to minimize the resulting count rates to tolerable values.

During the state readout of single trapped atoms the time window for accepting detection events from the CEMs will have a duration on the order of 200 ns. To keep the probability $p_{dc}$ of detecting a dark count within this time window below $0.1\%$, the overall dark count rate should be below $\frac{0.1\%}{200\,\mathrm{ns}} = 5000\,\frac{\#}{sec}$.

#### Direct detection of photons

First of all the detectors are also sensitive to ultraviolet photons that have sufficient energy to produce secondary electrons directly in the active surface of the CEMs. It is thus mandatory to provide good shielding from daylight and fluorescent lamps. Also the UV-LED (wavelength 390 nm) that is used for loading of the magneto-optical trap produces a considerable amount of dark counts on the order of 1000 ... 10000 $\frac{\#}{sec}$. It is thus switched off, once a single atom has been loaded.

The remaining source of light with the highest photon energy is the ionization laser ($E_{ph} = 2.62\,\mathrm{eV}$ for 473 nm and $2.75\,\mathrm{eV}$ for 450 nm). Its photons could enter the CEMs after scattering on the sidewalls of the glass cell or retro-reflection on external optical components. To test whether its photon energy is sufficient to trigger the CEMs, a continuous-wave laser beam with a wavelength of 473 nm was directly shined into the CEM's entrance. No additional counts were observed. The same experiment was not repeated with a wavelength of 450 nm, as this laser was only purchased later, when the optical access to the detector setup was already strongly limited. However, the resulting count rate is still expected to be tolerably low.

#### Stray electrons created via the photo-effect

Another source of dark counts are stray electrons. These can on the one hand be produced by photoemission from surfaces within the vacuum chamber. The metallic copper and gold surfaces in the CEM setup as well as the indium tin oxide coating on the glass walls all have work functions well above the photon energy of the ionization laser[5] and can hence be excluded as sources of stray particles. However, all surfaces get coated with small amounts of Rubidium from the dispensers (see also section 4.1.2). The ionization energy of single Rubidium atoms in

[5] $\Phi_{\mathrm{copper}} = 4.53$–$5.10\,\mathrm{eV}$, $\Phi_{\mathrm{gold}} = 5.1$–$5.47\,\mathrm{eV}$ [75], $\Phi_{\mathrm{ITO}}$: see section 3.2.3

| | trap 1 | | trap 2 | |
|---|---|---|---|---|
| | dark count rate | $p_{dc}$ | dark count rate | $p_{dc}$ |
| ion CEM | $< 1 \frac{\#}{sec}$ | $2 \cdot 10^{-7}$ | $< 1 \frac{\#}{sec}$ | $2 \cdot 10^{-7}$ |
| electron CEM | $< 500 \frac{\#}{sec}$ | $0.01\%$ | $< 500 \frac{\#}{sec}$ | $0.01\%$ |

Table 4.1.: Dark count rates of the channel electron multipliers in both trap setups and the associated probabilities $p_{dc}$ to detect a dark count within a 200 ns time window.

free space is $E_{ion} = 4.18\,\text{eV}$ [30] and thus also above the photon energy of the ionization lasers. But for a layer of Rubidium atoms it is expected that the necessary photon energy approaches the work function of bulk Rubidium metal which is $\Phi = 2.261\,\text{eV}$ [75]. In this case photo-emission would become possible.

As a countermeasure against such stray electrons the potential at both CEM entrances is chosen to be repulsive for electrons coming from the surrounding environment. This means that the applied potential must be negative with respect to the ITO coated glass walls and the copper electrodes. This countermeasure can, however, not help to shield against electrons that are created from Rubidium atoms on the surface of the CEM entrances themselves. Indeed, in the setup of trap 2 considerable dark count rates were induced by the ionization laser at 450 nm that increased with the time the dispensers were switched on. This happened on the time scale of a few days and resulted in a probability $p_{dc}$ to detect a dark count within the 200 ns time window of up to 7.4% (see appendix F). $p_{dc}$ could in turn also be decreased to several percent by cleaning the surfaces from the adsorbed Rubidium layer via light induced disorption using a UV lamp. To entirely circumvent this problem the laser was finally replaced by a laser at 473 nm, which has a slightly lower photon energy. Together with regular UV-cleaning of the setup this resulted in sufficiently low values of $p_{dc}$. The 450 nm laser was then installed in the setup of trap 1, where such dark counts did not appear at all.

### Stray electrons from field emission

Finally, even in the absence of light another origin of dark counts can be stray electrons created via field emission from small tips on the strongly negatively charged front of the ion CEM. Depending on the position of the emitting spot and the local field configuration these electrons can either directly impinge on the opposing electron detector or they are accelerated onto surrounding surfaces where they produce detectable x-rays via Bremsstrahlung. The latter effect is for example directly observable if electrons impinge on the glass walls of the vacuum chamber due the visible fluorescence that is emitted in the impact region. In the setup of trap 2 electrons that originated from the cable shoes contacting the front side of the ion detector and that were accelerated onto the glass walls caused count rates at the electron CEM that were on the order of $10^4 \ldots 10^5 \frac{\#}{sec}$. In that case the only possible solution was to switch the roles of the detectors so that the lower acceleration voltage $U_{acc}^{el}$ is applied to this CEM.

Table 4.1 summarizes the dark count rates of the ion and electron CEMs in the two trap setups. Both ion detectors have continuous dark count rates below one count per second. The residual

electron dark count rates are typically on the order of a few hundred counts per second and are attributed to field emission from the opposing negatively charged ion CEM. For both, electron and ion CEMs, this omnipresent background of dark counts leads to probabilities $p_{dc}$ of accidental detection events within a 200 ns time window that are well below the envisaged 0.1%. They can hence not significantly reduce the fidelity of the state readout.

### 4.1.4. Typical operating voltages

Table 4.2 summarizes the typical operating voltages of the CEM setup. In our experiment the necessary gain voltages range between 2.3 ... 3.2 kV, depending on the age of the detectors. They are chosen such that a mean pulse height of 100 ... 120 mV is achieved at the CEM's output. Both acceleration voltages $U_{acc}^{el,ion}$ at the front entrance of the detectors are always kept negative with respect to the surrounding sidewalls ($U_{SW}$) and the copper plates ($U_{CP}$) for shielding against stray electrons. For switching the roles of the CEMs (from ion detector to electron detector) only the acceleration voltages have to be interchanged. The actual values of $U_{SW\,1/2}$ and $U_{CP\,1/2}$ are finally chosen such that the detection efficiencies are maximized in the experiment with single trapped atoms.

| | |
|---|---|
| $U_{gain}$ | 2.3 ... 3.2 kV |
| $U_{acc}^{ion}$ | -4.0 ... -5 kV |
| $U_{acc}^{el}$ | -400...100 V |
| $\rightarrow \Delta U_{acc}$ = 3.6 ... 4.6 kV | |
| $U_{SW\,1/2}$ | -200 ... +200 V |
| $U_{CP\,1/2}$ | -200 ... +200 V |

Table 4.2.: Typical operating parameters for the channel electron multipliers and the electrodes for the transverse field components.

## 4.2. Method for determining the detection efficiencies

In the following it is explained how one can determine the detection efficiencies of each of the CEMs experimentally. Most importantly, the method does not require knowledge about the absolute number $N_{total}$ of ionization fragments that is created between the detectors. In any experimental scheme - be it ionization of atoms from the background vapor or ionization of single trapped atoms - it would be impossible to determine this number precisely. When using atoms from the background vapor this is due to a lack of knowledge of the local density of the atomic vapor, the velocity distribution of atoms crossing the intersection, the precise geometry of the intersection and so forth. When using single trapped atoms the situation evidently is much more well-defined. However, also here there is the possibility of unnoticed losses of the atom from the trap that do not lead to the creation of ionization fragments.

For determining the efficiencies one creates ionization fragments and counts the number of detection events $N_{el}$, $N_{ion}$ at the electron- and ion-detector together with the number of coin-

cidence events $N_{coinc}$. These are events where two particles are detected simultaneously - one at each of the detectors (of course the different times of flight due to the different masses and kinetic energies have to be considered). The respective detection efficiencies $\eta_{el}$ and $\eta_{ion}$ of the two fragments are then given by [76]:

$$\eta_{el} = \frac{N_{coinc}}{N_{ion}} \tag{4.1}$$

$$\eta_{ion} = \frac{N_{coinc}}{N_{el}} \tag{4.2}$$

In the presence of dark counts the event numbers $N_x$ still have to be corrected for the dark count rate of the respective detectors.

In the context of the state readout of single trapped atoms it is sufficient to detect at least one of the two ionization fragments in order to be able to decide that the atom was in the bright state of the state readout (see section 2.4). We are hence mainly interested in the combined probability $\eta_{comb}$ to detect at least one of the ionization fragments, i.e. the electron OR the ion. This can be calculated from the single particle detection efficiencies via:

$$\eta_{comb} = 1 - (1 - \eta_{el}) \cdot (1 - \eta_{ion}) \tag{4.3}$$

### Statistical errors

The combined detection efficiency $\eta_{comb}$ to detect a single trapped atom after the ionization is the key figure of merit for the setup of the charged particle detectors. To quantify its measurement error one starts with the errors of the single particle detection efficiencies $\Delta\eta_{el,ion}$. In the absence of CEM dark counts (as is approximately the case in experiments with single atoms) these can be obtained from the single particle and coincidence event numbers via [76]

$$\Delta\eta_{el,ion} = \frac{N_{coinc}}{N_{ion,el}} \sqrt{\left(\frac{1}{N_{coinc}} - \frac{1}{N_{ion,el}}\right)}. \tag{4.4}$$

This formula includes the statistical dependence (covariance) of the single particle and coincidence counts (for example, a coincidence can never be detected without an electron).

The efficiencies of the respective detectors are in turn indepentent variables. Thus the error of the combined efficiency $\eta_{comb}$ is simply given by the standard Gaussian error propagation for independent variables:

$$\begin{aligned} \Delta\eta_{comb} &= \sqrt{\left(\frac{\delta\eta_{comb}}{\delta\eta_{el}} \cdot \Delta\eta_{el}\right)^2 + \left(\frac{\delta\eta_{comb}}{\delta\eta_{ion}} \cdot \Delta\eta_{ion}\right)^2} \\ &= \sqrt{\left((1 - \eta_{ion}) \cdot \Delta\eta_{el}\right)^2 + \left((1 - \eta_{el}) \cdot \Delta\eta_{ion}\right)^2} \end{aligned} \tag{4.5}$$

## 4.3. Controlled shifting of the spatial volume with optimum detection efficiencies

The preceding work [28, 73] on the channel electron multipliers was mainly concerned with the aspects of detection time and efficiency. There the ion-electron pairs that were used to test the detectors did not originate from the ionization of single trapped atoms. Instead they were produced by probabilistic laser ionization of atoms in a thermal vapor of Rubidium atoms in the vacuum chamber. It was found that particles can be collected out of a cylindrical volume of a diameter of about 0.8 mm around the symmetry axis connecting the entrances of the detectors.

However, the detection efficiencies vary within this volume. This is due to the dependence of the detection efficiency on the angle of incidence of the impacting particle with respect to the detector surface, which is different for a hit on the detector cone and a hit into the channel at the exit of the cone. Hence it is possible that the highest efficiencies can be reliably obtained only out of smaller volumes. For integration of the detectors into a single atom trap a good overlap of the volume of optimal detection efficiencies with the position of the trap is required. It is, however, technically highly complex to align the relative position between the optical dipole trap and the vacuum setup incorporating the detectors to such a precision. This was a motivation to find a way that allows to optimize the overlap without having to move the entire setup. The solution are additional electrodes (the copper plates and the ITO-coated sidewalls of the glass cell from figure 4.3) that allow for fine tuning of the trajectories of the ionization fragments in transverse direction.

In the following section we examine the experimental feasibility of this approach. For this we make use of a method developed in [28, 73] that allows to construct a two-dimensional map of the detection efficiencies of particles originating from the central plane between the two detectors. With this method we want to observe experimentally whether it is possible to shift the collection volume of the detector setup to the necessary degree without reducing the optimal detection efficiencies. All measurements presented in this section were performed with the setup of trap 1 and the results were obtained in collaboration with my diploma student Kai Redeker [74].

### 4.3.1. Experimental scheme

Figure 4.4 depicts the experimental setup for measuring the two dimensional maps of the detection efficiencies. Two crossed laser beams create pairs of $^{87}Rb^{+}$-ions and electrons by 2-photon ionization of atoms from the vapor in the glass cell. Since ionization only takes place within the intersection of the beams, this provides a sufficient spatial definition of the origin of the ionization fragments. For sampling the two dimensional map the intersection is then scanned across the central $y'$-$z'$-plane between the detectors by displacing the respective beams. At each point the individual count rates at the electron and ion detector $N_{el}$ and $N_{ion}$ are determined together with the coincidence rate $N_{coinc}$, i.e. the rate of events where both, the electron and the ion from one ionization event, are detected. This set of data allows to extract the respective detection efficiencies $\eta_{el}$, $\eta_{ion}$ for electrons and ions originating from the addressed spatial volume (see section 4.2). Such scans are then performed for different sets of voltages applied to the

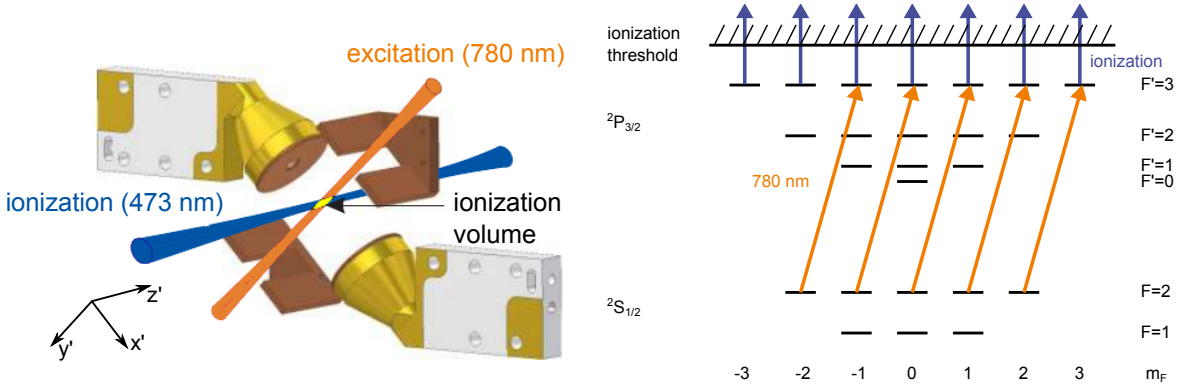


Figure 4.4.: Left: Setup for measuring the 2D-maps of the detection probabilities. The intersection of two crossed laser beams that create electron-ion pairs from the background vapor is scanned in the central plane between the detectors [28]. Right: Atomic level scheme with the transitions for the two-photon ionization.

transverse electrodes.

The presented method of ionizing from the atomic vapor delivers relatively high event rates, typically on the order of a few hundred to thousand events per second. This allows characterization of the detectors with a spatial resolution that would not be possible when taking single trapped atoms as particle sources. Here the loading time of the atom trap would strongly limit the event rate to about one to two events per second.

The level scheme in figure 4.4 shows the atomic transitions that are addressed during the two-photon ionization: A frequency stabilized near-infrared laser at 780 nm (see section 3.1.1) excites $^{87}Rb$-atoms from the $5S_{1/2}, F = 2$ ground state to the $5P_{3/2}, F' = 3$. A laser at 473 nm then delivers the remaining energy to ionize the atom. The specific transition for the 780 nm laser was selected due to its strong Clebsch-Gordan coefficients [30] for $F = 2 \rightarrow F' = 3$ that allow for faster excitation of the atom for a given laser power and hence higher event rates. A Zeeman state dependent ionization as it is envisaged for the readout scheme with single trapped atoms is not possible but also not necessary in this context.

## 4.3.2. Optical setup

The arrangement for scanning the cross-section of the ionizing laser beams works as follows: The ionization laser is incident parallel to the quantization axis which will later on be defined by the optical axis of the confocal microscope. The exciting laser at 780 nm is oriented perpendicular to the ionization laser under an angle of 45° with respect to the horizontal plane. Both beams originate from single mode optical fibers with the output couplers being mounted on stepper motor driven linear translation stages that allow to shift the beams within the x'-z-plane.

The beam waists at the intersection region are 90 µm for the ionization laser and 82 µm for the 780 nm laser. Their optical powers are 51 mW and 84 µW, respectively. At this power the resulting intensity of the 780 nm laser is above the saturation intensity of the $F = 2 \rightarrow F' = 3$

transition within a region of 75 µm around the beam axis. During the experiment the beams were displaced in step sizes of 50 µm.

The origin of the ionization fragments is thus less well-defined than those stemming from single atoms trapped in the optical dipole trap (see section 2.2.2). It is, however, still sufficient to resolve the basic spatial characteristics of the detector setup.

This experiment for characterizing the CEMs' detection efficiencies has been performed before the optical setup for the single atom trap was installed around the vacuum chamber. Otherwise the region of interest between the CEMs would have no more been accessible to the necessary extent.

### 4.3.3. Determination of single and coincidence count rates

The TTL output signals from the discriminators of the electron and ion CEM are read in in separate channels of a time tagging unit with a time resolution of 125 picoseconds. Evaluation of the registered events yields the electron and ion count rates. Coincidence events are identified by looking for electron events that are followed by an event at the ion detector within a given time window (see further below).

For each spatial position of the 2-D scans the data must be corrected for the current dark count rate of the detectors that would be present if no electron ion pairs were produced. This is accomplished by periodically switching the 780 nm laser on and off during the measurement. The switching happens in time intervals of 50 milliseconds with the help of an accousto-optical modulator. An auxiliary trigger signal indicating the switching of the laser is sent to another channel of the time tagging unit. The chosen duration of the on/off periods is well below the measurement time at each position which is on the order of seconds. In this way one also corrects for temporal drifts of the dark count rate on such short timescales. In order to account for possible dark counts triggered by the 473 nm ionization laser alone, the latter is continuously left on during the dark count measurement.

The dark count corrected count rates for electrons and ions are then given by:

$$\begin{aligned} N_{el} &= N'_{el} - N_{el}^{dark} \\ N_{ion} &= N'_{ion} - N_{ion}^{dark} \end{aligned}$$

with $N'_{el}$, $N'_{ion}$ being the number of counts collected during the time the 780 nm laser is switched on and $N_{el}^{dark}$, $N_{ion}^{dark}$ being the counts collected during the time the laser is switched off.

#### Filtering of spurious detection events

There are two types of spurious detection events that have to be filtered out for a correct determination of the count rates:

- events where a sufficiently high post-pulse oscillation of the signal from the CEM triggers the discriminator a second time after the end of its dead-time.

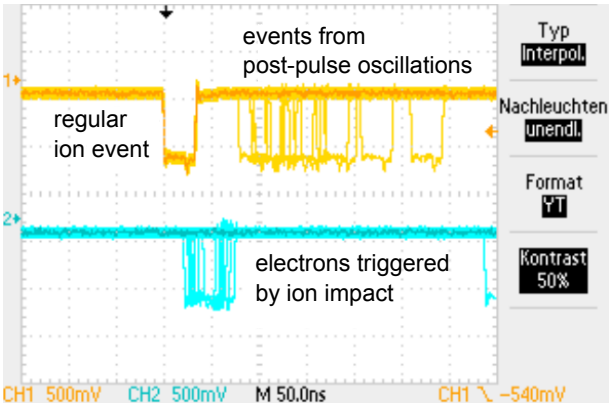


Figure 4.5.: Spurious detection events measured at the output of the discriminators of the ion-CEM (yellow) and electron-CEM (blue). The events were recorded with an oscilloscope with the display set to persistent mode.

- events where the impact of an ion on its CEM creates an electron that is accelerated into the opposing electron CEM thus leading to an additional electron detection event shortly after the ion detection.

Figure 4.5 shows an oscilloscope trace of these kind of events: Upon detection of a regular ion event additional events due to post-pulse oscillations are detected after the end of the dead time of the discriminator of 80 ns. This happens in up to 10% of the events. Electrons that are created during the ion impact are detected about 20-30 ns after the ion. These latter events happen with a much lower probability on the order of a few per mill.

Both effects lead to additional single particle detection events (electrons or ions) that do not coincide with the detection of a respective counterpart (ion or electron). They hence increase the measured single particle count rates but leave the coincidence count rate unaffected. According to equations 4.1 and 4.2 one will thus underestimate the detection efficiencies $\eta_{el}$ and $\eta_{ion}$.

To circumvent this problem the evaluation software for the timestamp files filters out these events. For filtering of the first kind of events we introduce time windows with a duration of 500 ns after each single particle detection. All secondary events at the same detector within this time window are discarded. For filtering of the second type of events all electron events within a time window of 75 ns after the detection of an ion are discarded. Longer time windows are not necessary and should also be avoided for the given event rates in order to minimize the occurrence of multiple independent ionization events within the same time window.

### Identification of coincidence events

Coincidence events are identified by searching for an ion after each detection of an electron. Due to their higher mass ions have a considerably longer time of flight to their detector than the electrons. Figure 4.6 shows a histogram of the differences of the time of flight between electrons and ions. In this example the accelerating potential difference $\Delta U_{acc}$ between the two CEMs was 4.3 kV. One can see that the ions arrive about 355 ns after the electrons within a time

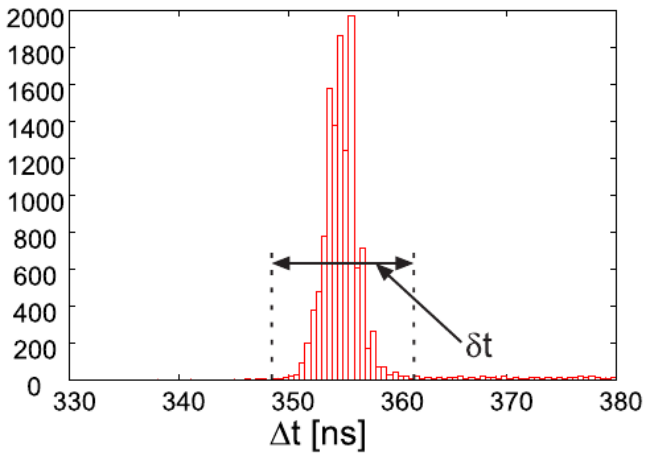


Figure 4.6.: Histogram of the difference in time of flight between the electron and the ion. The ion arrives at its detector about 355 ns after the electron [74].

window of less than 15 ns. In the 2-D scans the actual acceptance window for the ions was, however, chosen to be longer (typically on the order of 50 ns) since the time of flight shows slight variations depending on the position of the ionization volume. Still, this time window is by far short enough to be able to disregard possible coincidences due to dark counts.

### 4.3.4. Measurement results

The 2-D scans of the detection efficiencies were performed for a set of six voltage configurations at the ITO-coated glass walls and the copper plates. Table 4.3 lists the respective voltage configurations. Between scans I, II and III the electric potential was shifted along the quantization axis by varying the voltage differences between the ITO-coated side walls. In configuration II the difference is zero with both walls at -100 V and in configuration I and III it is $\pm$200 V. Here the voltage at the copper plates was left constant at 0 V. For scans IV, V and VI we varied the voltages at the copper plates and thus induced a shift perpendicular to the quantization axis. Scan V was taken with zero voltage difference and both plates at 0 V and in scans IV and VI the difference was $\pm$400 V. Here the voltage at the glass walls was left constant at -100 V.

Figures 4.7 and 4.8 show color maps of the resulting electron and ion detection efficiencies $\eta_{el}$,$\eta_{ion}$ as well as the combined efficiency $\eta_{comb}$. They have been derived from the dark count corrected count rates $N_{el}$, $N_{ion}$ and $N_{coinc}$ at the respective position via equations 4.1, 4.2 and 4.3. The measurement time per position was 5 seconds during which the exciting laser was periodically switched on and off for the correction of the dark counts as described in 4.3.3. In the center of the collection volume the dark count corrected count rates for electrons and ions were about 300 #/sec, resulting in about 750 single particle detection events per measurement point. The size of the scan area was 1$\times$1 millimeters in scans I-III and 1$\times$1.2 millimeters in scans IV-VI.

As one can see, electrons are only efficiently collected from a circular region with a diameter

| ITO-coated side walls | | | |
|---|---|---|---|
| I | $U_{SW1} = +200\text{V}$ | $U_{SW2} = 0\text{V}$ | $\Delta U_{SW} = -200\text{V}$ |
| II | $U_{SW1} = -100\text{V}$ | $U_{SW2} = -100\text{V}$ | $\Delta U_{SW} = 0\text{V}$ |
| III | $U_{SW1} = 0\text{V}$ | $U_{SW2} = +200\text{V}$ | $\Delta U_{SW} = +200\text{V}$ |
| Copper plates | | | |
| IV | $U_{CP1} = -200\text{V}$ | $U_{CP2} = +200\text{V}$ | $\Delta U_{CP} = -400\text{V}$ |
| V | $U_{CP1} = 0\text{V}$ | $U_{CP2} = 0\text{V}$ | $\Delta U_{CP} = 0\text{V}$ |
| VI | $U_{CP1} = +200\text{V}$ | $U_{CP2} = -200\text{V}$ | $\Delta U_{CP} = +400\text{V}$ |

Table 4.3.: Voltage configurations on the ITO-coated side walls and the copper plates during the 2-D scans in figures 4.7 and 4.8.

of about 0.6 mm. Within this region the electron detection efficiencies $\eta_{el}$ are homgeneously around 90%. However, outside this region the efficiencies quickly decrease to zero. In contrast to this the ion detection efficiencies $\eta_{ion}$, that are as well in the range of 90%, show noise-like fluctuations from point to point. These arise from the statistical variations of the comparably high electron CEM dark count rate (table 4.1) and hence a higher error in the determination of $N_{el}$. On the other hand the efficiencies do not drop to zero for larger distances from the center. But since one needs non-zero electron count rates to determine the ion efficiency (see equation 4.2), it not possible to determine the ion efficiency in the outer lying regions. Finally, the resulting combined detection efficiency $\eta_{comb}$ is on the order of 99% with variations on the order of $\pm 1\%$.

Scans I and III show that a voltage difference of 200 V between the sidewalls causes a shift of the collection volume of 0.24 mm along the z-axis with respect to the symmetric configuration. About the same shift (0.26 mm) is obtained along the x'-axis for a voltage difference of 400 V on the copper plates. There are two reasons why a higher potential difference is necessary at the copper plates for achieving the same amount of spatial shift of the collection volume. Firstly, the distance between the plates is larger than the distance between the glass walls. Secondly, due to their limited size the plates do not provide quasi infinitely large capacitor plates as the sidewalls do and thus have a different net effect on the potential along the symmetry axis of the detectors.

While the value of the efficiencies is almost fully unaffected by shifts along the x'-axis (figure 4.8) there is a significant decrease of the ion detection efficiencies for shifts along the quantization axis $z'$ (figure 4.7). The strongest effect can be observed in scan III where these efficiencies are reduced by about 10-15%. In general a reduction of the efficiencies can be expected for increasing field components perpendicular to the accelerating electrical field since this favors an impact of the ionization fragments on the outer segments of CEM's entrance cone which would happen under a less favorable angle of incidence as compared to an impact in the central region around the entrance of the channel (see [28] for a discussion of the influence of the angle of incidence on the gain of the detectors). This, however, should also occur when transverse fields are applied at the copper plates. Hence further investigation would be required to explain this observation.

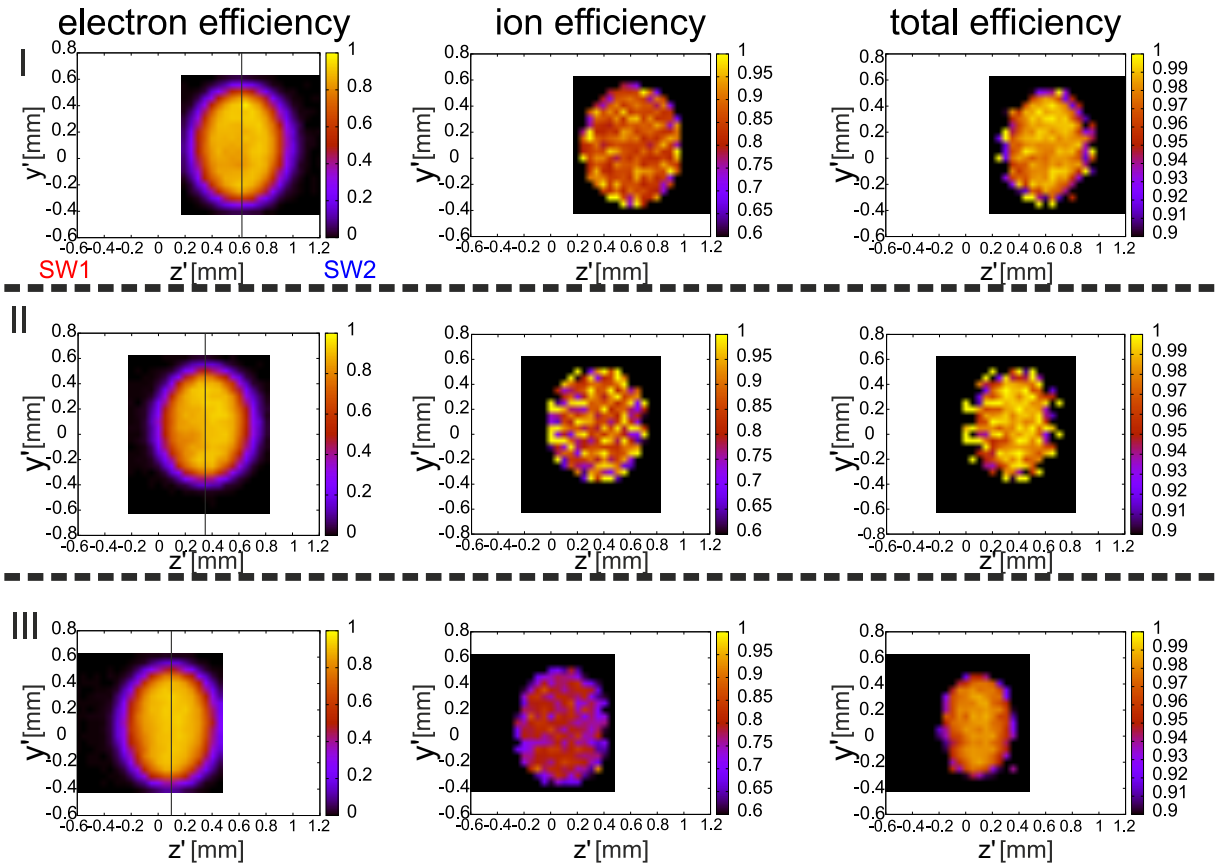


Figure 4.7.: 2-dimensional map of the detection efficiencies of the CEMs under variation of the voltage configuration at the sidewalls (SW1, SW2) of the vacuum chamber, i.e shift of the electric potential along the quantization axis. For voltage settings see table 4.3.

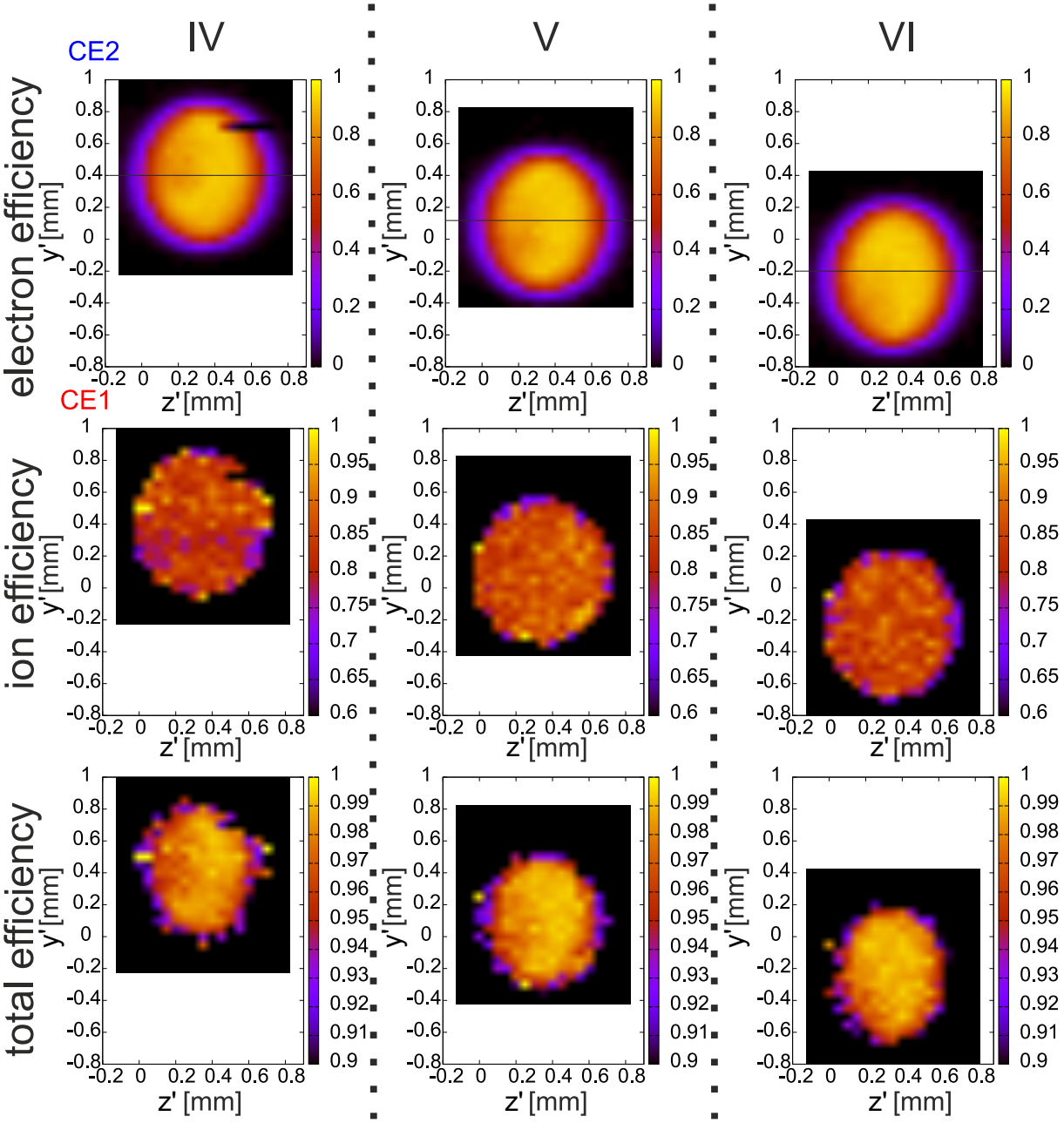


Figure 4.8.: 2-dimensional map of the detection efficiencies of the CEMs under variation of the voltage configuration at the copper electrodes (CE1, CE2). For voltage settings see table 4.3.

## 4.4. Optimization of the CEM detection efficiencies for single trapped atoms

During the integration of the optical dipole trap setup with the vacuum setup the position of the optical dipole trap was only coarsely aligned with respect to the collection volume of the particle detectors. The particle detection efficiencies for single trapped atoms hence had to be optimized in additional measurements. For this purpose the trapped atoms were ionized and the detection efficiencies were measured for different voltage configurations at the copper plates and the ITO-coated sidewalls of the glass cell.

### 4.4.1. Method

For the optimization of the particle detection efficiencies it is not necessary to create the ionization fragments via the Zeeman-state selective ionization. The simpler process from figure 4.4 (right) is fully sufficient for this purpose. For this, after the trapping of a single atom, the population of its electronic state is first optically pumped to the $F = 2$ hyperfine ground state using the repump laser of the MOT. Then the two lasers cycling and ionization are applied for ~400 ns which is more than twice the time that is expected to be necessary to fully ionize the atom. Just like in 4.3, the single particle detection efficiencies $\eta_{el}$ and $\eta_{ion}$ as well as the combined detection efficiency $\eta_{comb}$ are then calculated from the number of single particle detection events $N_{el}$, $N_{ion}$ and the number of coincidence events $N_{coinc}$ via equations 4.1, 4.2 and 4.3. Hence, the knowledge about the absolute number of created ionization fragments is again not necessary[6].

A correction for dark count events like in section 4.3.3 is not necessary in this measurement as the pulsed production of ionization fragments allows for a precise definition of an acceptance time window and hence a high signal-to-noise ratio[7]. There are also no considerable events from the ionization laser alone that could falsify the event rates. This can be seen from a histogram of the detection times of the ionization fragments as it is shown in figure 4.9. One can clearly see that there is no background noise from dark count events. The primary detection events of electrons (red) and ions (green) each happen within about 100 ns, separated by the time of flight difference of 360 ns. As in 4.3.3, secondary electron events originate from electrons created during the impact of ions in the ion-CEM (blue curve, 10 fold magnification) and secondary ion events from post-pulse oscillations of the primary ion detection event (violet). Again, these secondary events are discarded for the determination of the single and coincidence event numbers. The time intervals indicated by the horizontal arrows are the time windows where primary electron (left) and ion (right) detection events are accepted.

[6] One could also directly determine the detection efficiencies from the relative frequencies to detect the respective fragments after an ionization attempt. But this method is only fully reliable under the preconditions of perfect optical pumping, 100% ionization probability and if no atoms are lost from the trap at all via other loss channels before the ionizing laser pulses are applied. This, however, can not be guaranteed. See further below in this section.

[7] The probability to produce real ionization fragments in one attempt is close to unity, while the probability to detect a CEM dark count in the predefined acceptance time windows after the ionization is only on the order of $10^{-4}$.

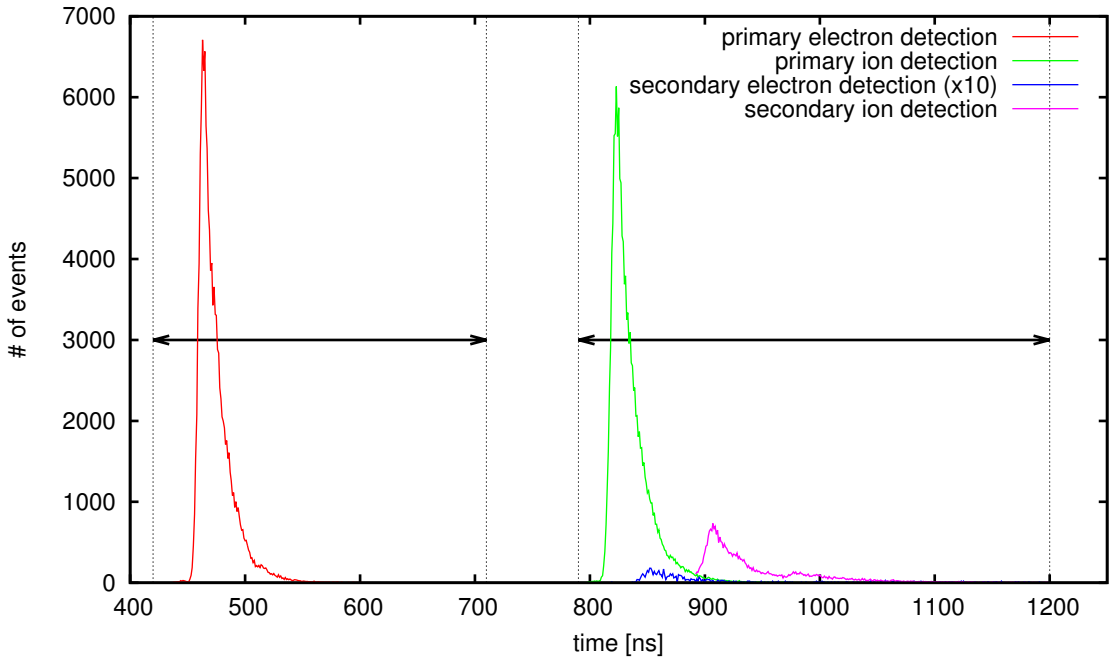


Figure 4.9.: Histogram of the detection times of the ionization fragments after the initialization of the hyperfine state selective ionization of single trapped atoms. The horizontal arrows indicate the acceptance time windows for primary electron and ion events.

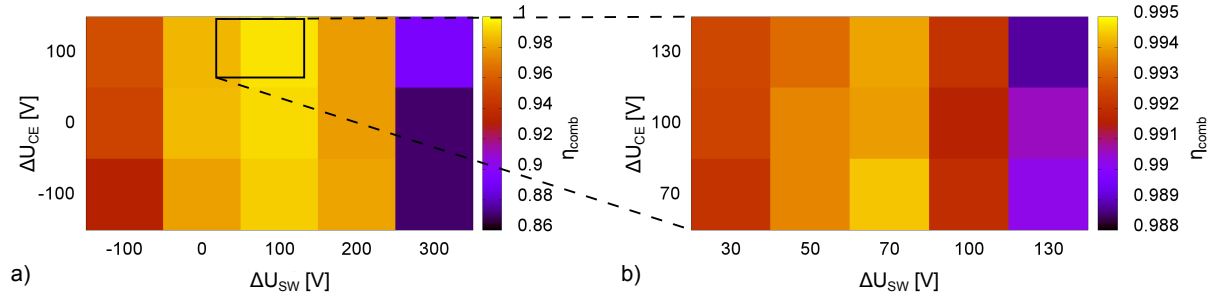


Figure 4.10.: Color maps of the combined detection efficiencies $\eta_{comb}$ for ionization fragments from single trapped atoms when varying the electric potential differences $\Delta U_{CE}$ and $\Delta U_{SW}$ between the copper electrodes and the ITO-coated sidewalls of the glass cell [55]. Note the different color scales.

### 4.4.2. Results

Throughout the measurement the voltage settings at the CEMs stayed fixed at $U_{acc}^{ion} = -4.3\,\text{kV}$, $U_{acc}^{el} = +50\,\text{V}$ and $U_{gain} = 3.2\,\text{kV}$. The scanned voltages $U_{CE1/CE2}$ and $U_{SW1/SW2}$ at the copper electrodes and the ITO-coated sidewalls of the glass cell were always kept below $U_{acc}^{el}$ in order to keep them attractive for stray electrons that could otherwise hit the electron CEM.

The extracted detection efficiencies are visualized in figures 4.10 a) and b). They show color maps of the combined detection efficiencies $\eta_{comb}$ as a function of the potential differences applied between the electrodes ($\Delta U_{CE} = U_{CE2} - U_{CE1}$) and the side walls ($\Delta U_{SW} = U_{SW2} - U_{SW1}$). Figure b) shows a scan with smaller step size in the region around $\Delta U_{CE} = 100\,\text{V}$ and $\Delta U_{SW} = 70\,\text{V}$, where the scan from figure a) yielded the highest efficiencies (note the different color scales of the two graphs). The event number per point is ~5000 in the measurement from figure a) and ~13000...16000 in figure b).

The maximum combined detection efficiency in figure b) is obtained for $\Delta U_{CE} = \Delta U_{SW} = 70\,\text{V}$. Here the single particle and coincidence event numbers were $N_{el} = 13991$, $N_{ion} = 14637$ and $N_{coinc} = 13167$. This yields detection efficiencies of $\eta_{el} = (89.96 \pm 0.25)\%$, $\eta_{ion} = (94.11 \pm 0.20)\%$ and a combined efficiency of $\eta_{comb} = (99.41 \pm 0.02)\%$ (errors calculated via equations 4.4 and 4.5). The experiments in the following chapter were performed with these settings.

In principle such two-dimensional scans should be able to reproduce a picture analogous to that from figures 4.7 and 4.8. However, the lower event rates (limited by the loading rate of the single atom trap) do not allow to perform these measurements with small step sizes over the entire region of interest and within a reasonable amount of time (the measurement of figure b) took 42 hours). This is especially the case if such small variations of $\eta_{comb}$ down to 0.1% are to be resolved with sufficiently small errors. Nonetheless one can e.g. clearly identify a maximum of $\eta_{comb}$ in figure a) in the horizontal direction for $\Delta U_{SW} = 100\,\text{V}$ and in the vertical direction for $\Delta U_{CE} = 100\,\text{V}$.

### 4.4.3. Hints for hidden mechanisms of atom loss

In order to gain information about the absolute probability to produce ionization fragments in an ionization attempt, also a fluorescence detection of the presence of the atom in the trap was performed after each event (see appendix B). This measurement revealed that the probability to detect no atom in the trap after the ionization is of (99.9±0.03)% and hence suggests that the probability that the atom is indeed ionized is close to unity. The remaining 0.1% could then be attributed to imperfect optical pumping or ionization. Together with the above measured probability $\eta_{comb} = 99.41\%$ to detect at least one of the fragments of all created electron-ion pairs, one would expect that the probability to see a fragment after an ionization attempt is 99.9% × 99.41% = 99.3%. However, by reanalyzing the data as suggested in footnote 6 one finds that after only (98.1±0.1)% of the ionization attempts at least one of the fragments is detected.

The observed difference of 99.3%-98.1%=1.2% is attributed to events where the loaded atom does not leave the trap due to being ionized but rather due to other loss channels that do not produce ionization fragments. This can be e.g. heating induced by the cooling and pumping beams that are applied before the ionization. In this case the actual experiment is performed without any atom in the trap. Also the repulsive force, that the strongly blue detuned ionization laser exerts on the atom, could be an explanation for the atom loss. But simulations of this latter process suggest that the duration, during which the laser is on, is too short to remove the atom from the trapping region.

We note here that at least the losses due to heating will not play a role in the following experiments on the Zeeman-state selective readout because there the presence of the atom in the trap is going to be additionally confirmed right before the ionization by the detection of the single photon that is emitted in the preceding atom-photon entanglement procedure.

## 4.5. Summary

The fragments from the laser-induced ionization of the single atoms are collected with two opposing channel electron multipliers that are placed at a distance of 8 mm from the position of the trap. The dark counts of the system are low enough to be able to exclude negative effects on the fidelity of the state readout.

From the single particle and coincidence count rates one can determine the single particle detection efficiencies and the combined probability $\eta_{comb}$ to detect at least one of the fragments. No knowledge of the absolute number of created ionization fragments is required. In measurements with atoms ionized from the background vapor it was found that the fragments are collected out of a cylindrical region with a diameter of ~0.6 mm. $\eta_{comb}$ reaches up to 99% over regions with a size of 0.3...0.4 mm.

Copper electrodes and the ITO coating on the inner walls of the glass cell allow for tuning of the accelerating electric field in transverse direction in order shift the spatial volume with good detection efficiencies. For shifts of ~0.3 mm no significant reduction of the detection efficiencies is observed. This simplifies the alignment of the detector setup with respect to the single atom

trap and allows to achieve the maximum detection efficiencies also with single trapped atoms. In this way the detection efficiency of trapped atoms can be optimized. The maximum combined efficiency $\eta_{comb}$ for trapped atoms was found to be $(99.41 \pm 0.02)\%$. A high fidelity of the ionization based atomic state readout is hence possible.

The duration of the detection of the fragments is mainly limited by the longer time of flight of the heavier ion. This is detected at its respective channel electron multiplier about 360 ns after the electron.

# 5. Experimental characterization of the atomic state readout

In this chapter we experimentally characterize the new readout scheme for single trapped atoms. The preparation of various atomic states is realized via the creation of entanglement between the atomic Zeeman state and the polarization of a single photon emitted by the atom as described in chapter 2. After the projection of the photonic polarization state the atomic state readout is initialized. The special interest of this chapter lies on the overall fidelity and duration of the readout. It starts with an overview over the experimental sequence and then treats the two main stages of the readout process - the laser-induced state selective ionization and the detection of the ionization fragments with the channel electron multipliers. In the end the readout is tested by measuring correlations in the photonic and atomic states for various measurement bases and comparing the results with those obtained from the fluorescence based detection method.

## 5.1. Experimental sequence

Figure 5.1 shows a schematic time diagram of the complete experimental sequence. It depicts the on/off statuses of the involved laser beams during the different stages of the experiment (loading of the single atom trap, optical pumping and preparation of atom-photon entanglement and finally the atomic state readout). All lasers are switched by a digital pattern generator [77]. Successful loading of the trap is signaled by a rise of fluorescence collected with the confocal microscope. The PC monitoring the fluorescence then triggers the switching to the optical pumping pattern. Optical pumping and excitation of the atom are repeated until a single photon from the atom-photon entanglement process is detected. After every forty unsuccessful pumping and excitation attempts the atom is cooled again for 200 µs. The detection of a single photon after the excitation indicates the successful projection of the photonic polarization state and thereby successful preparation of the atomic state. The lasers are then switched to the pattern for the atomic state readout.

In the following experiments the overall time delay between the creation of atom-photon entanglement and the initialization of the atomic state readout is well below 1 µs. This is short enough to be able to exclude any significant impact of sources of decoherence on the atomic Zeeman state[1]. Deviations of the measurement results from what could be expected from a perfect entangled state can hence be mostly attributed to imperfections during the preparation of entanglement or the atomic state readout.

[1] In the experiment magnetic fields are actively stabilized to 0.5 mG with magnetic field coils in a closed feedback control loop [40].

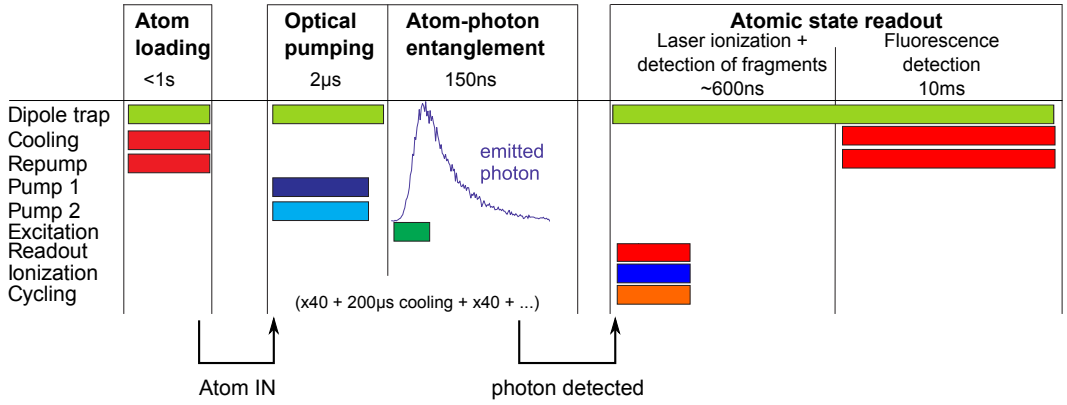


Figure 5.1.: Experimental sequence for the atomic state preparation via atom-photon entanglement and the subsequent readout of the atomic state. The diagram shows which lasers are used during the different stages of the experiment. Switching between the stages happens upon signals that indicate successful loading of the trap or detection of a photon after the atom-photon entanglement.

In addition to the detection of the ionization fragments that finalizes the projection of the atomic state we also perform the fluorescence based detection of the presence of the atom in the trap (see appendix B).

## 5.2. Laser induced Zeeman state-selective ionization

For characterizing the laser induced ionization process we run the full experiment described in 5.1 and measure the ionization probabilites of atoms that have been prepared in the dark and bright state of the atomic state readout. In the envisaged Bell-experiment we reserve a maximum duration of 200 ns for the laser ionization. The laser pulse parameters were hence optimized for an optimum contrast in the discrimination between bright and dark state within this predefined time window. In the end we compare the experimentally determined ionization probabilities with those obtained in the numerical simulations from 2.4.2.

### 5.2.1. Optical pulse sequence

Figure 5.2 shows traces of the temporal pulse shapes of the laser pulses measured with photo diodes. The power of the ionization laser settles to a stable value about 60 ns after the switching. The readout and cycling laser are hence switched on with an appropriate delay. In the following measurements both, the ionization laser as well as the cycling laser, are on for a fixed duration of 360 ns and with fixed intensities. The peak intensity of the ionization laser in the center of the focus is $I_{ion}(0,0) = \frac{2 \cdot 200\,\mathrm{mW}}{\pi w_0^2} \approx 11.1 \cdot 10^9\ \frac{\mathrm{mW}}{\mathrm{cm}^2}$. In separate measurements this intensity was found to deliver an ionization rate of the $P_{3/2}$ excited state of $\Gamma_{ion} = 3.32 \cdot \Gamma_1$. The duration and intensity of the readout laser are varied with the acoustic-optical modulator in order to find the

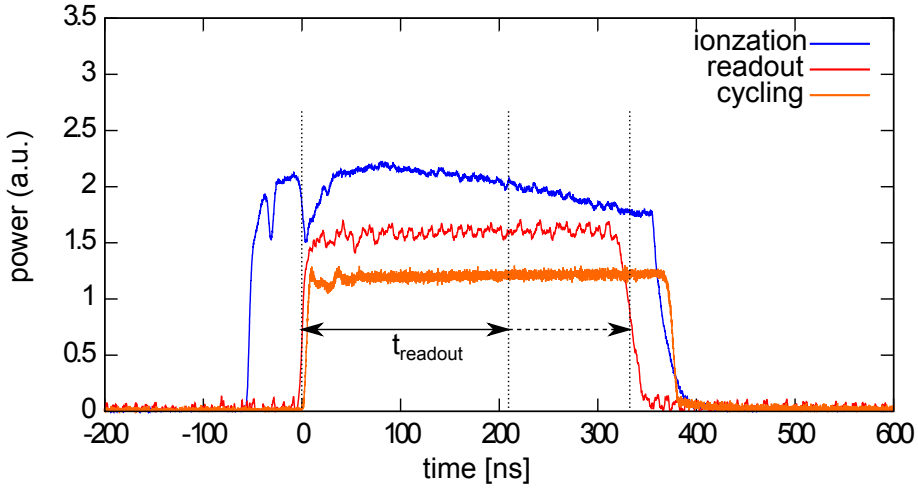


Figure 5.2.: Experimental laser pulse sequence for the Zeeman-state selective ionization. To characterize the temporal behaviour of the process, the duration $t_{readout}$ of the readout laser is varied.

pulse parameters that yield the optimum contrast.

### 5.2.2. Optimum pulse duration and intensity

In the following measurements the photons from the entangled atom-photon pair were analyzed in the $H/V$-basis and the polarization of the readout laser was $V$. According to table 2.1 the bright and dark state of the laser induced ionization process are then:

$$\begin{aligned} \psi_{bright} &= \frac{1}{\sqrt{2}}\left(|1,+1\rangle + |1,-1\rangle\right) \\ \psi_{dark} &= \frac{1}{\sqrt{2}}\left(|1,+1\rangle - |1,-1\rangle\right) \end{aligned}$$

Figures 5.3 and 5.4 show the ionization probabilities of the two states when the pulse parameters are varied. The blue curves in the figures contain the events where the photonic state readout projected the polarization of the photon onto $H$. As can be seen from equation 2.8, this projection prepares the atom in the bright state of the state readout. The red curves in contrast contain the events where the photon was projected onto $V$ - thus yielding an atom in the dark state of the readout.

In order to find the optimum pulse duration and intensity, the ionization probabilities of the bright and dark state and the resulting contrast were measured under iterative variation of these parameters. The best results for the contrast where obtained in the measurement shown in figure 5.3. Here the readout duration was varied, while the readout power was kept fixed at 1.24 µW [2].

[2]Due to uncertainties in the actual intensity at the position of the atom, this power cannot be directly compared to those from the numerical simulations. See following section.

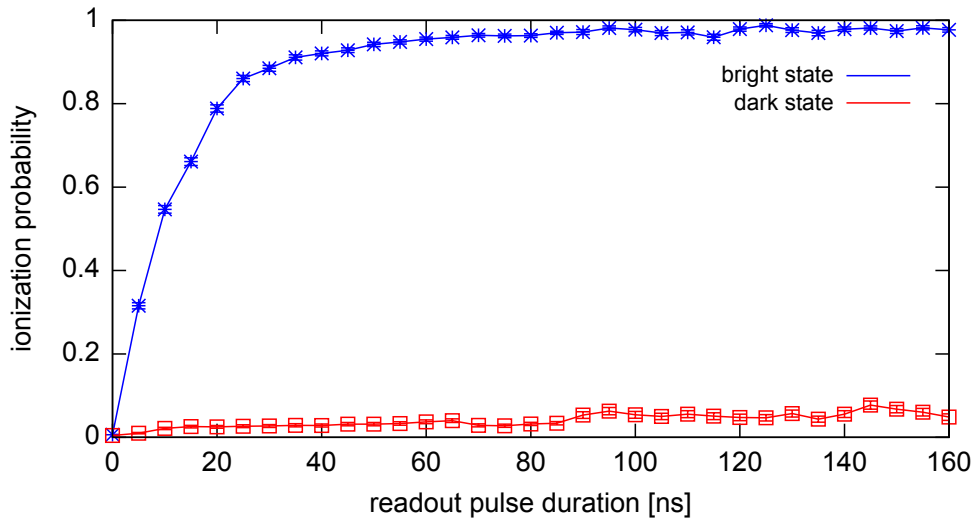


Figure 5.3.: Measurement of the dependency of the ionization probabilities of bright and dark state under variation of the duration of the readout laser pulse.

One can clearly see the saturation of the ionization probability of the bright state (blue curve) and the ongoing linear increase of the ionization of the dark state (red curve). For pulse durations in the range of 120 ... 140 ns the contrast lies between 92% and 94%. Variations are due to statistical errors.

Figure 5.4 shows a measurement where the readout laser power was varied at a fixed pulse duration of 140 ns. Also in this case the ionization probability of the bright state saturates while that of the dark state increases linearly. For a power of 1.24 µW the measured contrast is 93.8%.

Both of these graphs show the ionization probabilities that were determined using the channel electron multipliers and not the fluorescence detection. The values hence include the reduced combined particle detection efficiency $\eta_{comb}$ of 99.41%.

### 5.2.3. Comparison of simulation and measurement

We now compare the results from the measurement with the predictions from the numerical simulations in section 2.4.2. The dashed lines in figure 5.4 show predictions from the simulation for a pulse duration of 140 ns.

To account for the lack of knowledge of the precise intensity of the laser beam at the position of the atom, the curves from the simulation were stretched in the horizontal direction. The stretching factor was chosen such that the agreement with the measured data for the bright state is optimized, as this state shows the most pronounced dependency on the readout power. Moreover, the simulation for the bright state was corrected for the combined detection efficiency $\eta_{comb}$=99.41% to actually see at least one of the ionization fragments. As one can see this yields a good agreement between measurement and theory in the case of the bright state.

However, when stretching the simulated curve for the dark state by the same factor, at the

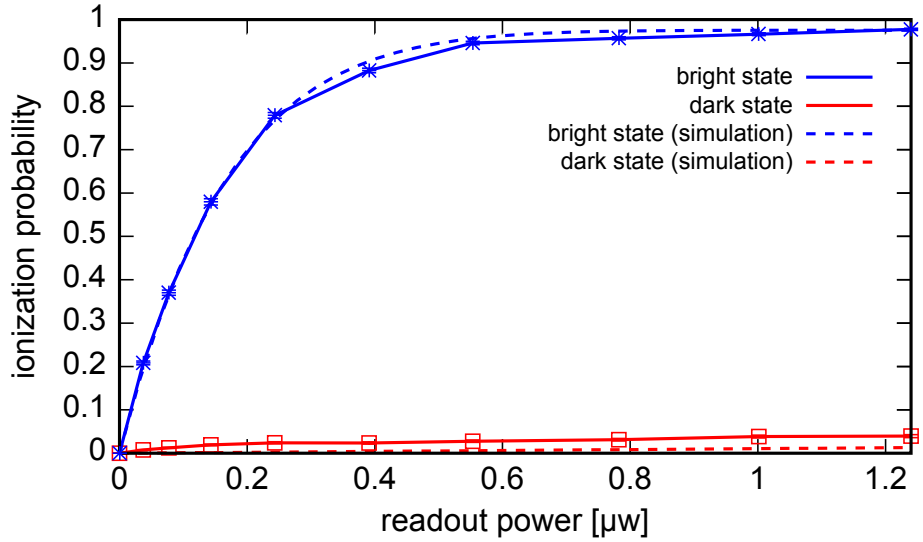


Figure 5.4.: Dependency of the ionization probabilities of the bright state (blue curves) and dark state (red curves) on the power of the readout laser. The solid lines show the results from the measurement. The dashed lines were obtained with the numerical simulations and were stretched in the horizontal direction in order to correct for uncertainties in the actual intensity at the position of the atom. While the behavior of atoms prepared in the bright state is well reproduced, the results for atoms in the dark state differ significantly.

power of 1.24 µW the experimental results yield a significantly higher ionization probability $p_{dark}^{exp} = (3.95 \pm 0.34)\,\%$ than what is predicted from the simulation $(1.30\%)$. To a small extent this significant difference can be explained by the fact, that in the experiment errors in the preparation of the atomic state or polarization errors of the readout laser also allow for a resonant excitation of atoms that were supposedly prepared in the dark state. This was not considered in the simulations. A closer analysis of the temporal evolution of the ionization of the dark state in section 5.3 shows that a relative ratio of $r_{res} = 33.4\%$ of the ionization events can be explained by such imperfections while the remaining $r_{or} = 66.6\%$ still seem to originate from off-resonant excitation of the dark state. This means that experimental imperfections lead to a probability $p_{dark}^{res}$ to resonantly ionize the dark state of

$$p_{dark}^{res} = r_{res} \cdot p_{dark}^{exp} = 33.4\% \cdot 3.95\% = 1.32\% \tag{5.1}$$

while the inherent possibility of off-resonant excitation leads to an ionization probability $p_{dark}^{or}$ of

$$p_{dark}^{or} = r_{or} \cdot p_{dark}^{exp} = 66.6\% \cdot 3.95\% = 2.63\% \tag{5.2}$$

This latter value is still a strong deviation from the expectations from the simulation and an explanation for this requires further investigation.

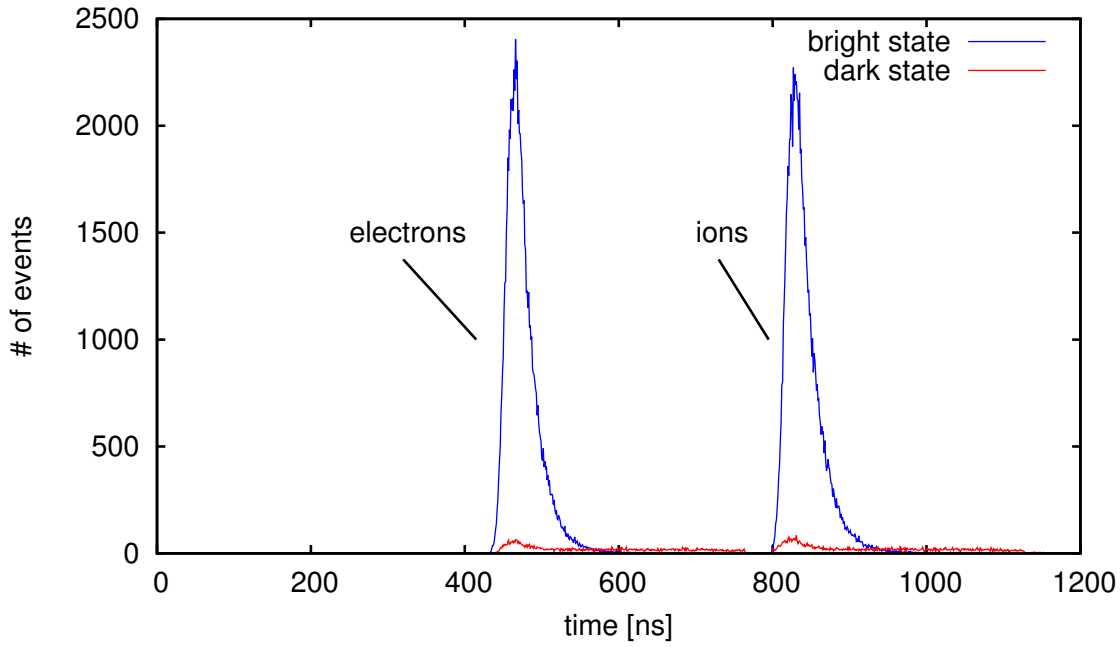


Figure 5.5.: Histogram of the detection times of the ionization fragments from a Zeeman-state selective ionization. Blue curve: fragments from atoms prepared in the bright state of the readout. Red curve: fragments from atoms in the dark state.

### 5.2.4. Upper bound for the errors in the atomic state preparation

During the introduction of the atomic state preparation via atom-photon entanglement possible sources of error in this process had been discussed (section 2.3.5). The extracted value of $p_{dark}^{res} = 1.32\%$ from equation 5.1 gives an upper bound for the summed probability of the different types of error. The polarization and alignment errors of the readout laser that also contribute to $p_{dark}^{res}$ have been measured to be comparably small (sections 3.1.3 and 3.1.5). It seems hence justified to attribute a large proportion of $p_{dark}^{res}$ to errors in the atomic state preparation.

## 5.3. Analysis of the ionization fragments from the state selective readout

As it turns out, further insight into the properties of the laser ionization can be gained from the histograms of the detection times of the two ionization fragments.

An example for such a histogram is depicted in figure 5.5. The readout power in this measurement was 1.24 µW. Also in these measurements the photons from the entangled atom-photon pair were analyzed in the $H/V$-basis and the polarization of the readout laser was $V$. The blue curve shows the events where the photonic polarization readout yielded $H$ thus preparing the atom in the bright state. The red curve shows events where the atom has been prepared in the dark state.

Regarding the temporal shape of the histograms one recognizes a fundamental difference between the $\psi_{bright}$ and $\psi_{dark}$. In this measurement the laser pulses for the atomic state readout were left on for 320 ns. From the width of the blue histograms of the electron and ion detections one can see that the bright state gets fully ionized within less than 200 ns. However, in the case of the dark state, detection events occur over the entire duration of the laser pulses. This characteristic gives hints about the different origins of the unwanted ionization of the dark state as well as their relative probabilities.

## 5.3.1. Origin of the unwanted ionization of the dark state

In order to examine the ionization of the dark state more closely we magnify the red histogram from figure 5.5 (see figure 5.6). It is composed of two major contributions:

- An accumulation of events at the beginning of the ionization process
- and a constant background of detection events over the full duration of the ionizing laser pulses.

By comparing the temporal shape of the peak in the beginning of the histogram to that of fragments from the ionization of the bright state (blue dashed curves in the figure) one can derive that this contribution must come from a resonant excitation of the atom. This can occur if the atom has not properly been prepared in the dark state of the readout or due to polarization errors of the readout laser. It can then be resonantly excited to the $P_{1/2}, F' = 1$ manifold. The constant background is attributed to the off-resonant excitation of the dark state to $P_{1/2}, F' = 2$. Due to the off-resonant coupling this process leads to a very slow ionization of the population in the dark state and hence an almost constant ionization rate.

### Relative probabilities of the resonant and off-resonant excitation processes

It is possible to estimate the relative probabilities of the resonant and off-resonant contributions from the histogram in figure 5.6. The total number of events due to off-resonant excitation $N_{or}$ is given by the area of the rectangularly shaped part of the histogram below the horizontal dotted line. The number of events due to resonant excitation $N_{res}$ is given by the surface of the remaining part above the dotted line. From the histogram of the electron events one obtains for a constant off-resonant excitation rate of $\approx (17 \pm 1)\frac{1}{\mathrm{ns}}$ (see dotted line):

$$N_{or} = (17 \pm 1)\frac{1}{\mathrm{ns}} \cdot 320\mathrm{ns} = 5440 \pm 320$$

With a total event number $N_{ges} = 6634$ it follows:

$$N_{res} = N_{ges} - N_{or} = 1194 \pm 320$$

The relative ratios of ionization events due to resonant and off-resonant excitation, $r_{res}$ and $r_{or}$, are then:

$$\begin{aligned} r_{res} &= \tfrac{N_{res}}{N_{ges}} &&= (18.00 \pm 4.82)\% \\ r_{or} &= \tfrac{N_{or}}{N_{ges}} &&= (82.00 \pm 4.82)\% \end{aligned}$$

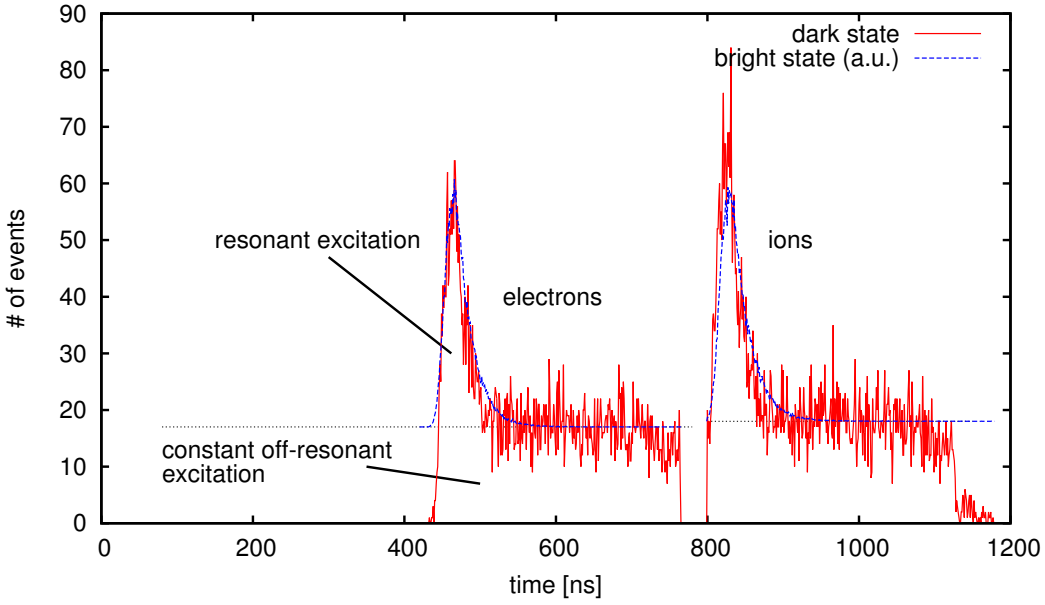


Figure 5.6.: Histogram of the detection times of fragments from the dark state (red line). It is composed of a constant background over the full duration of the laser ionization and a pronounced peak in the beginning. The blue dotted line shows a rescaled histogram of fragments from the bright state for comparison of the temporal evolution.

These are the results for a readout pulse duration of 320 nanoseconds. However, as stated in the previous section, the optimal pulse duration is rather on the order of 140 ns. When neglecting all further detection events, the above ratios become:

$$r_{res} = 33.4\% \tag{5.3}$$
$$r_{or} = 66.6\% \tag{5.4}$$

This means that at a pulse duration of 140 ns one third of the ionization events of the dark state happen via resonant excitation due to wrong preparation of the atomic state or errors in the readout polarization. Two third of the events can be attributed to off-resonant excitation to the neighboring $F' = 2$ hyperfine state.

### 5.3.2. Optimal acceptance time window

To optimize the quality of the readout scheme one can define a time window within which ionization fragments are accepted. All detection events outside of this window are discarded and the atom is considered to having been in the dark state of the readout. The scans in figure 5.3 show that the optimum contrast is achieved for a duration $T$ of 130 to 140 nanoseconds. This is also reflected in the histograms of the detection times of the ionization fragments. Figure 5.7 shows a close-up view of the histogram from figure 5.5. One observes that after $T$=140 ns the ionization

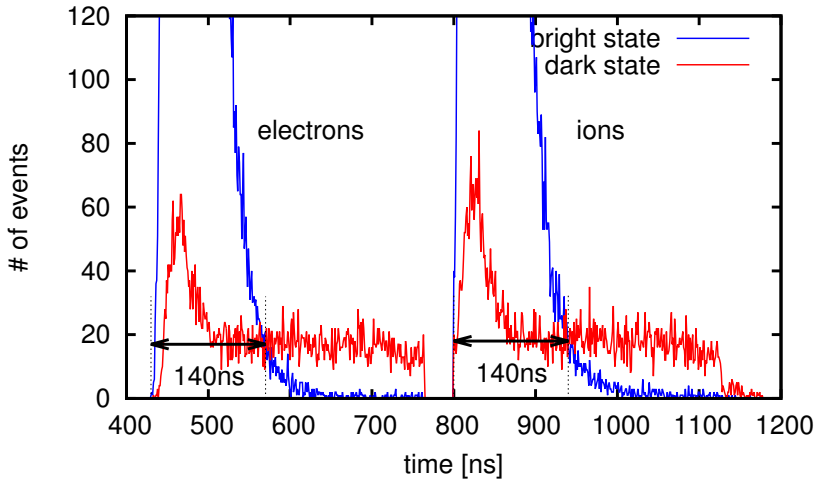


Figure 5.7.: Magnification of the histogram from figure 5.5. The ionization rate of the dark state starts to exceed that of the bright state after a pulse duration of 140 ns. The vertical dotted lines hence indicate the optimal acceptance time windows for the ionization fragments that maximize the contrast of the atomic state readout.

rate of the bright state falls below that of the dark state, i.e.

$$\frac{d}{dT}p_{bright}(T) \gtrless \frac{d}{dT}p_{dark}(T)\,, \text{ for } T \lessgtr 140\,\text{ns}$$

Since the contrast is defined as $c(T) = p_{bright}(T) - p_{dark}(T)$ it follows $\frac{d}{dT}c(140\,\text{ns}) = 0$ and the contrast has a maximum at this duration.

In general, the implementation of such a time window is redundant to setting the duration of the readout laser pulse to this optimum value. However, in order to minimize any impact of potential CEM dark count events on the state readout a restrictive choice of this time window is still recommended. During experiments on the characterization of the readout or the atom-photon entanglement this time window can be implemented in the evaluation software. To close the locality loophole in a Bell experiment, however, the detection events have to be filtered in real time since this filtering influences the measurement outcome and must hence be considered to be part of the measurement process. Therefore a logic AND operation is applied between the output signals of the CEMs and a second signal which defines the acceptance time window.

## 5.4. Overall duration of the state readout

The overall duration that is relevant for closing the locality loophole in a Bell experiment is measured from the moment when the measurement basis has been determined until the moment when a definite (classical) answer about the state of the observed particle is obtained. In the envisaged Bell experiment the choice of the measurement basis will be given by a random number ($\in \{0, 1\}$) that is retrieved from a continuously running quantum random number generator

(QRNG) [78]. This number decides which of the two accousto-optic modulators, that switch the power of the readout beams with the two polarizations, is activated (see section 3.1.4). This QRNG was not employed within this thesis. In our case the AOMs are directly addressed by the digital pattern generator. As a starting point of our measurements we take the time when this device sends the electric pulse to the driving electronics of the AOMs. The readout ends at end of the 140 ns long time window within which the slower fragments - the ions - are accepted.

In order to obtain a definite value for the overall duration of the readout we look at the time histogram in figure 5.7. In this histogram the digital pattern generator sends the pulse for switching the AOM drivers at time $t = 120$ ns. From this moment it takes 310 ns until the first output signal from the electron CEM is detected (rising edge of the blue electron histogram at $t = 430$ ns). This duration includes the delay for switching the AOM, the optical delay until the laser pulse reaches the atom, the time of flight of the electron, the throughput delay of the CEM and the subsequent discriminator, the logic AND operation with the acceptance time window and all delays in cables until the electric pulse reaches the time tagging unit. The observer can make a definite statement of the result of the readout at the end of the acceptance time window for the ions at $t = 940$ ns. The overall duration of the readout hence is 940 ns - 120 ns = 820 ns.

For estimating the overall duration in a Bell experiment closing the locality loophole we include the time needed for setting the measurement basis according to a random number. Including delays in cables, the throughput delay of the QRNG after the request of a random number and the maximum age of the random number at the moment of request[3], this delay is smaller than 100 ns resulting in an overall duration shorter than (820+100) ns=920 ns. This is well below the admitted duration of 1.3 µs in a Bell experiment with a distance of 400 meters between the two atoms. The presented atomic state readout is hence fast enough to close the locality loophole.

## 5.5. Atom-photon correlations

### 5.5.1. Measurement procedure

In the end of this thesis we test the ability of the atomic state readout to conduct projection measurements in different measurement bases. For measuring the atom-photon correlations we repeatedly create entangled atom-photon pairs and project the photons in the $H/V$- or $\pm 45°$-basis. For the subsequent readout of the atoms we vary the polarization angle of the linearly polarized readout laser. For each result of the photon projection we determine the relative frequency to detect no ionization fragment after the laser ionization as well as the relative frequency to redetect the atom in the trap via the fluorescence detection.

Figure 5.8 illustrates the correlations between the results from the photonic and atomic state readouts. The two graphs in the left column show the results from the readout with the channel electron multipliers while the graphs in the right column show those obtained with the fluorescence detection. In the graphs in the top row the photonic readout basis was $H/V$, in the bottom row it was $\pm 45°$ . The curves depict the relative frequencies to detect no ionization fragment after the state selective laser ionization of the atom - or to redetect the atom via its fluorescence

[3]The actual starting point of the measurement is when the random number has been generated in the QRNG.

| | CEMs | | fluorescence detection | |
|---|---|---|---|---|
| | visibility | phase shift | visibility | phase shift |
| black | 0.9363±0.0043 | 1.4°±0.1° | 0.9452±0.0040 | 1.4°±0.1° |
| green | 0.9063±0.0050 | 0.3°±0.1° | 0.9157±0.0048 | 0.3°±0.1° |
| blue | 0.9071±0.0060 | 1.3°±0.1° | 0.9179±0.0058 | 1.3°±0.1° |
| red | 0.9219±0.0045 | 0.6°±0.1° | 0.9316±0.0043 | 0.6°±0.1° |

Table 5.1.: Visibilities (peak-to-peak amplitudes) of the fitted sine curves in figure 5.8 together with the phase shifts (horizontal shifts with respect to the ideal case).

- for a given angle setting of the $\lambda/2$-plate in the beam path of the readout laser. An angle of $0°$ yields a readout polarization of $V$, 22.5° yields $+45°$ and so forth. The probabilities for each measurement point are derived from 2000-3000 events (total measurement time 61 hours).

### 5.5.2. Analysis of the results

The data for each polarization state of the detected photon was fitted with a sinusoidal function. The main figures of merit that one obtains from these data are again the contrasts between the ionization of atoms prepared in the bright and dark state at given polarizations of the readout laser as well as the visibilities of the fitted sine functions.

For the photonic basis $H/V$ the contrasts for the CEM- and fluorescence-based detection $c_{CEM}$ and $c_{fluo}$ at the readout polarization $V$ are: $c_{CEM}(V) = 0.9274 \pm 0.0079$ and $c_{fluo}(V) = 0.9325 \pm 0.0077$. In the photonic basis $\pm 45°$ at the readout polarization $+45°$ one obtains: $c_{CEM}(45°) = 0.9060 \pm 0.0089$ and $c_{fluo}(45°) = 0.9182 \pm 0.0083$. The value of $c_{CEM}(V)$ is slightly but not very significantly smaller than the optimum contrast of 93.8% from section 5.2.2. In addition to statistical errors this difference is also due to a slightly decreased combined detection efficiency of the CEMs in this measurement (only 98.9% instead of the original $p_{comb}$=99.41% after several high-voltage breakthroughs). Moreover, the contrasts in the $45°$-basis are lower than those in the $H/V$-basis. This is attributed to additional polarization errors that are introduced by imperfections of the employed $\lambda$/2-plate in the photonic state analysis, which is not present in the $H/V$-basis.

Table 5.1 lists the visibilities, i.e. the peak-to-peak amplitudes, of the fitted sine curves together with the phase shifts of the curves with respect to the ideal case[4]. From the phase shifts one can derive that the relative error of the linear polarizations of the polarization detection of the single photon and the readout laser are of at most 1.4°. As can be estimated from the curvature at the maxima and minima this phase shift does not have a considerable influence on the contrast at these respective points. Circular polarization components of the projected photons or the readout laser would lead to a global reduction of the visibilities. Their effect can hence not be directly seen here, but also these components had been measured to be small (see section on the setup). Also errors in the preparation of atom-photon entanglement have been determined to be of at

[4]The phase of the sine functions is a free fit parameter in this analysis and accounts for polarization errors of the photonic measurement basis and the readout laser.

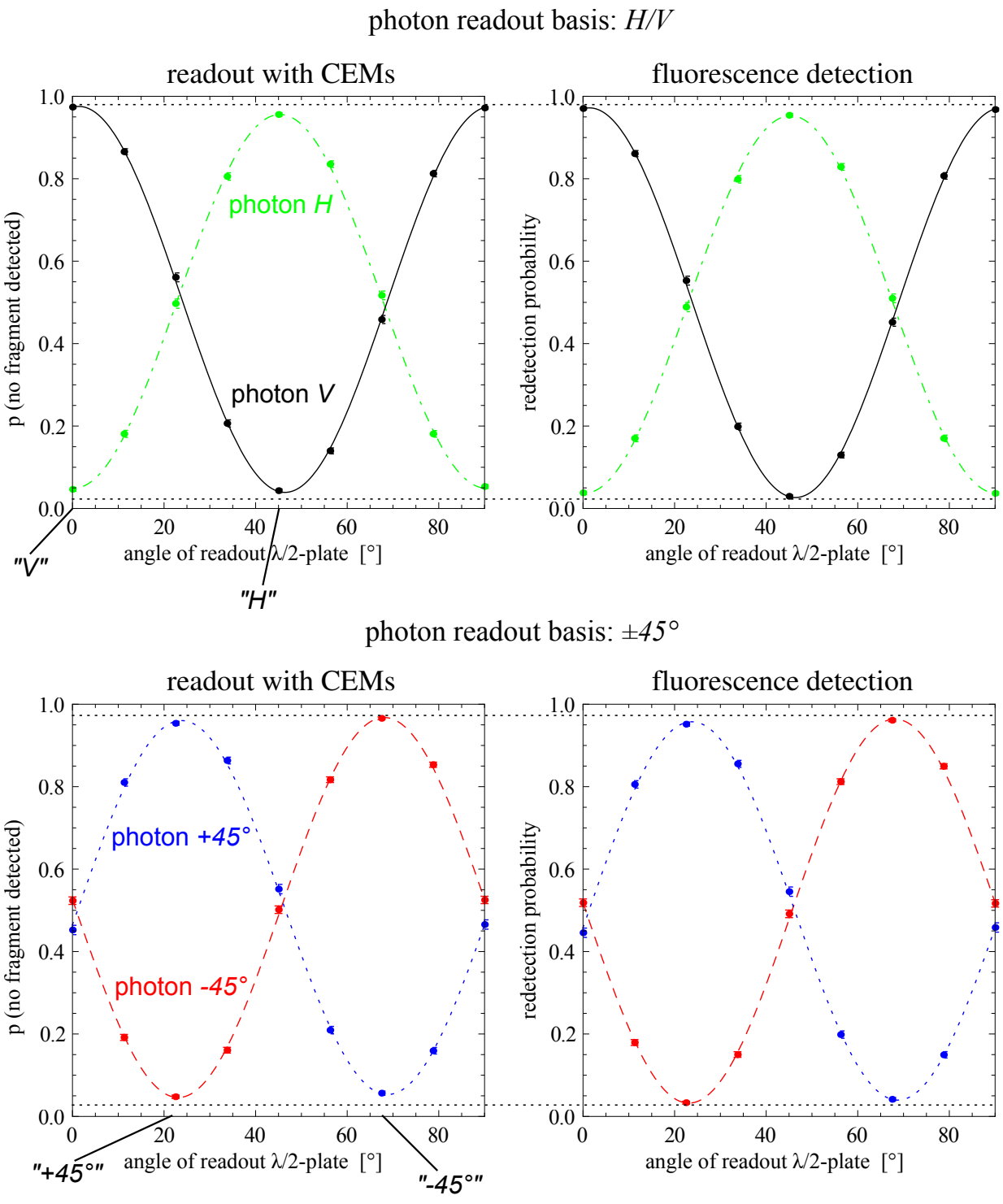


Figure 5.8.: Atom-photon correlation curves for the photonic measurement bases $H/V$ (top row) and $\pm 45°$ (bottom row). Starting from $V$ the linear polarization of the readout laser is rotated over a range of 180°. The left column shows the results from the CEM-based atomic state readout while the left column shows those from the fluorescence detection.

most 1.32% (section 5.2.4). It seems thus justified to attribute the reduction of the visibilities with respect to a perfectly entangled state (100% visibility) mainly to errors of the state readout.

When carefully comparing the correlation curves for the readout with the CEMs and the fluorescence detection, one recognizes that the curves for the fluorescence detection are slightly shifted downwards (see the horizontal dotted lines). The downward shift of the maxima reflects the possible atom losses during the fluorescence detection that lead to a reduced redetection probability of atoms in the dark state. The downward shift of the minima results from the better identification of the bright state with the fluorescence detection due to the non-unity detection efficiency of the CEMs.

### Suitability for a Bell experiment

To estimate whether the presented atomic state readout is suitable for a Bell experiment with two distant atoms we compare the above visibilities of the atom-photon correlations with those from a previous atom-atom entanglement setup that already demonstrated a violation of Bell's inequality. In [26] the atomic state readout was based on a Zeeman selective STIRAP transfer of a chosen qubit state to the $F = 2$ hyperfine ground state. A subsequent hyperfine state selective laser pulse then removed the atom from the trap and the state projection was finalized with a fluorescence detection of the presence of the atom in the trap. With this method the visibilities of the two trap setups were in the range of 0.869 to 0.901 and allowed for a violation of Bell's inequality by two standard deviations. The presented new fast state readout delivers significantly higher visibilities. Assuming the same fidelity of the prepared atom-atom state this promises to allow for another successful Bell experiment.

## 5.6. Summary

This chapter characterized the Zeeman state selective atomic state readout with the help of measurements on single trapped Rubidium 87 atoms.

The pulse parameters of the lasers in the Zeeman state selective ionization were optimized to yield the maximum possible discrimination of the bright and dark state of the ionization process. Using the detection of the ionization fragments to finalize the state projection the achievable contrast was found to be 93.8%. Also after correction for the detection efficiency of the CEMs this is smaller than the 97% predicted by the numerical simulations. A closer analysis of the histogram of the detection times of the two ionization fragments showed that the difference between measurement and theory has two reasons. First, it is due to resonant excitation and subsequent ionization of the dark state with a probability of $p_{dark}^{res} = 1.32\%$. This is mainly attributed to errors in the preparation of the atom photon entanglement. Such effects were not considered in the simulation. Second, the off-resonant excitation of the dark state seems to be stronger than what is predicted in the simulations and happens with a probability of $p_{dark}^{or} = 2.63\%$. This latter probability is higher than what is predicted by the simulation and could not be explained up to now.

Without the selection of the measurement basis with a random number generator the overall

duration that is necessary to finalize the readout was found to be 820 nanoseconds. Including the random number generator it is expected to be still below 920 ns which makes the system suitable for closing the locality loophole in a Bell experiment with an inter-atomic distance of 400 meters.

In the end of the chapter the possibility to perform the state readout in arbitrary measurement bases has been tested. This revealed correlations between the atomic and photonic state that are characteristic for an entangled state. Compared to the slower fluorescence detection the new fast CEM-based scheme shows only slightly lower visibilities of the correlation curves. They are in the range of 90.6%...93.6% and should also enable a clear violation of Bell's inequality with a pair of entangled atoms.

# 6. Conclusion

This thesis presented the implementation of a method to perform fast and precise quantum mechanical projection measurements on an atomic qubit that is encoded in the $m_F = \pm 1$ Zeeman sublevels of the $S_{1/2}, F = 1$ ground state of a single trapped Rubidium 87 atom. The method is based on a laser induced Zeeman state selective ionization of the atom and the subsequent detection of the ionization fragments (the electron and the ion) with two channel electron multipliers. For each polarization of the readout laser there is a superposition of Zeeman states that does not interact with the ionizing light field and hence is not ionized (dark state), while the orthogonal state is bright and does get ionized. After the detection of at least one of the two fragments the atomic state is considered to having been projected onto the bright state of the laser ionization. If no fragment is detected, one considers this as a projection onto the dark state of the readout. Since this method always delivers either one of the two outcomes for every readout attempt, it inherently closes the detection loophole in a Bell-experiment with single atoms.

The laser ionization is a two photon process where the atom is first state-selectively excited to the intermediate state $P_{1/2}, F' = 1, m_F = 0$ by the so-called readout laser and then gets ionized by a second laser. It is the polarization of the exciting readout laser that defines the measurement basis of the atomic state readout. Numerical simulations of the laser ionization showed that the maximum contrast with which the dark and bright states can be distinguished is 97%. Even in an ideal experimental setup this contrast is limited by two effects: First, atoms in the bright state that have been excited by the readout laser can decay to the dark state before being ionized. And second, atoms in the dark state can get ionized via off-resonant coupling of the readout laser to the neighboring $F' = 2$ hyperfine level. In order to test this state selective ionization experimentally, the atom can be prepared in arbitrary superpositions of the Zeeman states by first entangling the spin state of the atom with the polarization of a single photon and then projecting the photon onto the corresponding basis of polarization states.

This work comprises the construction and characterization of an atom trap setup that allows to generate the atom-photon entanglement, prepare a desired atomic state and perform the envisaged atomic state readout. To detect the ionization fragments a system of two charged particle detectors has been integrated into the trap setup. To be able to reach high detection efficiencies, the transverse electric field configuration between the detectors can be tuned with two pairs of electrodes - copper plates and the indium tin oxide coated walls of the ultra-high vacuum glass cell. These electrodes allow to optimize the overlap of the position of the single atom trap with the spatial volume from which the fragments are detected efficiently. The maximum observed probability to detect at least one of the two fragments from the ionization of a trapped atom is 99.4%. This allows for a high fidelity of the state readout.

After optimization of the laser pulse parameters an experimental characterization of the Zeeman state selective readout yielded a maximum contrast of 93.8% for the distinction between the

bright and dark state. In measurements of atom-photon correlations the ability of the readout to perform measurements in arbitrary bases could be demonstrated. The visibilities of the correlation curves are in the range of 90.6%...93.6% and are mainly limited by errors in the atomic state readout. All in all the quality of the atomic state readout should allow to violate Bell's inequality significantly.

Also the duration of the state readout has been optimized. Fast switching of the polarization of the readout laser, as it is required for closing the locality loophole in a Bell-experiment, is achieved with two fast accousto-optic modulators that control the power of two laser beams with the appropriate predefined polarizations. The time delay between addressing one of the AOMs and the arrival of the optical pulse at the atom is 185 ns. The optimum contrast of the Zeeman state selective ionization is reached for a duration of the ionizing laser pulses of 140 ns. The time needed for the detection of the ionization fragments is limited by the time of flight of the heavier ions that are detected about 360 ns after the electrons. The overall duration of the atomic state readout including further electronic delays and the temporal filtering of the events from the charged particle detectors was found to be 820 ns. Even with the selection of the measurement basis with a quantum random number generator the duration should not exceed 920 ns. A closing of the locality loophole with two atoms at a distance of 400 m hence is also possible.

In a Bell experiment with widely separated atoms the delay between the creation of entanglement and the beginning of the state readout will lead to decoherence of the atomic state. This is mainly due to circular components of the trapping laser's polarization that show strong temperature dependence. Also the fidelities of the atomic state preparation and readout require precise control of the polarization of the single photons and all lasers and hence minimum drifts of the birefringence of all optical components. To achieve the necessary stability, a stabilization of the air temperature in the trap was designed that reduces temperature variations to below 0.01 K peak-to-peak for the most critical components and still well below 0.1 K at more remote positions. This stability is maintained over periods of days and weeks.

### Successful loophole-free Bell experiment

Recently our group was able to successfully perform the envisaged loophole-free Bell experiment with two single Rubidium 87 atoms that were trapped at a distance of 400 meters. For this both trap setups were equipped with the atomic state readout and the temperature stabilization presented in this work. Using entanglement swapping the atoms were prepared in an entangled Bell state (see figure 1.1 and [26] for the entanglement scheme). The atomic state readout was then initialized simultaneously at both locations. The measurement basis on each side was switched with the fast AOMs upon retrieval of a random number and the results were registered by local electronic units ("the observers"). Evaluation of the correlations in the measurement outcomes on both sides yielded a clear violation of the CHSH inequality by more than six standard deviations thus excluding the possibility of local hidden variables with a very high significance.

# A. Constants

| Physical constants | | |
|---|---|---|
| $\hbar$ | reduced Planck constant | $1.054571726 \cdot 10^{-34}\,\mathrm{J \cdot s}$ |
| $c$ | speed of light in vacuum | $2.99792458 \cdot 10^{8}\,{}^{m}/_{\mathrm{s}}$ |
| $\mu_0$ | permeability of free space | $1.25663770614 \cdot 10^{-6}\,{}^{N}/_{\mathrm{A}^2}$ |
| $\epsilon_0 = \frac{1}{c^2\mu_0}$ | permittivity of free space | $8.8541878176 \cdot 10^{-12}\,{}^{F}/_{\mathrm{m}}$ |
| $e$ | elementary charge | $1.602176565 \cdot 10^{-19}\,\mathrm{C}$ |

| Properties of Rubidium 87 | | |
|---|---|---|
| $\tau_{D1}$ | lifetime of the $5P_{1/2}$ excited state | $27.679\,\mathrm{ns}$ |
| $\tau_{D2}$ | lifetime of the $5P_{3/2}$ excited state | $26.2348\,\mathrm{ns}$ |
| $\Gamma_{D1}$ | decay rate of the $D1$ transition | $2\pi \cdot 5.7500\,\mathrm{MHz}$ |
| $\Gamma_{D2}$ | decay rate of the $D2$ transition | $2\pi \cdot 6.0666\,\mathrm{MHz}$ |
| $d_{D1}$ | dipole matrix element of the $D1$ transition | $2.53766 \cdot 10^{-29}\,\mathrm{C \cdot m}$ |
| $d_{D2}$ | dipole matrix element of the $D2$ transition | $3.58424 \cdot 10^{-29}\,\mathrm{C \cdot m}$ |

Table A.1.: Physical constants and properties of ${}^{87}Rb$.

# B. Fluorescence detection of trapped atoms

The presence of an atom in the optical dipole trap can be sensed by irradiating the trap region with light and collecting the fluorescence photons that are scattered by the atom. Analogous to the detection of the ionization fragments this also allows to determine the outcome of a laser-induced ionization of a trapped atom. The relationship of the results obtained from the fluorescence detection and the detection of the ionization fragments is of a complementary nature: If the atom is not ionized, no fragments will be detected. But since the atom then remains trapped, one should see fluorescence. On the other hand, if the atom is ionized, one should detect fragments, but see no fluorescence. The fluorescence detection can hence serve as a comparative measurement to test the results from the charged particle detectors. During all experiments with single trapped atoms, where ionization fragments are created, both methods are always used in parallel.

After a short description of the method the strengths and weaknesses of both detection schemes will be compared.

### Method

The presence of the atom in the trap after the laser-induced state selective ionization can be verified by the emitted fluorescence. For this the cooling and repump lasers from the MOT are switched on and the resulting fluorescence photons from the atom are collected with the confocal microscope over a fixed period of time. If the total number of detected photons exceeds a predefined threshold the atom is considered to be still present in the trap. Otherwise the atom is considered as having been ionized.

Figure B.1 shows a histogram of the accumulated fluorescence counts collected during a time window of 66 milliseconds. The total number of events in this experiment was 99169. In about half of the cases the atoms had been ionized and thus left the trap whereas in the other half of the cases they remained in the trap. As one can see from the graph, these two types of events can clearly be identified by the number of detected fluorescence photons. The indicated threshold for distinguishing the cases is not set symmetrically in the middle between the two peaks but rather closer to the peak for “no atom in trap”. This is motivated by the fact that it can happen that a trapped atom can be lost during the rather long duration of the fluorescence detection (60 ms), thus leading to a significantly lower photon number. It turns out that this is the primary reason of events with such intermediate photon rates and it is much more probable than detecting an unusually increased fluorescence with no atom in the trap (e.g. due a varying background count rate).

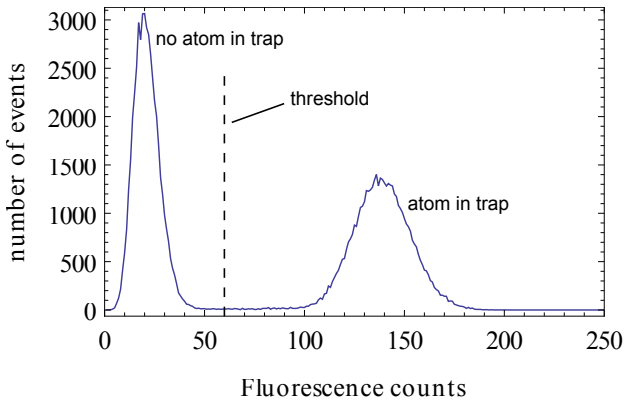


Figure B.1.: Histogram of the accumulated photon counts during the fluorescence detection. The cases "atom in trap" and "no atom in trap" can clearly be distinguished.

### Comparison to the detection of ionization fragments

In the following we compare the fidelity of this detection method to that of detecting the ionization fragments. The identification of cases where the atom has been ionized and left the trap happens with almost perfect precision as the probability to detect a high level of fluorescence with no atom in the trap is practically zero. In this case the fluorescence readout outperforms the detection of the fragments due to the limited quantum efficiency of the employed particle detectors. On the other hand, as stated above, cases where the atom remained in the trap because it was not ionized are not perfectly identified by the fluorescence detection as the atom might be lost due to other effects after the state-selective ionization. Here the detection of the fragments shows superior performance due to the low dark count rate of the charged particle detectors.

Table B.1 summarizes the respective fidelities of the two detection schemes[1]. Although the individual fidelities for the cases "atom ionized/not ionized" slightly differ for the two methods, one can see that the overall contrast for distinguishing the two cases is almost the same. This means that the atomic state readout should have approximately the same quality for both methods.

| | atom ionized | atom not ionized |
|---|---|---|
| fluorescence detection | 100% | (99.0±0.5)% |
| detection of ionization fragments ($\eta_{comb}$) | (99.41±0.02)% | >99.99% |

Table B.1.: Comparison of the fidelities of the fluorescence based detection and the detection of the ionization fragments.

[1] Values for the detection of the ionization fragments in case "atom not ionized" are based on the dark count rates of the CEM setup of trap 1 given in table 4.1 for an acceptance time window of the fragments of 200 ns. For "atom ionized" the value is given by the combined detection efficiency $\eta_{comb}$ determined in section 4.4. The value for the fluorescence detection in the case "atom not ionized" could then be extracted from measurements on single atoms where both methods were used in parallel.

# C. Rabi frequencies and saturation intensities of dipole transitions

When using the oscillating electric field from a monochromatic laser to drive transitions between different atomic states, the interaction between the light field and the atom is governed by the transition dipole matrix elements $d_{Dx}$ of the $D1$ and $D2$-lines and the Clebsch-Gordon coefficients $\mathrm{CGC}$ of the considered transitions (values can be found in [30]). In a two-level system without spontaneous decay the atom-light interaction leads to coherent oscillations of the occupation probabilities between the two coupled atomic states with the Rabi frequency $\Omega$. For a given intensity $I$ of the light field this frequency is given by:

$$\Omega = \frac{d_{Dx} \cdot \mathrm{CGC}(\mathrm{F}, \mathrm{m_F}; \mathrm{F'}, \mathrm{m'_F}) \cdot \mathrm{E}_0}{\hbar} = \frac{d_{Dx} \cdot \mathrm{CGC}(\mathrm{F}, \mathrm{m_F}; \mathrm{F'}, \mathrm{m'_F}) \cdot}{\hbar} \sqrt{\frac{2 \cdot I}{c \cdot \epsilon_0}} \tag{C.1}$$

where $E_0$ is the field amplitude of the light field

When the spontaneous decay of the excited state with the decay rate $\Gamma_{Dx}$ is included, a characteristic intensity is given by the saturation intensity $I_{sat}$

$$I_{sat} = \frac{c\epsilon_0 \Gamma_{Dx}^2 \hbar^2}{4 \cdot |d_{Dx} \cdot \mathrm{CGC}(\mathrm{F}, \mathrm{m_F}; \mathrm{F'}, \mathrm{m'_F})|^2} \tag{C.2}$$

For $I \gg I_{sat}$ the populations of the ground and excited state equal 1/2.

The following table lists the saturation intensities of the cycling and readout beam, that are involved in the atomic state readout.

| | $I_{sat}$ |
|---|---|
| Cycling | $1.669\ \frac{\mathrm{mW}}{\mathrm{cm}^2}$ |
| Readout | $5.98\ \frac{\mathrm{mW}}{\mathrm{cm}^2}$ |

Table C.1.: Saturation intensities of the cycling and readout transitions.

Due to the strong spatial localization of the atom (see section 2.2.2) one can assume that it is always exposed to the peak intensity $I(0,0)$ in the center of the focal spots of the gaussian laser beams. To calculate the optical power $P$ that is needed to obtain $I(0,0) = I_{sat}$ for a focal waist $w_0$ one must use the following relation

$$I(0,0) = \frac{2P}{\pi\, w_0^2}. \tag{C.3}$$

# D. Birefringence of the glass cells

## D.1. Influence of mechanical forces on the birefringence in previous setups

In previous vacuum setups the ultra-high vacuum glass cell was pressed against the vacuum flange with the help of a stamp on the front face of the cell (see figure D.1). We calculate here the stress induced birefringence in the large sidewalls of the cell under the influence of the force $F$ that is applied with this stamp.

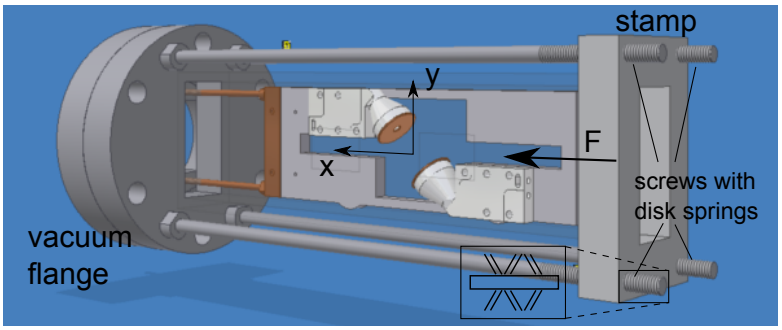


Figure D.1.: Design of the previously used UHV glass cell with the installed particle detectors. A stamp presses the cell onto an indium gasket on a vaccum flange thus inducing birefringence in the glass walls.

The force has been derived from the measured compression of three pairs of disk springs[1] that were placed between the stamp and the nuts that exerted the compressing force (see insert in the figure). The force per screw was determined to be of about $(170 \pm 50)$ Newton with the large error being due to the difficulty to precisely measure the compression of the springs. This means that the force per side wall is $F = 340\,\mathrm{N}$.

We now calculate the impact of the birefringence on a $+45°$-polarized laser beam crossing the glass wall under 90° angle of incidence. The relevant quantity for this is the resulting phase retardance $\Delta\phi$ between electric field components along the $x$- and $y$-axis. It is given by

$$\Delta\phi = \frac{1}{\lambda} C \cdot t \cdot (\sigma_x - \sigma_y) \tag{D.1}$$

[1] Schnorr 027100, 84 Newton at 75% compression. Two springs were placed on top of each other in order to double the spring constant.

where $\lambda$ is the wavelength of the laser light (780 nm), $C$ is the stress optical coefficient ($3.4{\cdot}10^{-12}\frac{1}{\mathrm{Pa}}$ for Schott Lithosil quartz glass), $t$=3.5 mm is the thickness of the wall and $\sigma_x$, $\sigma_y$ are the diagonal elements of the stress tensor along the $x$- and $y$-axis that lie in the plane of the glass wall. If the cell is evacuated, the stress tensor generally also depends on the pressure difference between inside and outside the cell. However, since the phase retardance depends only on the difference of $\sigma_x$ and $\sigma_y$ and since the beams cross the cell in its center, due to symmetry reasons the net effect will be small and is neglected here (the difference was also experimentally quantified, see following section). We therefore set $\sigma_y = 0$ and determine only the dependence of $\sigma_x$ on the force $F$. With $t$=3.5 mm and the height of the cell being 42 mm one obtains:

$$\sigma_x = \frac{F}{3.5 \cdot 42\,\mathrm{mm}^2} = 2.31\frac{\mathrm{N}}{\mathrm{mm}^2} \tag{D.2}$$

and hence

$$\begin{aligned} \Delta\phi &= \frac{1}{780\,\mathrm{nm}} 3.4 \cdot 10^{-12}\frac{1}{\mathrm{Pa}} \cdot 3.5\,\mathrm{mm} \cdot 2.31\,\frac{\mathrm{N}}{\mathrm{mm}^2} \\ \Delta\phi &= \frac{27.6\,\mathrm{nm}}{780\,\mathrm{nm}} = 0.0708\,\pi. \end{aligned}$$

Consider now an incoming $+45°$ polarized laser beam:

$$|\Psi\rangle = \frac{1}{\sqrt{2}}\left(|H\rangle + |V\rangle\right)$$

After transmission through the glass wall this polarization state is transformed into:

$$|\Psi'\rangle = \frac{1}{\sqrt{2}}\left(|H\rangle + e^{i\,\Delta\phi}|V\rangle\right)$$

The extinction ratio that can be expected for this beam at a $-45°$-oriented polarizer behind the glass wall will then be:

$$\begin{aligned} |\langle -45°|\Psi'\rangle|^2 &= \left|\frac{1}{2}\left(\langle H| - \langle V|\right)\left(|H\rangle + e^{i\,\Delta\phi}|V\rangle\right)\right|^2 \\ &= \frac{1}{4}\left|\left(1 - \cos\left(\Delta\phi\right) - i\sin\left(\Delta\phi\right)\right)\right|^2 \end{aligned}$$

For small retardances $\Delta\phi$ this can be simplified to:

$$|\langle -45°|\Psi'\rangle|^2 \approx \frac{1}{4}(\Delta\phi)^2$$

Together with equations D.1 and D.2 it follows that the extinction depends quadratically on the applied force $F$.

For the above parameters we obtain an extinction of 1.2%. The extinction for $+45°$-polarized light has also been measured experimentally for the unevacuated cell setup. It was determined separately for the two walls of this glass cell by placing one polarizer within the cell and another

in front and behind the cell. The extinction ratios were 2.2% and 0.63%, respectively. Considering the large error in determining $F$ this is in agreement with the result from the calculation.

Note, that in this situation light that is polarized parallel to the $x$- or $y$-axis, i.e. parallel or orthogonal to the direction of the force $F$, should not be influenced. This has also been confirmed experimentally.

## D.2. Influence of the evacuation on the cell's birefringence

Moreover, the birefringence of the individual glass walls of this previous setup was also measured for an evacuated and not evacuated cell without the external force that is applied with the stamp. This was done in order to obtain an estimate about the birefringence that can be expected from the new cell that is introduced in this thesis and which avoids the pressure from the problematic stamp. The measurements were again performed for an input polarization of $+45°$. The determination of the birefringence for the evacuated cell without the stamp was possible since the indium gasket remains tight if one loosens the screws on the stamp after the vacuum has been established. Except for the wall thickness (3 mm for the old type, 3.5 mm for the new) and the glass flange of the new cell both cell types have the same dimensions.

Table D.1 shows the results of these measurements. At first one can see that the birefringence is in general strikingly lower without the pressure from the stamp. The extinctions differ by up to two orders of magnitude. Additionally, compared to the effect from the stamp, the evacuation of the cell has only a very small impact on the birefringence.

| | sidewall 1 | | sidewall 2 | |
|---|---|---|---|---|
| | with stamp | without stamp | with stamp | without stamp |
| evacuated | - | 0.09‰ | - | 0.13‰ |
| unevacuated | 0.63% | 0.05‰ | 2.2% | 0.1‰ |

Table D.1.: Extinction of $+45°$-polarized light transmitted through the center of the sidewalls of the glass cell at a crossed polarizer (wavelength 780 nm). The measurement was performed for an evacuated and unevacuated cell and with the screws of the stamp tightened and not tightened. (Values in the empty cells were not measured.)

# E. Photos of the polished CEM copper frame

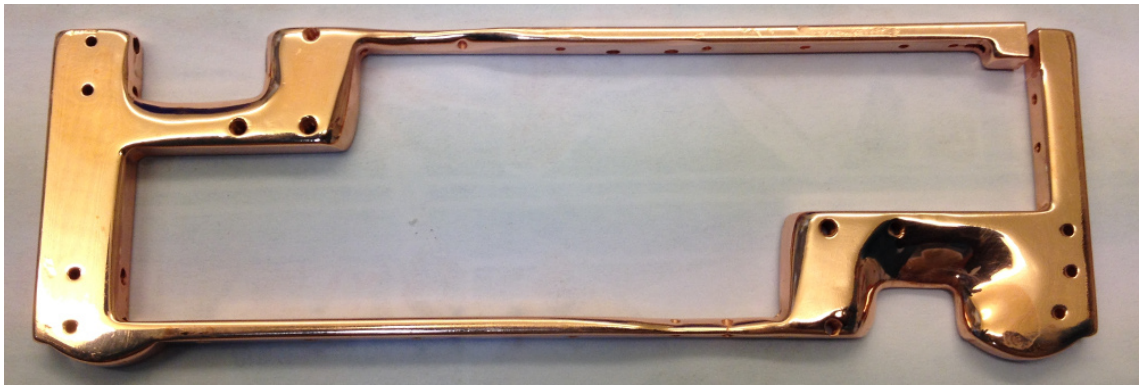

Figure E.1.: The frame for holding the channel electron multipliers after polishing.

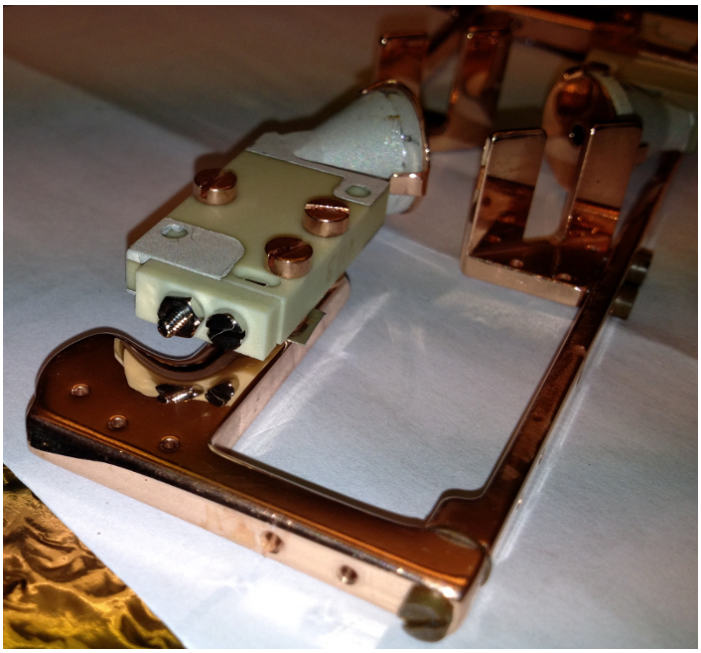

Figure E.2.: Close up view showing the rear side of a CEM mounted on the frame.

# F. Background events due to the ionization laser

Figure F.1 shows detection events at the electron CEM of trap 2 that were generated by the 450 nm ionization laser. Like in experiments on the ionization of single trapped atoms the ionization laser was applied in short pulses - here with a duration of 500 ns - at an optical power of ≈400 mW. The measurement was performed without atoms in the optical dipole trap and all other laser were switched off. All events are hence due to the ionization laser alone.

After 28960 repetitions a total of 5336 events were detected at the electron CEM. Just like the signals from the detection of electrons from the ionization of real atoms the events are detected simultaneously with the arrival of the optical pulse at the trap. This results from the short time of flight of the electrons due to their low mass. The events are almost evenly distributed over the full pulse duration. No events are detected at the ion CEM - neither in the depicted time window nor at later times. The probability to detect such an event in a 200 ns long time window is $\frac{5336}{28960} \cdot \frac{200\,\mathrm{ns}}{500\,\mathrm{ns}} = 7.4\%$

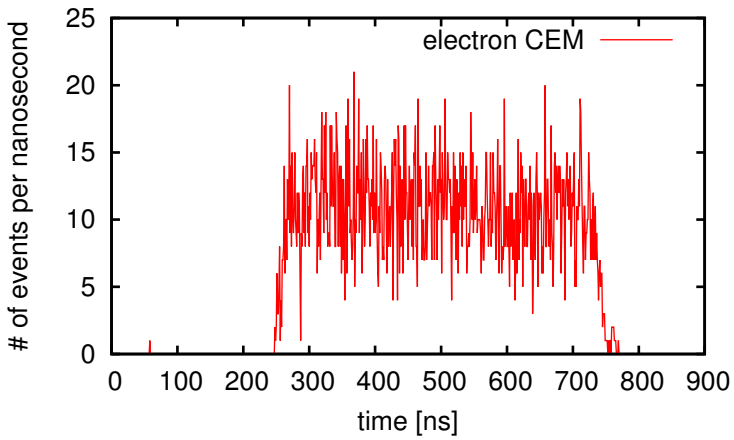


Figure F.1.: Time histogram of the detection events at the electron CEM of trap 2 when applying a 500 ns long laser pulse with the 450 nm ionization laser. The shape of the histogram reproduces well the rectangular temporal shape of the laser pulse.

The events are assumed to originate from the ionization of Rubidium atoms that have been adsorbed on the front surface of the CEMs. This assumption is supported by the fact that the event rate increases with the time the Rubidium dispensers were switched on and decreases when the vacuum chamber is cleaned from the Rubidium layer with UV light.

Moreover, the effect disappears when the laser is blocked after exiting the vacuum chamber in front of the focusing lens of the readout laser. This suggests that reflections from the lens that hit the CEMs cause the dark counts (the lens is only anti-reflection coated for the near-infrared). Electrons originating from the glass walls can be excluded given the applied voltage configuration with all walls being positively charged with respect to the electron CEM. Also, such electrons would already be created by the actual laser beam when entering and exiting the glass cell.

The problem could be solved by replacing the laser with another at a wavelength of 473 nm that has a lower photon energy and by regularly cleaning the vacuum chamber from Rubidium with UV-light.

# Bibliography


[1] A. Einstein, B. Podolsky, and N. Rosen. Can Quantum-Mechanical Description of Physical Reality Be Considered Complete? *Phys. Rev.*, 47:777–780, May 1935.

[2] David Bohm. *Quantum Theory*. Prentice-Hall, New York, 1951.

[3] D. Bohm and Y. Aharonov. Discussion of Experimental Proof for the Paradox of Einstein, Rosen, and Podolsky. *Phys. Rev.*, 108:1070–1076, Nov 1957.

[4] J.S. Bell. On the Einstein-Podolsky-Rosen paradox. *Physics*, 1(3):195–200, 1964.

[5] John F. Clauser, Michael A. Horne, Abner Shimony, and Richard A. Holt. Proposed Experiment to Test Local Hidden-Variable Theories. *Phys. Rev. Lett.*, 23:880–884, Oct 1969.

[6] Stuart J. Freedman and John F. Clauser. Experimental Test of Local Hidden-Variable Theories. *Phys. Rev. Lett.*, 28:938–941, Apr 1972.

[7] Alain Aspect, Philippe Grangier, and Gérard Roger. Experimental Tests of Realistic Local Theories via Bell's Theorem. *Phys. Rev. Lett.*, 47:460–463, Aug 1981.

[8] Alain Aspect, Philippe Grangier, and Gérard Roger. Experimental Realization of Einstein-Podolsky-Rosen-Bohm *Gedankenexperiment* : A New Violation of Bell's Inequalities. *Phys. Rev. Lett.*, 49:91–94, Jul 1982.

[9] Philip M. Pearle. Hidden-Variable Example Based upon Data Rejection. *Phys. Rev. D*, 2:1418–1425, Oct 1970.

[10] Alain Aspect, Jean Dalibard, and Gérard Roger. Experimental Test of Bell's Inequalities Using Time- Varying Analyzers. *Phys. Rev. Lett.*, 49:1804–1807, Dec 1982.

[11] Gregor Weihs, Thomas Jennewein, Christoph Simon, Harald Weinfurter, and Anton Zeilinger. Violation of Bell's Inequality under Strict Einstein Locality Conditions. *Phys. Rev. Lett.*, 81:5039–5043, Dec 1998.

[12] Thomas Scheidl, Rupert Ursin, Johannes Kofler, Sven Ramelow, Xiao-Song Ma, Thomas Herbst, Lothar Ratschbacher, Alessandro Fedrizzi, Nathan K. Langford, Thomas Jennewein, and Anton Zeilinger. Violation of local realism with freedom of choice. *PNAS*, 107(46):19708–19713, November 2010.

[13] M. A. Rowe, D. Kielpinski, V. Meyer, C. A. Sackett, W. M. Itano, C. Monroe, and D. J. Wineland. Experimental violation of a Bell's inequality with efficient detection. *Nature*, 409(6822):791–794, February 2001.

[14] Markus Ansmann, H. Wang, Radoslaw C. Bialczak, Max Hofheinz, Erik Lucero, M. Neeley, A. D. O'Connell, D. Sank, M. Weides, J. Wenner, A. N. Cleland, and John M. Martinis. Violation of Bell's inequality in Josephson phase qubits. *Nature*, 461(7263):504–506, September 2009.

[15] Adriana E. Lita, Aaron J. Miller, and Sae Woo Nam. Counting near-infrared single-photons with 95% efficiency. *Opt. Express*, 16(5):3032–3040, Mar 2008.

[16] Marissa Giustina, Alexandra Mech, Sven Ramelow, Bernhard Wittmann, Johannes Kofler, Jorn Beyer, Adriana Lita, Brice Calkins, Thomas Gerrits, Sae Woo Nam, Rupert Ursin, and Anton Zeilinger. Bell violation using entangled photons without the fair-sampling assumption. *Nature*, 497(7448):227–230, May 2013.

[17] B. Hensen, H. Bernien, A. E. Dreau, A. Reiserer, N. Kalb, M. S. Blok, J. Ruitenberg, R. F. L. Vermeulen, R. N. Schouten, C. Abellan, W. Amaya, V. Pruneri, M. W. Mitchell, M. Markham, D. J. Twitchen, D. Elkouss, S. Wehner, T. H. Taminiau, and R. Hanson. Loophole-free Bell inequality violation using electron spins separated by 1.3 kilometres. *Nature*, 526(7575):682–686, October 2015.

[18] B. Hensen, N. Kalb, M.S. Blok, A. Dréau, A. Reiserer, R.F.L. Vermeulen, R.N. Schouten, M. Markham, D.J. Twitchen, K. Goodenough, D. Elkouss, S. Wehner, T.H. Taminiau, and R. Hanson. Loophole-free Bell test using electron spins in diamond: second experiment and additional analysis. *arXiv:1603.05705v2*, 2016.

[19] Lynden K. Shalm, Evan Meyer-Scott, Bradley G. Christensen, Peter Bierhorst, Michael A. Wayne, Martin J. Stevens, Thomas Gerrits, Scott Glancy, Deny R. Hamel, Michael S. Allman, Kevin J. Coakley, Shellee D. Dyer, Carson Hodge, Adriana E. Lita, Varun B. Verma, Camilla Lambrocco, Edward Tortorici, Alan L. Migdall, Yanbao Zhang, Daniel R. Kumor, William H. Farr, Francesco Marsili, Matthew D. Shaw, Jeffrey A. Stern, Carlos Abellán, Waldimar Amaya, Valerio Pruneri, Thomas Jennewein, Morgan W. Mitchell, Paul G. Kwiat, Joshua C. Bienfang, Richard P. Mirin, Emanuel Knill, and Sae Woo Nam. Strong Loophole-Free Test of Local Realism. *Phys. Rev. Lett.*, 115:250402, Dec 2015.

[20] David Bohm. A Suggested Interpretation of the Quantum Theory in Terms of "Hidden" Variables. I. *Phys. Rev.*, 85:166–179, Jan 1952.

[21] David Bohm. A Suggested Interpretation of the Quantum Theory in Terms of "Hidden" Variables. II. *Phys. Rev.*, 85:180–193, Jan 1952.

[22] Artur K. Ekert. Quantum cryptography based on Bell's theorem. *Phys. Rev. Lett.*, 67:661–663, Aug 1991.

[23] Umesh Vazirani and Thomas Vidick. Fully Device-Independent Quantum Key Distribution. *Phys. Rev. Lett.*, 113:140501, Sep 2014.

[24] M. Żukowski, A. Zeilinger, M. A. Horne, and A. K. Ekert. "Event-ready-detectors" Bell experiment via entanglement swapping. *Phys. Rev. Lett.*, 71:4287–4290, Dec 1993.

[25] C. K. Hong, Z. Y. Ou, and L. Mandel. Measurement of subpicosecond time intervals between two photons by interference. *Phys. Rev. Lett.*, 59:2044–2046, Nov 1987.

[26] Julian Hofmann, Michael Krug, Norbert Ortegel, Lea Gérard, Markus Weber, Wenjamin Rosenfeld, and Harald Weinfurter. Heralded Entanglement Between Widely Separated Atoms. *Science*, 337(6090):72–75, 2012.

[27] W. Rosenfeld, F. Hocke, F. Henkel, M. Krug, J. Volz, M. Weber, and H. Weinfurter. Towards Long-Distance Atom-Photon Entanglement. *Phys. Rev. Lett.*, 101:260403, Dec 2008.

[28] Florian Henkel. Photoionisation detection of single $^{87}$Rb-atoms using channel electron multipliers. PhD thesis, Ludwig-Maximilians-Universität München, November 2011.

[29] Michael Krug. Title to be announced. PhD thesis, Ludwig-Maximilians-Universität München.

[30] Daniel A Steck. Rubidium 87 d line data. *http://steck.us/alkalidata/rubidium87numbers.pdf*, version 2.1.5 from 5 January 2015.

[31] E. L. Raab, M. Prentiss, Alex Cable, Steven Chu, and D. E. Pritchard. Trapping of Neutral Sodium Atoms with Radiation Pressure. *Phys. Rev. Lett.*, 59:2631–2634, Dec 1987.

[32] H.J. Metcalf and P. van der Straten. *Laser cooling and trapping*. Springer Verlag, New York, 1999.

[33] T. W. Hänsch and A. L. Schawlow. Cooling of gases by laser radiation. *Optics Communications*, 13(1):68 – 69, 1975.

[34] J. Dalibard and C. Cohen-Tannoudji. Laser cooling below the Doppler limit by polarization gradients: simple theoretical models. *J. Opt. Soc. Am. B*, 6(11):2023–2045, Nov 1989.

[35] Rudolf Grimm, Matthias Weidemüller, and Yurii B. Ovchinnikov. Optical dipole traps for neutral atoms. *arXiv:physics/9902072*, 1999.

[36] K. L. Corwin, S. J. M. Kuppens, D. Cho, and C. E. Wieman. Spin-Polarized Atoms in a Circularly Polarized Optical Dipole Trap. *Phys. Rev. Lett.*, 83:1311–1314, Aug 1999.

[37] Nicolas Schlosser, Georges Reymond, Igor Protsenko, and Philippe Grangier. Sub-poissonian loading of single atoms in a microscopic dipole trap. *Nature*, 411:1024–1027, 2001.

[38] N. Schlosser, G. Reymond, and P. Grangier. Collisional Blockade in Microscopic Optical Dipole Traps. *Phys. Rev. Lett.*, 89:023005, Jun 2002.

[39] Norbert Ortegel. Atom-photon entanglement. Diplomarbeit, Ludwig-Maximilians-Universität München, 2009.

[40] Wenjamin Rosenfeld. Experiments with an Entangled System of a Single Atom and a Single Photon. PhD thesis, Ludwig-Maximilians-Universität München, November 2008.

[41] C. Klempt, T. van Zoest, T. Henninger, O. Topic, E. Rasel, W. Ertmer, and J. Arlt. Ultraviolet light-induced atom desorption for large rubidium and potassium magneto-optical traps. *Phys. Rev. A*, 73:013410, Jan 2006.

[42] Jürgen Volz. Atom-Photon Entanglement. PhD thesis, Ludwig-Maximilians-Universität München, Juli 2006.

[43] Julian Hofmann. Heralded atom-atom entanglement. PhD thesis, January 2014.

[44] Jürgen Volz, Markus Weber, Daniel Schlenk, Wenjamin Rosenfeld, Johannes Vrana, Karen Saucke, Christian Kurtsiefer, and Harald Weinfurter. Observation of Entanglement of a Single Photon with a Trapped Atom. *Phys. Rev. Lett.*, 96:030404, Jan 2006.

[45] Markus Weber, Jürgen Volz, Karen Saucke, Christian Kurtsiefer, and Harald Weinfurter. Analysis of a single-atom dipole trap. *Phys. Rev. A*, 73:043406, Apr 2006.

[46] Andreas Deeg. Zustandsdetektion eines einzelnen Atoms. Diplomarbeit, Ludwig-Maximilians-Universität München, 2008.

[47] S. Gerber, D. Rotter, M. Hennrich, R. Blatt, F. Rohde, C. Schuck, M. Almendros, R. Gehr, F. Dubin, and J. Eschner. Quantum interference from remotely trapped ions. *New Journal of Physics*, 11(1):013032, 2009.

[48] David Alexander Hucul. A Modular Quantum System of Trapped Atomic Ions. PhD thesis, University of Maryland, 2015.

[49] D. Hucul, I. V. Inlek, G. Vittorini, C. Crocker, S. Debnath, S. M. Clark, and C. Monroe. Modular entanglement of atomic qubits using photons and phonons. *Nat Phys*, 11(1):37–42, January 2015.

[50] Tatjana Wilk, Simon C. Webster, Axel Kuhn, and Gerhard Rempe. Single-Atom Single-Photon Quantum Interface. *Science*, 317(5837):488–490, 2007.

[51] J. D. Sterk, L. Luo, T. A. Manning, P. Maunz, and C. Monroe. Photon collection from a trapped ion-cavity system. *Phys. Rev. A*, 85:062308, Jun 2012.

[52] Matthias Steiner, Hendrik M. Meyer, Christian Deutsch, Jakob Reichel, and Michael Köhl. Single Ion Coupled to an Optical Fiber Cavity. *Phys. Rev. Lett.*, 110:043003, Jan 2013.

[53] Robert Maiwald, Andrea Golla, Martin Fischer, Marianne Bader, Simon Heugel, Benoît Chalopin, Markus Sondermann, and Gerd Leuchs. Collecting more than half the fluorescence photons from a single ion. *Phys. Rev. A*, 86:043431, Oct 2012.

[54] Marlan. O. Scully and M. Suhail Zubairy. *Quantum optics*. Cambridge University Press, 2006.

[55] Robert Garthoff. Optimierte Erzeugung und Nachweis von Atom-Photon-Zuständen zur Verschränkung Räumlich Getrennter Atome. Master's thesis, Ludwig-Maximilians-Universität München, 2015.

[56] L. Ricci, M. Weidemüller, T. Esslinger, A. Hemmerich, C. Zimmermann, V. Vuletic, W. König, and Th. W. Hänsch. A compact grating-stabilized diode laser system for atomic physics. *Optics Communications*, 117(5):541–549, 1995.

[57] Thomas F. Johnston. Beam propagation ($M^2$) measurement made as easy as it gets: the four-cuts method. *Applied optics*, 37(21):4840–4850, 1998.

[58] Christopher C. Davis. *Lasers and Electro-Optics*. Cambridge University Press, 1996.

[59] Jonathan Rohland. Konfiguration und Test eines elektrooptischen Modulators mit Lithiumniobat-Kristall. Bachelor's Thesis, Ludwig-Maximilians-Universität München, June 2012.

[60] Wenjamin Rosenfeld, Jürgen Volz, Markus Weber, and Harald Weinfurter. Coherence of a qubit stored in Zeeman levels of a single optically trapped atom. *Phys. Rev. A*, 84:022343, Aug 2011.

[61] A. Härter, A. Krükow, A. Brunner, and J. Hecker Denschlag. Long-term drifts of stray electric fields in a Paul trap. *Applied Physics B*, 114(1-2):275–281, 2014.

[62] H. Kim, C. M. Gilmore, A. Piqué, J. S. Horwitz, H. Mattoussi, H. Murata, Z. H. Kafafi, and D. B. Chrisey. Electrical, optical, and structural properties of indium-tin-oxide thin films for organic light-emitting devices. *Journal of Applied Physics*, 86(11):6451–6461, 1999.

[63] Y. Park, V. Choong, Y. Gao, B. R. Hsieh, and C. W. Tang. Work function of indium tin oxide transparent conductor measured by photoelectron spectroscopy. *Applied Physics Letters*, 68(19):2699–2701, 1996.

[64] Mirko Vogel. Grenzflächen in Phthalocyanin-C60-Solarzellen. PhD thesis, Freie Universitä t Berlin, 2005.

[65] L. Chkoda, C. Heske, M. Sokolowski, E. Umbach, F. Steuber, J. Staudigel, M. Stößel, and J. Simmerer. Work function of ITO substrates and band-offsets at the TPD/ITO interface determined by photoelectron spectroscopy. *Synthetic Metals*, 111-112:315–319, 2000.

[66] W. Song, S.K. So, and L. Cao. Angular-dependent photoemission studies of indium tin oxide surfaces. *Applied Physics A*, 72(3):361–365, 2001.

[67] H. Y. Yu, X. D. Feng, D. Grozea, Z. H. Lu, R. N. S. Sodhi, A-M. Hor, and H. Aziz. Surface electronic structure of plasma-treated indium tin oxides. *Applied Physics Letters*, 78(17):2595–2597, 2001.

[68] Pascal Alexander Böhi. Coherent manipulation of ultracold atoms with microwave near-fields. PhD thesis, Ludwig-Maximilians-Universität München, August 2010.

[69] For a design guideline of the indium seal see:
http://www.indiumwire.com/cryogenic-vacuum-seals/c205y
Last access: August, 24th 2016.

[70] H.A. Adam, S. Kaufman, and B.S. Liley. Indium seals for dismountable vacuum systems. *Journal of Scientific Instruments*, 34(3):123, 1957.

[71] Stefan Brakhane, Wolfgang Alt, Dieter Meschede, Carsten Robens, Geol Moon, and Andrea Alberti. Note: Ultra-low birefringence dodecagonal vacuum glass cell. *Review of Scientific Instruments*, 86(12), 2015.

[72] Andreas Steffen, Wolfgang Alt, Maximilian Genske, Dieter Meschede, Carsten Robens, and Andrea Alberti. Note: In situ measurement of vacuum window birefringence by atomic spectroscopy. *Review of Scientific Instruments*, 84(12), 2013.

[73] F. Henkel, M. Krug, J. Hofmann, W. Rosenfeld, M. Weber, and H. Weinfurter. Highly Efficient State-Selective Submicrosecond Photoionization Detection of Single Atoms. *Phys. Rev. Lett.*, 105:253001, Dec 2010.

[74] Kai Redeker. Detektion von Ionisationsfragmenten von Rb-87 Atomen. Diplomarbeit, Ludwig-Maximilians-Universität München, 2012.

[75] W. Haynes, editor. *CRC Handbook of Chemistry and Physics*. 2011.

[76] T. Campey, C. J. Vale, M. J. Davis, N. R. Heckenberg, H. Rubinsztein-Dunlop, S. Kraft, C. Zimmermann, and J. Fortágh. Atom counting in ultracold gases using photoionization and ion detection. *Phys. Rev. A*, 74:043612, Oct 2006.

[77] Christian Kurtsiefer. A programmable pattern generator - *Unpublished*. 2002.

[78] Martin Fürst. Quantenoptisches Verfahren zur Erzeugung zufälliger Bitfolgen. PhD thesis, August 2011.

# Danksagungen

Zum Schluß ergeht noch ein herzlicher Dank an alle, die zum Gelingen und dieser Arbeit beigetragen haben:

- Prof. Harald Weinfurter für die Möglichkeit diese Arbeit in seiner Gruppe durchführen zu können.
- Wenjamin Rosenfeld für die Betreuung am Experiment und die vielen fruchtvollen Diskussionen.
- Markus Weber für den Einstieg ins Thema Channeltrons und die herzliche Art.
- An meine Master- und Diplomstudenten Chien-Ju Lee, Kai Redeker, und Robert Garthoff, die mir beim Aufbau der Fallen und Detektoren sowie deren Inbetriebnahme geholfen haben.
- An die Doktoranden vom Experiment: Florian Henkel, Michael Krug, Julian Hofmann, Daniel Burchardt, Kai Redeker und Robert Garthoff für die schönen Stunden im Labor, die lehrreichen Diskussionen und die gemeinsamen Tage auf Konferenzen.
- An all die anderen Doktoranden der Arbeitsgruppe wie Daniel Schlenk, meinen ehemaligen Bürokollegen Sebastian Nauerth, Markus Rau, Christian Schwemmer, Daniel Richardt Lukas Knips, Lars Liebermeister, Martin Zeitlmaier und Gwenaelle Vest. Die Mischung macht's und so jeder hat seinen Teil zu einer angenehmen Atmosphäre in der Gruppe beigetragen.
- An meine Eltern und meinen Bruder Christian für die Unterstützung und dafür, dass Sie sich so gut um unsere kleine Tochter gekümmert haben, wenn es zeitlich einmal eng war.
- Und zuguterletzt an meine kleine Familie, Dorothée und Mathilde, die immer hinter mir standen und mich bis zum Schluß motiviert haben die Sache zu Ende zu bringen.